

**FLOW AND DISPERSION IN URBAN AREAS:
EXPERIMENTAL INVESTIGATION, EVENT
RECONSTRUCTION, AND FORM
OPTIMIZATION**

by

Bhagirath Addepalli

A dissertation submitted to the faculty of
The University of Utah
in partial fulfillment of the requirements for the degree of

Doctor of Philosophy

Department of Mechanical Engineering

The University of Utah

May 2016

Copyright © Bhagirath Addepalli 2016

All Rights Reserved

The University of Utah Graduate School

STATEMENT OF DISSERTATION APPROVAL

The dissertation of Bhagirath Addepalli
has been approved by the following supervisory committee members:

<u>Eric R. Pardyjak</u>	, Chair	<u>12/21/2012</u> Date Approved
<u>Patrick McMurtry</u>	, Member	<u>12/21/2012</u> Date Approved
<u>James R. Stoll</u>	, Member	<u>12/21/2012</u> Date Approved
<u>Peter Willemsen</u>	, Member	<u> </u> Date Approved
<u>David E. Johnson</u>	, Member	<u>12/21/2012</u> Date Approved

and by Tim Ameel, Chair/Dean of
the Department/College/School of Mechanical Engineering

and by David B. Kieda, Dean of The Graduate School.

ABSTRACT

The present work focuses on developing a holistic understanding of flow and dispersion in urban environments. Toward this end, ideas are drawn from the fields of physical modeling, inverse modeling, and optimization in urban fluid dynamics. The physical modeling part of the dissertation investigates flow in the vicinity of tall buildings using wind tunnel two-dimensional particle image velocimetry (PIV) measurements. The data obtained have been used to evaluate and improve urban wind and dispersion models. In the inverse modeling part of the dissertation, an event reconstruction tool is developed to quickly and accurately characterize the source parameters of chemical / biological / radiological (CBR) agents released into the atmosphere in an urban domain. Event reconstruction is performed using concentration measurements obtained from a distributed sensor network in the city, where the spatial coordinates of the sensors are known a priori. Source characterization comprises retrieving several source parameters including the spatial coordinates of the source, the source strength, the wind speed, and wind direction at the source, etc. The Gaussian plume model is adopted as the forward model, and derivative-based optimization is chosen to take advantage of its simple analytical nature. The solution technique developed is independent of the forward model used and is comprised of stochastic search with regularized gradient optimization.

The final part of the dissertation is comprised of urban form optimization. The problem of identification of urban forms that result in the best environmental conditions is referred to as the urban form optimization problem (UFOP). The decision variables optimized include the spatial locations and the physical dimensions of the buildings and the wind speed and wind direction over the domain of interest. For the UFOP, the quick urban and industrial complex (QUIC) dispersion model is used as the forward model. The UFOP is cast as a single optimization problem, and simulated annealing and genetic algorithms are used in the solution procedure.

CONTENTS

ABSTRACT	iii
LIST OF TABLES	vi
CHAPTERS	
1. INTRODUCTION	1
2. INVESTIGATION OF THE FLOW STRUCTURE IN STEP-UP STREET CANYONS—MEAN FLOW AND TURBULENCE STATISTICS	3
2.1 Abstract	4
2.2 Introduction	5
2.3 Experimental Details	7
2.4 Validation Experiments	10
2.5 Results and Discussion	10
2.6 Conclusions	24
2.7 References	24
3. A STUDY OF FLOW FIELDS IN STEP-DOWN STREET CANYON .	27
3.1 Abstract	28
3.2 Introduction	29
3.3 Experimental Details	30
3.4 The Near Wake of An Isolated Tall Building	35
3.5 Results and Discussion	38
3.6 Effect of Street Canyon Aspect Ratio and Building Widths on the In-canyon Flow Structure	53
3.7 Summary	57
3.8 References	68
4. SOURCE CHARACTERIZATION OF ATMOSPHERIC RELEASES USING STOCHASTIC SEARCH AND REGULARIZED GRADIENT OPTIMIZATION	71
4.1 Abstract	72
4.2 Introduction	72
4.3 Problem Definition	77
4.4 The Copenhagen Tracer Experiments	80
4.5 Solution Procedure	82
4.6 Results and Discussion	92
4.7 Conclusions	97
4.8 References	97

5. URBAN FORM OPTIMIZATION FOR IMPROVED AIR QUALITY .	100
5.1 Abstract	100
5.2 Introduction	100
5.3 Problem Definition	102
5.4 The Eight-Dimensional Test Problem	106
5.5 Results and Discussion	108
5.6 Summary	110
5.7 References	111
6. CONCLUSIONS	124

LIST OF TABLES

2.1	The mean spanwise vorticity flux for $H_d/H_u \approx 3; W/S \approx 1$ to 4	16
2.2	The mean spanwise vorticity flux for $H_d/H_u \approx 1.67; W/S \approx 1$ to 4	17
4.1	Salient features of various inversion techniques used to solve atmospheric source characterization problems	75
4.2	Computed inversion model parameters for TCTE	91
4.3	Comparison of the predicted concentrations from Newton's method with Copenhagen data (12:13 h-12:33 h on 19 October 1978) and [16]	94
4.4	Computed inversion model parameters for TCTE using the dataset between 12:13 h and 12:33 h	95
4.5	Performance of the various original QMC point-sets with SR1	95
4.6	Performance of the various scrambled QMC point-sets with SR1	95
4.7	Performance of the various original QMC point-sets with SR3	95
4.8	Performance of the various scrambled QMC point-sets with SR3	96
5.1	Parameters in SA implemented for the 2×2 array problem.	113
5.2	Parameters in the BGA implemented for the 2×2 array problem.	113

CHAPTER 1

INTRODUCTION

A significant fraction of the world's population lives in urban areas. In the coming years, continual migration to urban areas will only see the fraction of urban populace increase. Since cities are regions of intense activity and are the dominant consumers of resources and major producers of waste, urbanization introduces an array of environmental challenges including those related to air quality. As urban density increases, accidental or deliberate release of contaminants in or close to urban centers can result in catastrophic consequences. One such event was recently witnessed with the Fukushima Daiichi nuclear reactor in Japan, with the reactor spewing dangerous radiation into the atmosphere. Countering such situations requires at the very minimum (1) design of sustainable and resilient cities—cities that can resist unknown and variable loadings over a diverse set of environmental conditions, (2) continuous monitoring of hazardous contaminants in an urban area, (3) event reconstruction (inversion) tools to characterize sources of contaminants if detected, (4) high-fidelity forward prediction capability, and (5) a good understanding of flow and dispersion in urban environments. The present work participates in the endeavor to create safe, sustainable, and resilient cities through the development of the following tools, techniques, and investigations (1) an atmospheric event reconstruction tool, (2) an urban form optimization tool, and (3) wind tunnel experiments that shed light on the mechanisms that drive transport of contaminants in the vicinity of tall buildings, which form an important part of urban downtowns.

The objective of the current work is to develop a holistic understanding of flow and dispersion in urban environments. The objective is approached by posing three specific questions:

1. How do tall buildings affect the street level flow patterns in urban areas?
2. Can efficient and robust atmospheric event reconstruction tools be developed that can quickly and accurately characterize the sources of contaminants released into the atmosphere in urban domains?

3. Can a decision-making tool for urban form optimization be developed to serve as a boundary object linking science and policy in coupled human-ecological systems?

In the following chapters, the above-mentioned questions are systematically addressed. The influence of tall buildings on urban street canyon flow is investigated through wind tunnel two-dimensional particle image velocimetry (PIV) measurements around idealized urban configurations. The results of the experiments conducted are discussed in Chapters 2 and 3. Question 2 is addressed by examining the three principal components of a source inversion tool. The three components are (1) the forward prediction model, (2) the objective function formulation, and (3) the optimization method. The effect of judicious choices for these components on the overall efficiency and accuracy of event reconstruction is discussed in Chapter 4. An urban form optimization tool serves to either help design from scratch cities that are environmentally sustainable or modify existing designs so that they eventually become environmentally sustainable. These aspects, along with the fundamental ideas behind single objective optimization techniques, are discussed in Chapter 5.

CHAPTER 2

**INVESTIGATION OF THE FLOW
STRUCTURE IN STEP-UP
STREET CANYONS -
MEAN FLOW AND
TURBULENCE
STATISTICS**

Addepalli B, Pardyjak ER (2013) Investigation of the flow structure in step-up street canyons - Mean flow and turbulence statistics. *Boundary-Layer Meteorol* 148:13–155. Reprinted with kind permission from Springer Science and Business Media.

Investigation of the Flow Structure in Step-Up Street Canyons—Mean Flow and Turbulence Statistics

Bhagirath Addepalli · Eric R. Pardyjak

Received: 27 April 2012 / Accepted: 4 February 2013 / Published online: 12 March 2013
© Springer Science+Business Media Dordrecht 2013

Abstract A step-up street canyon is a characteristic urban element composed of two buildings in which the height of the upwind building (H_u) is less than the height of the downwind building (H_d). Here, the effect of canyon geometry on the flow structure in isolated step-up street canyons is investigated through isothermal wind-tunnel measurements. The measurements were acquired along the vertical symmetry plane of model buildings using two-dimensional particle image velocimetry (PIV) for normal approach flow. The building-height ratios considered were: $H_d/H_u \approx 3$, and $H_d/H_u \approx 1.67$. For each building-height ratio, the along-wind lengths (L) of the upwind and downwind buildings, and the street-canyon width (S) were kept constant, with $L \approx S$. The cross-wind widths (W) of the upwind and downwind buildings were varied uniformly from $W/S \approx 1$ through $W/S \approx 4$, in increments of $W/S \approx 1$. The objective of the work was to characterize the changes in the flow structure in step-up canyons as a function of W/S , for fixed L , S , and H_d/H_u values. The results indicate that the in-canyon flow structure does not vary significantly for $H_d/H_u \approx 3$ for the W/S values considered. Qualitatively, for $H_d/H_u \approx 3$, the upwind building behaves as an obstacle in the upwind cavity of the downwind building. In contrast, the flow patterns observed for the $H_d/H_u \approx 1.67$ configurations are unique and counter-intuitive, and depend strongly on building width (W/S). For $W/S \approx 1$ and $W/S \approx 2$, the effect of lateral flow into the canyon is so prominent that even the mean flow patterns are highly ambiguous. For $W/S \approx 3$ and 4, the flow along the vertical symmetry plane is more shielded from the lateral flow, and hence a stable counter-rotating vortex pair is observed in the canyon. In addition to these qualitative features, a quantitative analysis of the mean flow field and turbulence stress field is presented.

Keywords Particle image velocimetry · Reynolds stresses · Street canyon · Urban fluid mechanics · Wind tunnel

B. Addepalli · E. R. Pardyjak (✉)
Department of Mechanical Engineering, University of Utah, Salt Lake City, UT 84112, USA
e-mail: pardyjak@eng.utah.edu

B. Addepalli
e-mail: addbugs@gmail.com

1 Introduction

Concern over accidental or deliberate releases of contaminants has been a major driving force toward improved understanding of flow and dispersion in urban areas during the last decade. Field experiments such as URBAN 2000 (Allwine et al. 2002) in Salt Lake City, U.S.A., Joint Urban 2003 (Allwine and Flaherty 2006a) in Oklahoma City, U.S.A., DAPPLE (Wood et al. 2009) in London, U.K., as well as the MID05 (Allwine and Flaherty 2007) and MSG05 (Allwine and Flaherty 2006b) both in New York City, U.S.A., were conducted to study the flow and dispersion characteristics in highly built-up downtowns. Numerous empirical models (Panofsky and Dutton 1983; Turner 1994; Beychok 2005), diagnostic tools (Hendricks et al. 2004; Singh et al. 2008), and computational fluid dynamics (CFD) codes (Camelli et al. 2004; Hanna et al. 2004; Coirier and Kim 2006; Chan and Leach 2007) have been developed and are used to predict dispersion patterns in urban areas. Evaluation of these empirical models (Hanna and Baja 2009), diagnostic tools (Hendricks et al. 2004; Singh et al. 2008), and CFD codes (Camelli et al. 2004; Hanna et al. 2004; Coirier and Kim 2006; Hanna et al. 2006; Chan and Leach 2007) using field experimental data illustrated the complex nature of urban street-canyon flows, which makes modelling such processes extremely challenging. The complex nature of urban flows is due to the combined effects of, inter alia, meandering winds, diverse building geometries, complex surface energy balances, vegetative canopies, acting in unison. Wind-tunnel modelling provides a way to systematically control and vary several of these effects in simplified urban configurations. In the present work, the functional relationship between street-canyon geometry and the flow structure within step-up street canyons is investigated through wind-tunnel experiments.

A step-up street canyon is defined as a street canyon in which the upwind building height (H_u) is less than the downwind building height (H_d) (i.e., $H_u < H_d$). The presence of tall buildings in a cluster of relatively shorter buildings (typical of many downtowns) results in the formation of step-up canyons. Step-up canyons cause strong downdrafts in the vicinity of the buildings forming the canyon (Coirier and Kim 2006). The enhanced vertical motions due to step-up canyons affect the flow and dispersion patterns in urban areas in the following ways: (1) strong downdrafts can amplify the in-canyon instantaneous peak concentration levels due to advection of contaminants originating upwind of the canyon, (2) strong downdrafts help in the overall ventilation of pollutants from urban areas due to enhanced mixing (induced by the downdrafts), (3) strong downdrafts, which penetrate to the surface (Nelson et al. 2007), also help in dispersing street-level pollutants due to vehicle induced emissions, and (4) strong downdrafts adversely affect the pedestrian wind comfort in urban areas. To better understand the mechanisms that drive pollutant transport in step-up canyons, in the present work the flow structure in idealized isolated two-building step-up canyons is examined using wind-tunnel two-dimensional (2D) particle image velocimetry (PIV) measurements.

Given the importance attached to understanding step-up street-canyon flows, several researchers have studied flow and dispersion patterns in idealized step-up configurations using numerical simulations and wind-tunnel experiments. Assimakopoulos et al. (2003) simulated the dispersion of emissions from vehicle exhausts in step-up canyons within a built-up 2D urban environment. The simulations were performed using a Reynolds-averaged microscale model. Two step-up geometries were considered. In the first configuration, the ratio of the downwind (H_d) to the upwind (H_u) building height was $H_d/H_u = 2$, with the along-wind length (L) of the buildings being $L = H_d$, and the street-canyon width (S) being $S = H_d$. The second configuration considered was $H_d/H_u = 2$, $L = H_d$, $S = H_d/2$. Through their numerical experiments, Assimakopoulos et al. (2003) found that step-up canyons were characterized by a large distorted primary street-canyon vortex. In their results, the core of the

primary vortex was above the upwind building rooftop, skewed towards the downwind building, and extending beyond the stagnation point on the downwind building. In terms of dispersion, they did not find significant differences in concentration levels in step-up canyons in comparison to square canyons. Yang et al. (2007) investigated the dispersion of chlorine gas released upwind of an isolated step-up canyon using a fire dynamics simulator (FDS), a 2D large-eddy simulation (LES) model. The step-up configuration that they considered was $H_d/H_u = 2$, $L = H_d/2$, $S = H_d/2$. Their results indicate higher concentration levels in step-up canyons in comparison to square canyons. In terms of the wind field, the observed street-canyon vortex was more symmetric (in comparison to that reported by Assimakopoulos et al. (2003)), and did not extend beyond the upwind building rooftop. Xie et al. (2005) studied the dispersion characteristics of vehicle-induced emissions in a 2D computational urban setting comprising four buildings, with different building permutations resulting in step-up and step-down canyons. The step-up canyon that they studied had the geometry $H_d/H_u = 1.5$, $L = H_u$, $S = H_u$. The velocity and concentration fields were computed by numerically solving the Reynolds-averaged equations. Their results follow closely Yang et al. (2007), wherein higher pollutant concentrations were observed in step-up canyons (in comparison to square canyons), and the street-canyon vortex was symmetric. Santiago and Martin (2005) described the flow features in sequences of 2D asymmetric step-up canyons using the CFD software FLUENT. Their computations included step-up geometries where $H_d/H_u = 1.5$, $L = H_d/3$, with $S/H_u = 0.25, 0.5$ and unity respectively. Their work suggests that the number of vortices in a step-up street canyon is a function of the building-height ratio and the street-canyon width.

Previous literature contains few wind-tunnel data for step-up canyons. Soulhac et al. (2001) investigated pollutant transport in 2D step-up cavities using a combination of 3D laser Doppler anemometry and flame ionization detection. The step-up canyon that they considered had $H_d/H_u = 2$, $L = H_u$, $S = H_u$. They found that peak concentrations were similar in square and step-up canyons, with peak concentrations occurring near the upwind face of the cavity. Only Hoydysch and Dabberdt (1988) have considered the full 3D step-up canyon configuration, where they used $H_d/H_u = 1.5$, $L/H_u = 8$, $W/H_u \approx 2.67$, $S/H_u \approx 1.33$ (where W is the width of the buildings). Though extremely informative, their concentration measurements in the canyon suffer from poor spatial resolution, and they only diagnosed the circulation patterns in the canyon using bubble tracers.

In terms of general street-canyon flows, Hussain and Lee (1980) first proposed the well-known flow regime classification for pairs of cubical buildings resulting in street canyons of varying canyon widths (S). Based on wind-tunnel experiments, it was proposed that the flow regime in the canyon is a function of the aspect ratio (H/S) of the street-canyon configuration. Three flow regimes: *isolated roughness flow*, *wake interference*, and *skimming flow* were identified for different H/S values. These flow regimes have been verified previously through wind-tunnel and field experiments, as well as numerical simulations (Hotchkiss and Harlow 1973; DePaul and Sheih 1986; Oke 1987, 1988; Hunter et al. 1990; Sini 1996; Kim and Baik 1999; Baik et al. 2000; Chang 2001, 2003; Xueling and Fei 2005; Jiang et al. 2007; Salizzoni et al. 2009). From these studies, it is evident that the flow regimes in a street canyon are a function of the interaction of the wakes of the upwind and downwind buildings, and hence this classification has been extended beyond cubical buildings. For example, Baik et al. (2000) observed flow patterns in deep canyons where the number of street-canyon vortices is a function of the building heights. Ohba (1998) and Addepalli and Pardyjak (2007) reported on flow fields in step-down canyons, where the circulation in the canyon was largely driven by the taller upwind building. The new flow patterns, though not formally classified as regimes, as with the previous counterparts (Hussain and Lee 1980), are a function of the degree of the

interaction of the wakes of the buildings forming the canyon. Since real-world downtown areas are rarely comprised of cubical buildings, a qualitative classification of flow patterns in simple two building street canyons comprising tall buildings can help understand flow fields in more complex urban settings.

Based on the above-mentioned studies, it is evident that no work to date has reported high-resolution wind-tunnel measurements in idealized step-up canyons that include the effects of spanwise (lateral) flow into the canyon (although Kastner-Klein et al. (2004) report on lateral inflow into idealized canyons of different spanwise widths and roof shapes). Also, none of the aforementioned work focuses exclusively on isolated step-up canyons. High spatial resolution wind-tunnel data for isolated street canyons can help extend the existing flow regime classifications, and can be used in the development of parametrizations for fast response and empirical flow models, and in the validation of CFD codes. The current work therefore aspires to contribute to the existing knowledge of flow in urban environments.

2 Experimental Details

The experiments were performed at the environmental fluid dynamics (EFD) laboratory at the University of Utah, at an atmospheric pressure of approximately 86.5 kPa, temperature of 21.5 °C, in a 7.9-m long boundary-layer wind-tunnel facility (shown in Fig. 1), with a cross-section of 0.61 m × 0.91 m. LEGO® sheets with circular dimples of height 2 mm lined the floor of the tunnel and were used to produce a uniform rough-walled turbulent flow. All of the experiments were run at a mean streamwise freestream velocity of $u_\infty \approx 5 \text{ m s}^{-1}$. The corresponding mean streamwise velocity at the downwind building height (H_d) in the boundary layer (without the buildings) was $u_{H_d} \approx 4.32 \text{ m s}^{-1}$. The boundary-layer depth (δ) and power-law exponent (η) at the measurement location were $\delta \approx 240 \text{ mm}$ ($\delta/H_d \approx 2.5$) and $\eta \approx 0.21$. The aerodynamic roughness length (z_0) and the friction velocity (u_*) were $z_0 \approx 0.15 \text{ mm}$ and $u_* \approx 0.26 \text{ m s}^{-1}$. The Reynolds number based on the downwind building height (Re_{H_d}) ($Re_{H_d} = u_{H_d} H_d / \nu$) was $Re_{H_d} \approx 27,648$, and the roughness Reynolds number (Re_{z_0}) ($Re_{z_0} = u_* z_0 / \nu$) was $Re_{z_0} \approx 2.6$.

Two different street-canyon configurations with building-height ratios of $H_d/H_u \approx 3$ and $H_d/H_u \approx 1.67$ were considered for the present set of experiments. For each configuration, the cross-wind widths of the upwind and downwind buildings were simultaneously varied. The street-canyon width (S) and the along-wind building lengths (L) were kept constant for these experiments, with $L \approx S$. The cross-wind widths were varied uniformly from $W \approx 1S$ to $W \approx 4S$, in increments of $1S$. This resulted in four cases for each configuration (fixed H_d/H_u value), and a total of eight experiments were conducted. Definitions of critical dimensions are given in Fig. 2. Also shown in Fig. 2 is the region in the vertical symmetry plane where the measurements were acquired.

The physical dimensions of the building models in the first configuration ($H_d/H_u \approx 3$) were, $L \approx S \approx 32 \text{ mm}$, $H_u \approx 32 \text{ mm}$, $H_d \approx 96 \text{ mm}$, and $W/S \approx 1, 2, 3, 4$ respectively. The physical dimensions of the building models in the second configuration ($H_d/H_u \approx 1.67$) were, $L \approx S \approx 32 \text{ mm}$, $H_u \approx 57.6 \text{ mm}$, $H_d \approx 96 \text{ mm}$, and $W/S \approx 1, 2, 3, 4$ respectively.

Based on the value of $\delta/H_d \approx 2.5$, it should be noted that the configurations considered in the current work correspond to tall building urban-street canyons. The blockage effects due to the presence of the buildings in the wind tunnel were characterized through velocity measurements using pitot-static probes, and were not found to be significant. The pressure gradient induced along the tunnel centreline in the measurement section due to the presence

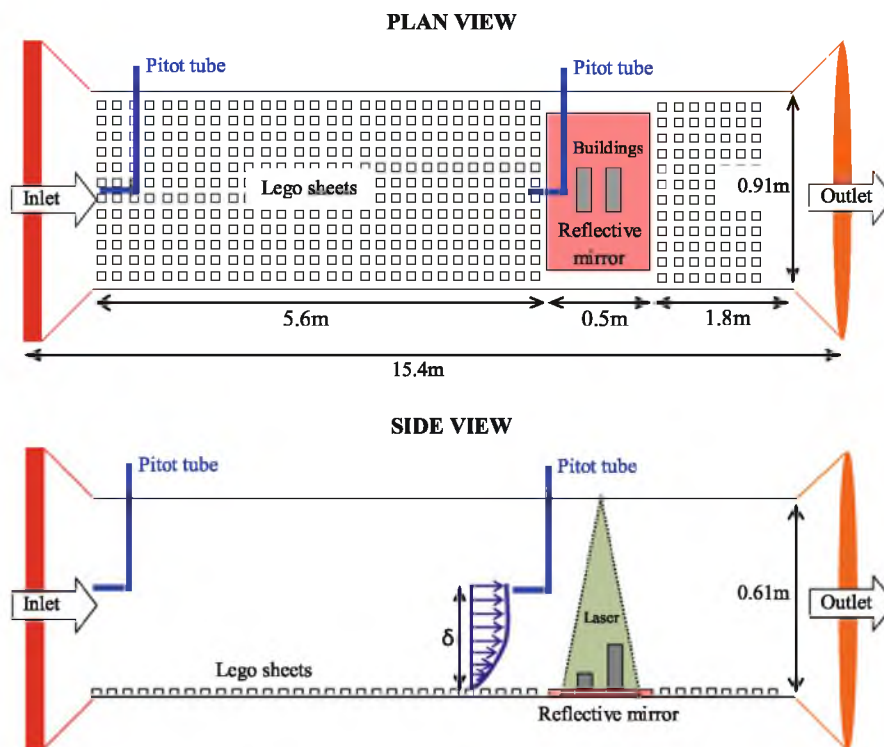


Fig. 1 Schematic of the wind tunnel used to conduct experiments in the present study (figure not to scale)

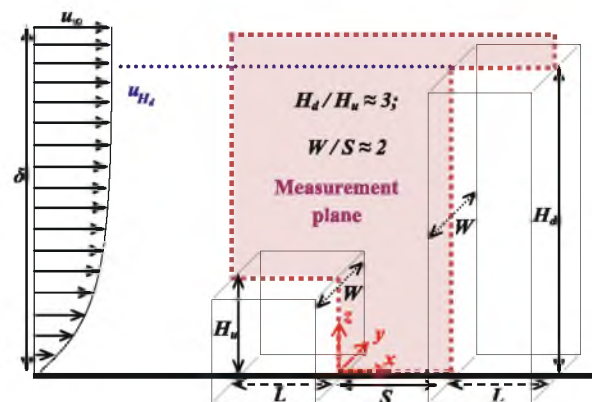


Fig. 2 Schematic showing the various terms used to define a step-up canyon (figure not to scale)

of the buildings was $\approx 2.5 \text{ Pa m}^{-1}$. The relative increase in the tunnel centreline velocity due to the presence of the buildings was $\approx 2.5 \%$.

Since step-up street canyons have different (and unique) flow features when compared to square or deep canyons, some of the flow regions of interest in step-up canyons are defined in Fig. 3b. The results obtained from the experiments, which will be discussed in Sect. 4, will

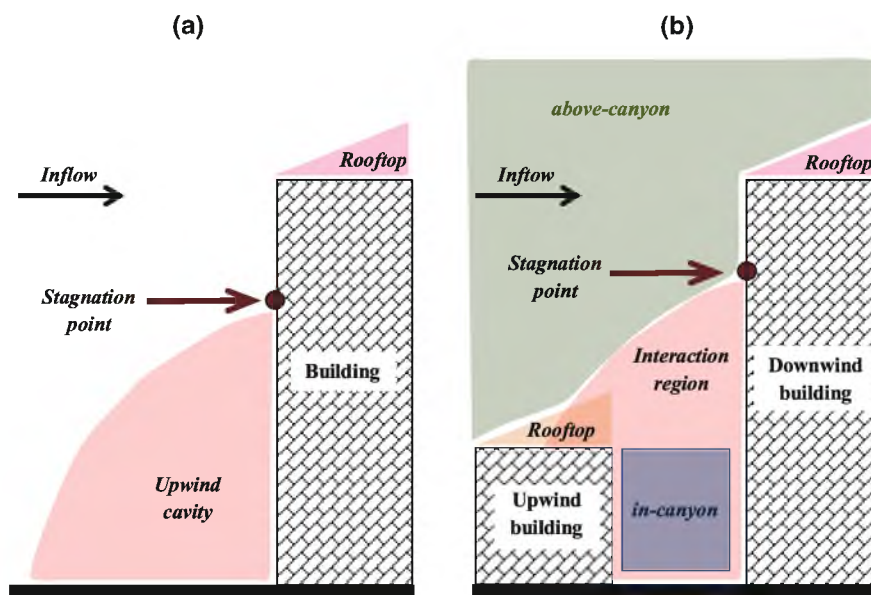


Fig. 3 Schematic defining the various flow regions in, **a** the vicinity of an isolated tall building, **b** a step-up canyon

use the terminology defined in Fig. 3b. In Fig. 3a, two prominent flow regions in the flow over an isolated building are identified. The regions are the upwind cavity region and the rooftop recirculation region. A step-up canyon is formed when a building is placed upwind of the building in Fig. 3a, such that its height is less than the downwind building height, as shown in Fig. 3b. In step-up canyons, the term *in-canyon* is used to define the region between the upwind and downwind buildings starting from the ground up to the height of the upwind building rooftop. The interaction region corresponds to the region above the *in-canyon* region, comprising part of the upwind building rooftop cavity, and below the stagnation point on the downwind building. The rationale behind defining an interaction region is based on the premise that the flow in the vicinity of the upwind building is influenced by the downwind building's upwind cavity, and the flow in the vicinity of the downwind building is affected by the presence of the upwind building. The term *rooftop* corresponds to the rooftop recirculation regions that might form either on the upwind or downwind buildings. The *above-canyon* region is defined as the region that does not include any of the aforementioned regions (*in-canyon* + *interaction region* + *rooftop*).

In the experiments conducted, two-dimensional (2D) particle image velocimetry (PIV) was used as the measurement technique. The measurements were taken along the vertical symmetry plane (x - z plane) of the model buildings (shown in Fig. 2). The flow was seeded with olive oil particles having a mean diameter of approximately $0.45 \mu\text{m}$, generated using two Laskin nozzles. According to Melling (1997) these particles should be approximately non-inertial and non-buoyant. The aerosols were illuminated with a 532-nm wavelength laser sheet (1.5 mm thick), generated using a 50 mJ NewWave Research (Fremont, CA) Solo PIV III Nd-Yag laser. A 4.0 MP ($2,048 \times 2,048$ pixels) CCD camera manufactured by TSI Inc. (Shoreview, MN) having a frame rate of 17 frames per second (fps) was used in conjunction with a frame grabber for image acquisition. The image acquisition rate was set to 2 fps.

A LASERPULSE synchronizer was used to control the timing between the laser pulses and the camera shutter open time through a PC desktop computer. Analysis of the acquired image pairs was done using TSIINSIGHT3G analysis software. Fast Fourier transform (FFT) based cross-correlation analysis was performed on the conditioned image pairs by dividing them into 32×32 pixel interrogation regions. One thousand image pairs were considered for computing the average velocity and turbulence fields. The spatial resolution of the final datasets obtained was ≈ 1.05 mm.

3 Validation Experiments

One thousand image pairs were deduced to be sufficient for computing the various mean and turbulence statistics by first running the $H_d/H_u \approx 3$, $W/S \approx 1$ test case, and plotting the cumulative moving average (CMA) of the various statistics at different spatial locations in the domain. Additionally, the PIV system was also tested and validated using the hot-wire data of Snyder and Lawson (1994) (hereafter SL94). PIV data were acquired for all the SL94 configurations for normal approach flow. However, for conciseness, only the results for an isolated tall building with $H/L \approx 3$, $W \approx L$ are presented.

Figure 4 shows the inflow velocity and turbulence intensity profiles obtained using 2D PIV. The PIV profiles have been plotted against SL94 inflow data. In Fig. 4, \bar{u} represents the mean streamwise velocity, u_H is the mean streamwise velocity at the building height (H) in the boundary layer without the buildings, and $\sigma_u(z)$ and $\sigma_w(z)$ are the streamwise and vertical velocity standard deviations at elevation z . Figure 4b, c shows that the turbulence intensity in the approach flow of SL94 is higher than that observed in the PIV data. The differences in the inflow turbulence intensities could be due to the differences in the boundary-layer generating mechanisms between SL94 and the current work. In SL94, the boundary layer was generated using ‘spires’ and wind-tunnel floor roughness, whereas in the present work, only Lego sheets as floor roughness were used. Figure 4d shows the comparison between 2D PIV and SL94 data along the vertical symmetry plane (x - z plane) in the wake of a tall building ($H/L \approx 3$, $W \approx L$). The velocity vectors in the figure were scaled by the streamwise velocity at the building height (u_H). Also, high spatial resolution 2D PIV measurements were fit to the sparse SL94 grid (locations where measurements were acquired) for comparison. Figure 4d shows that the wake structure predicted by the hot-wire and PIV data agree reasonably well ($\approx 14\%$ difference between the mean velocities measured using the two techniques). Minor differences can be observed in terms of the lengths of the near-wake region. One possible explanation for this discrepancy could be the higher inflow turbulence intensity associated with the SL94 case, leading to slightly smaller recirculation regions compared to the PIV experiments.

Based on the SL94 test cases used for validation, it was concluded that the 2D PIV system was performing satisfactorily in computing the velocity fields in the vicinity of the model buildings. Hence, with this acquired confidence in measurements, data were taken for the various configurations described in Sect. 2.

4 Results and Discussion

4.1 Mean Vertical Velocity Behaviour

In this section, mean flow patterns in step-up canyons for the configurations $H_d/H_u \approx 3$ and $H_d/H_u \approx 1.67$ are discussed.

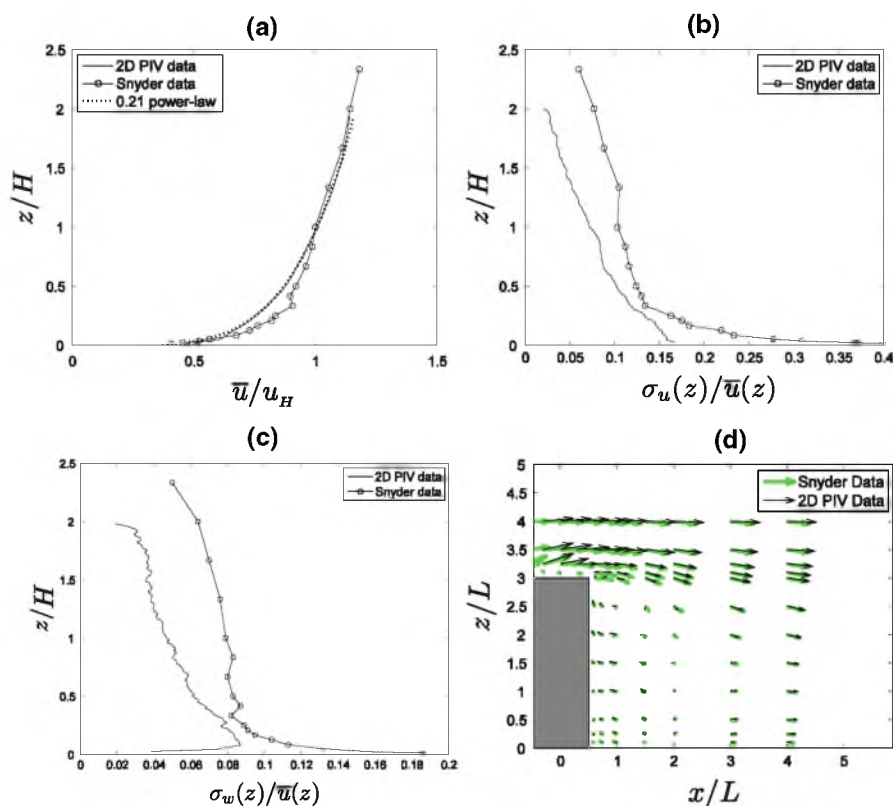


Fig. 4 Comparison of 2D PIV and (Snyder and Lawson 1994) hot-wire data for an isolated tall building ($H/L \approx 3$; $W \approx L$). Frames show comparison of the mean, a inflow streamwise velocity, b inflow streamwise turbulence intensity, c inflow vertical turbulence intensity, and d velocity vectors in the building wake. Note that the velocity vectors in d have been scaled by u_H

4.1.1 Canyon Configurations: $H_d/H_u \approx 3$, $W/S \approx 1$ to 4

Figure 5 shows mean vertical velocity (\bar{w}) contours and streamline patterns for all four test cases. From the figure, one can observe that the flow structure in step-up canyons is fundamentally different from the classical *skimming flow* regime (Hussain and Lee 1980) observed in square canyons (with $S = H$). In the *skimming flow* regime, the flow separating from the upwind building rooftop and sidewalls *skims* over the top and the side surfaces of the canyon (the volume between the buildings), in a manner similar to a lid driven cavity flow. Due to the intermittent nature of turbulent flows (which results in the *flapping* of the shear layers separating from the upwind building), the degree of penetration of the rooftop and sidewall flows into the canyon varies. In comparison to the *skimming flow* regime, the flow structure observed in step-up canyons is due to the combination of the flow separating over and around the upwind building, as well as the strong vertical motions induced in the upwind cavity of the downwind building (since for the cases considered, the upwind building is below the stagnation line of the downwind building). In the step-up canyons considered, since the flow separating over the upwind building rooftop does not have an escape route directly

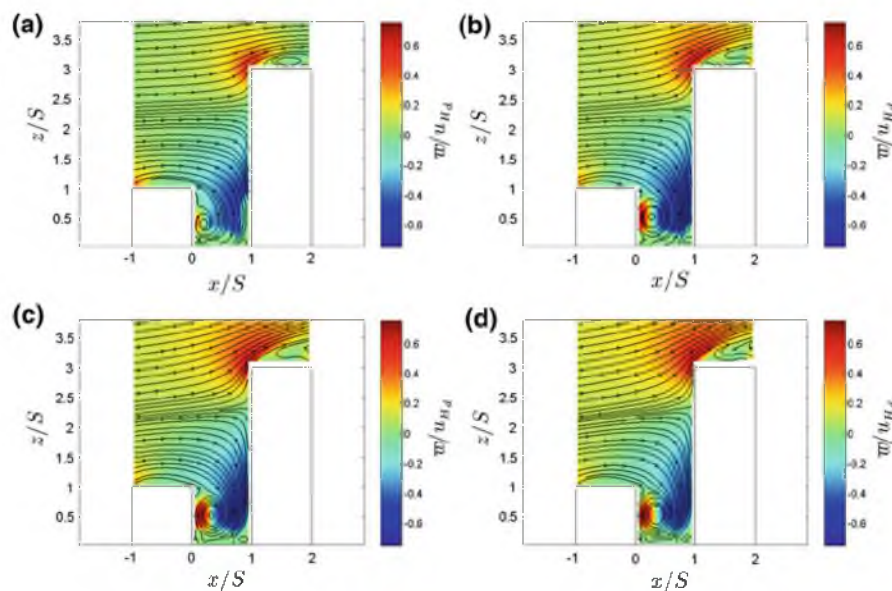


Fig. 5 Contours of the normalized mean vertical velocity for the configuration $H_d/H_u \approx 3$, **a** $W/S \approx 1$, **b** $W/S \approx 2$, **c** $W/S \approx 3$, and **d** $W/S \approx 4$

over the downwind building rooftop, it is forced down (into the in-canyon region) by the vertical motions in the upwind cavity of the downwind building. Therefore, unlike the typical skimming flow regime, the vertical velocity components (downdrafts induced by the taller downwind building) in the interaction region play a significant role in determining the flow structure in the in-canyon region.

For the H_d/H_u values considered, the upwind building can be thought of as an obstacle in the upwind cavity of the downwind building. To corroborate this claim, the flow structure in the upwind region of isolated buildings with physical dimensions $H/L \approx 3$, $W/L \approx 2$, and $H/L \approx 3$, $W/L \approx 3$ is shown in Fig. 6. It is apparent that the flow structure in the upwind cavity of isolated buildings, with the same physical dimensions as those in the step-up canyons considered (downwind building), is similar to that observed in step-up canyons. Placing a building upwind of the taller downwind building merely modifies the flow structure in the vicinity of the downwind building.

In Fig. 5, as the building widths are increased from $W/S \approx 1$ –4, a slight change in the in-canyon flow structure (stronger updrafts, downdrafts, and the in-canyon vortex) is observed. The difference in the flow structure can be ascribed to the greater interaction between the rooftop and sidewall flows (over and around the upwind building) in the vertical symmetry plane at lower building widths. As the building widths are increased, the flow in the vertical symmetry plane is more shielded from the incoming flow from the upwind building sidewalls (sidewall shear layers), and hence a more persistent flow structure is observed at increasing building widths. In addition, there is also a marginal increase in downdraft strengths into the canyon with increasing building widths. The magnitudes of \bar{w} remain about the same for the cases $W/S \approx 2$ through 4. The maximum mean vertical velocity in the in-canyon region for all cases is $\approx 65\%$ of u_{H_d} , supporting the notion that step-up building structures cause high downdrafts in the canyon between the buildings.

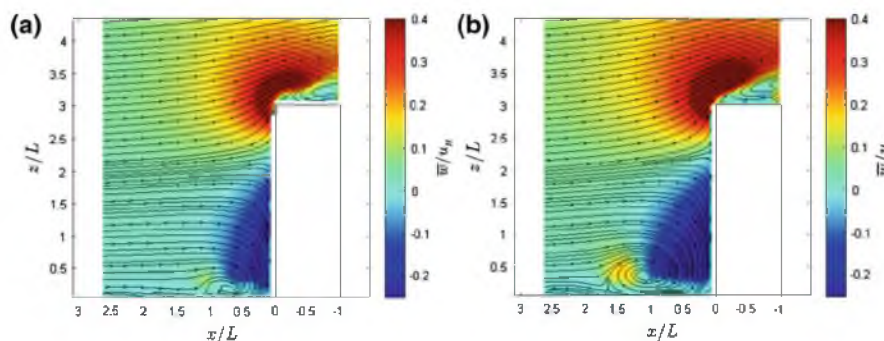


Fig. 6 Contours of the normalized mean vertical velocity for the configuration $H/L \approx 3$, **a** $W/L \approx 2$, and **b** $W/L \approx 3$

Changes in the above canyon, interaction region and downwind building rooftop flow patterns can be observed in terms of the changes in the curvature of the mean streamline patterns. As the building widths are increased, the separation angle at the downwind building windward edge and the size of the downwind building rooftop cavity increase. In fact, for $W/S \approx 1$, flow reattachment over the downwind building rooftop is observed, while at greater building widths, penetration of the downwind building wake flow into the downwind building rooftop cavity is observed. These changes can be attributed to the increased flow blockage due to an increase in building widths, resulting in greater flow acceleration around the buildings and thereby stronger wakes. Based on the mean streamline patterns, no conclusions can be made about the existence or non-existence of a rooftop cavity over the upwind building.

As the building widths increase from $W/S \approx 1$ to 2, a secondary vortex is observed in the lowest third of the canyon, close to the downwind building windward face. As with the primary vortex, the size and shape of the secondary vortex remains consistent for $W/S \approx 2$ through 4. These conclusions were made by zooming-in on the secondary vortex, but are not presented here to aid conciseness. The formation of the secondary vortex can again be attributed to greater rooftop and sidewall flow interaction along the vertical symmetry plane at lower building widths, and greater shielding from the sidewall flow at increasing building widths. Substantial changes in the stagnation point heights on the downwind building are not observed as the building widths are increased.

4.1.2 Canyon Configurations: $H_d/H_u \approx 1.67$, $W/S \approx 1$ to 4

Figure 7 shows contours of \bar{w} and mean streamline patterns for all four test cases. The results obtained for these cases are quite unique and have not been reported before in the street-canyon literature. For building width $W/S \approx 1$, the mean streamline patterns suggest the simultaneous existence of two co-rotating vortices near the upwind building leeward face (in the in-canyon region). The primary vortex for this case is defined as the one closer to the upwind building rooftop. It is seen that the size of the primary co-rotating vortex in this case is much larger than the secondary co-rotating vortex. When the building widths are increased to $W/S \approx 2$, the dual co-rotating vortex pair continues to exist, but with a smaller primary vortex and a larger secondary vortex. As the building widths are further increased to $W/S \approx 3$ and $W/S \approx 4$, more stable flow patterns are observed in the in-canyon region. The flow patterns are characterized by a counter-rotating vortex pair. The primary vortex, in this case, is again defined as the vortex closer to the upwind building roof height, while the

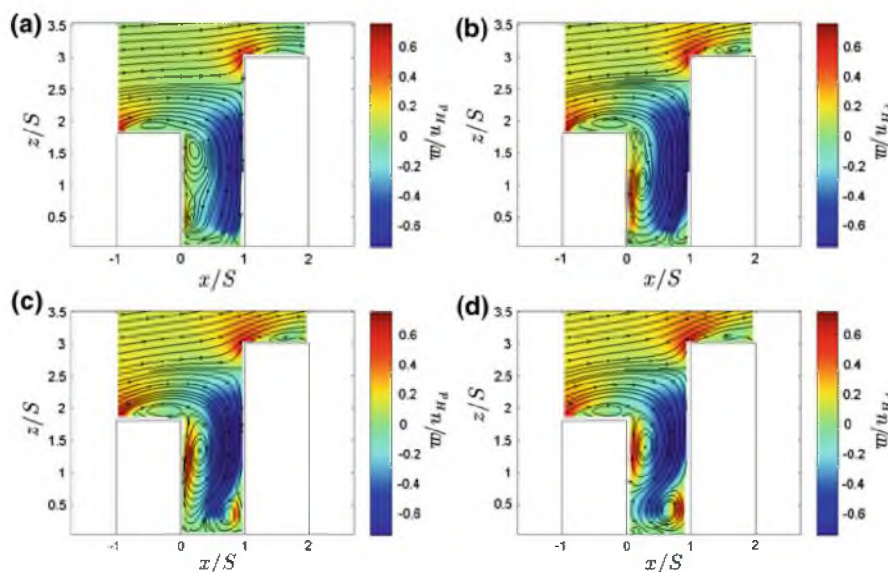


Fig. 7 Contours of the normalized mean vertical velocity for the configuration $H_d/H_u \approx 1.67$, **a** $W/S \approx 1$, **b** $W/S \approx 2$, **c** $W/S \approx 3$, and **d** $W/S \approx 4$

secondary vortex is near the downwind building windward face. The secondary vortex exists even for $W/S \approx 1$, and its size increases as the building widths are increased. The unusual flow patterns observed along the vertical symmetry plane for the cases $H_d/H_u \approx 1.67$, $W/S \approx 1$ to 4 can be attributed to the varying levels of interaction between the rooftop and sidewall flows entraining flow into the in-canyon region. The $H_d/H_u \approx 1.67$, $W/S \approx 1$ configuration represents a street-canyon configuration comprising slender buildings. Consequently, the path of least resistance for the inflow is around sidewalls of the upwind and downwind buildings. Hence, there is greater interaction between the in-canyon flow and that entraining into the in-canyon region around the upwind building sidewalls. The flow patterns observed in the in-canyon region are a result of the interaction between the upwind building rooftop cavity, the shear layers separating from the upwind building trailing edge, the primary vortex, the downdrafts induced by the downwind building, the upwind building sidewall flow entraining into the vertical symmetry plane, and the secondary vortex. The effect of the sidewall flow into the canyon on the average flow structure is much greater at lower building widths. Therefore, less stable flow patterns are observed at lower building widths. Also, since at greater building widths the in-canyon flow is more shielded from the sidewall flow into the canyon, the formation of a secondary counter-rotating vortex in the lower leg of the canyon is observed.

To further investigate the interesting flow structures observed in the $H_d/H_u \approx 1.67$ case, the instantaneous streamline patterns in the canyon are plotted and discussed in Sect. 4.2. To ensure that the flow patterns observed for $W/S \approx 1$ are not a result of unconverged velocity statistics, frequency histograms of the instantaneous vertical velocities were plotted at two locations in the canyon close to the upwind building leeward face (and the cumulative moving average (CMA) was computed). The plots of the CMA are not shown for conciseness. The frequency histograms are shown in Fig. 8. The coordinates of the locations where the histograms are plotted (and CMA values were computed) are, Fig. 8a: $(x/S \approx 0.25, z/S \approx$

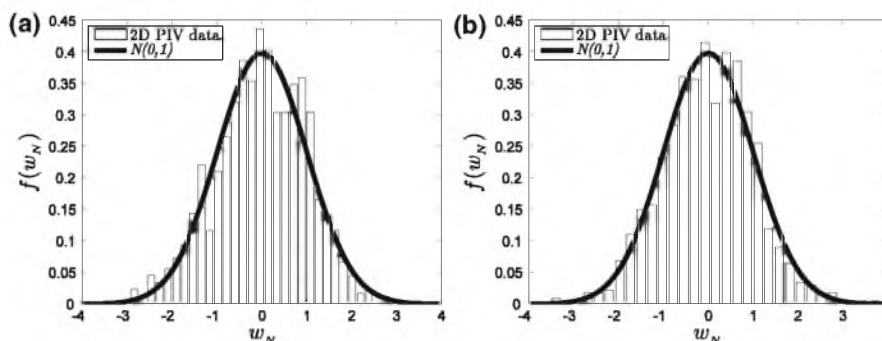


Fig. 8 Comparison of the histogram of the standardized instantaneous vertical velocities against the standard normal density $N(0,1)$ for $H_d/H_u \approx 1.67$, $W/S \approx 1$ at **a** ($x/S \approx 0.25$, $z/S \approx 0.5$), **b** ($x/S \approx 0.25$, $z/S \approx 1.5$)

0.5), and Fig. 8b: ($x/S \approx 0.25$, $z/S \approx 1.5$). In the histograms, the instantaneous vertical velocities (\bar{w}) at these locations were centralized and normalized ($w_N = (\bar{w} - \bar{w}) / \sigma_w$) to compare the histogram with the standard normal density ($N(0,1)$). Figure 8 indicates that although the locations at which the histograms are plotted correspond to regions of highly intermittent flow, the histograms resemble the normal density. Also, the CMA does not exhibit any unusual behaviour. This is surprising given that the intermittent nature of turbulent flows is usually ascribed to be the root cause for the deviation from normality of turbulent flow statistics.

Figure 7 indicates that, contrary to the $H_d/H_u \approx 3$ configurations, a well-defined rooftop cavity exists over the relatively taller upwind building. The rooftop cavity formation can be attributed to the increased flow acceleration (in comparison to $H_d/H_u \approx 3$) as a result of increased blockage. Also, since taller building rooftops are in regions of higher inflow velocities, this factor also contributes to the increased flow acceleration, and thereby the rooftop cavity formation. The rooftop cavity size increases from $W/S \approx 1$ to $W/S \approx 2$, and remains about the same at greater building widths. For $W/S \approx 1$, flow reattachment over the downwind building rooftop is observed. For $W/S \approx 2$ and $W/S \approx 3$, penetration of the downwind building rooftop cavity by the downwind building wake flow is seen. Also, the downwind building rooftop cavity size increases as the building widths increase from $W/S \approx 1$ to $W/S \approx 4$. All of these effects can again be attributed to increased velocities in the vicinity of buildings as a result of increased blockage. As for $H_d/H_u \approx 3$, no substantial change in the stagnation point height on the downwind building is observed for the reported cases. As the building widths are increased from $W/S \approx 1$ to $W/S \approx 2$, stronger downdrafts in the in-canyon region are observed. Though the magnitude of the maximum downdrafts remains the same at increasing building widths, their locations differ. This is due to the formation of the secondary vortex at greater building widths. The maximum mean vertical velocity in the in-canyon region for all the cases is $\geq 65\%$ of u_{H_d} . As the building widths are increased, the magnitude of the updrafts induced by the secondary (counter-rotating) vortex substantially increase, with the magnitudes of the updrafts induced by the primary and secondary vortices becoming almost equal.

4.2 The In-canyon Flow Structure

The results shown in Figs. 5 and 7 illustrate the importance of accounting for the momentum transport into the canyon in the lateral direction (x - y plane). Results from the 2D

Table 1 The mean spanwise vorticity flux for $H_d/H_u \approx 3$, $W/S \approx 1$ to 4

$H_d/H_u \approx 3$	$W/S \approx 1$	$W/S \approx 2$	$W/S \approx 3$	$W/S \approx 4$
$\int_A \bar{\omega}_y dA$ ($\text{m}^2 \text{s}^{-1}$)	42.8	75.6	57.5	46.8

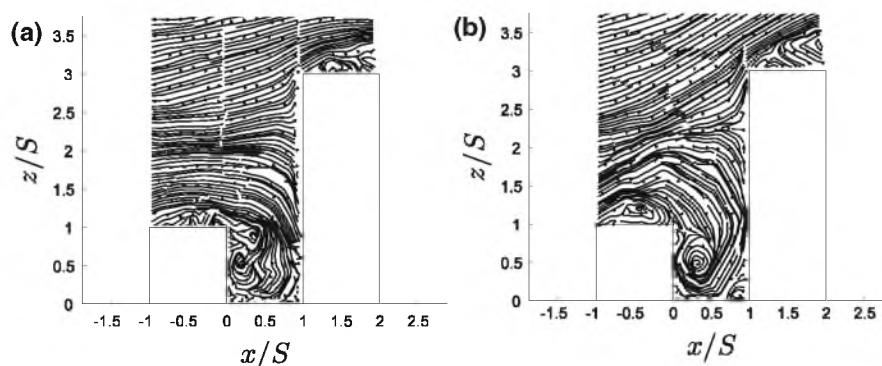
numerical simulations for step-up street canyons performed by [Assimakopoulos et al. \(2003\)](#); [Xie et al. \(2005\)](#); [Santiago and Martin \(2005\)](#) and [Yang et al. \(2007\)](#) show street-canyon vortices with different geometrical features than those reported herein. Differences can be found in the shape of the street-canyon vortex, the locations of the vortex core, as well as the magnitudes of the downdrafts in the canyon. All the 2D numerical simulations predict a street-canyon vortex with its vortex core either at the centre of the in-canyon, or slightly displaced towards the downwind building. Also, these studies underpredict the magnitude of the downdrafts near the downwind building windward face. The differences between the 3D experimental and the 2D computational results can be ascribed to the ventilation of the incoming flow in the lateral direction (x - y plane) around the downwind building. The differences can also be understood from the viewpoint of mass conservation. Since the magnitudes of the downdrafts are generally greater than the updrafts, in a 2D simulation, the area of the downdraft region (in the in-canyon region) should be smaller than the updraft region. This explains why the in-canyon vortex core occurs at either the canyon centre, or closer to the downwind building windward face in 2D simulations. The experimental data for 3D configurations indicate that the vortex core is closer to the upwind building leeward face. This is possible only if there is ventilation of the flow in the lateral direction to satisfy mass conservation (if not, there will be accumulation of mass in the downdraft region).

Examining the mean velocity field for step-up canyons with $H_d/H_u \approx 3$, it appears that for the street-canyon widths considered here, increasing the upwind and downwind building widths by the same factor does not result in a substantial change in the mean flow patterns in the canyon. However, changing the building widths does result in a change in the net circulation in the in-canyon region. Table 1 shows the mean spanwise vorticity flux ($= \int_A \bar{\omega}_y dA$; where, $\bar{\omega}_y = \partial \bar{u} / \partial z - \partial \bar{w} / \partial x$, and A = area of the in-canyon region) for the various cases. The data in Table 1 indicate that, as the building widths are increased from $W/S \approx 1$ to $W/S \approx 2$, the net circulation in the in-canyon region increases (the downdrafts in the in-canyon region are higher for $W/S \approx 2$ than for $W/S \approx 1$), and then decreases again; apparently, approaching the value for $W/S \approx 1$ at greater building widths.

The net circulation in the in-canyon region for $H_d/H_u \approx 1.67$ is shown in Table 2. Table 2 shows that, similar to the previous case, the net circulation in the in-canyon region increases as the buildings widths are increased from $W/S \approx 1$ to $W/S \approx 2$, and decreases for greater building widths. The behaviour observed may be attributed to the changes in flow patterns for different building widths. At greater building widths ($W/S \approx 3$ and $W/S \approx 4$), the formation of the secondary vortices results in a decrease in the net circulation, as the vorticity fluxes in the primary and secondary vortices will be of the opposite sign. As the building widths are increased from $W/S \approx 1$ to $W/S \approx 2$, there is an increase in the downdrafts (stronger downdrafts) into the in-canyon region, as well as the formation of a more coherent in-canyon vortex, resulting in greater net circulation. Comparing the results in Table 1 to those in Table 2, it is observed that the magnitudes of the circulations for the taller upwind building case are substantially larger. This is a result of the substantially increased driving velocity at the top of the canyon for the taller upwind building case.

Table 2 The mean spanwise vorticity flux for $H_d/H_u \approx 1.67$, $W/S \approx 1$ to 4

$H_d/H_u \approx 1.67$	$W/S \approx 1$	$W/S \approx 2$	$W/S \approx 3$	$W/S \approx 4$
$\int_A \bar{\omega}_y dA$ ($\text{m}^2 \text{s}^{-1}$)	223.8	283.5	177.4	125.6

**Fig. 9** Instantaneous streamline patterns for $H_d/H_u \approx 3$, a $W/S \approx 1$, b $W/S \approx 4$

The instantaneous flow structure in urban street canyons can be very different from the mean flow structure due to the irregular velocity and pressure fluctuations induced by turbulence. This salient feature of turbulent flows enhances transport of momentum, kinetic energy, and contaminants. In this section, the instantaneous flow patterns in the canyon are described to illustrate how flow structures not observed in the mean flow may be present in the instantaneous flow, and might affect the transport and dispersion of contaminants.

Figure 9 shows instantaneous streamline patterns for $H_d/H_u \approx 3$, $W/S \approx 1, 4$. The snapshots were chosen to illustrate the salient (and sometimes counter-intuitive) features of step-up street-canyon flows. Figure 9 shows that in comparison to the mean flow, an upwind building rooftop cavity exists in the instantaneous flow. The cavity is quite prominent for $W/S \approx 4$. For $W/S \approx 1$, a dual co-rotating vortex pair is observed in the in-canyon region close to the upwind building leeward face. This flow structure appears to be similar to the one observed in $H_d/H_u \approx 1.67$, $W/S \approx 1, 2$. From the instantaneous flow, it is evident that the primary vortex (the vortex closer to the upwind building trailing edge) is a result of the shear layers separating from the upwind building being pushed into the in-canyon region by the strong downdrafts.

Figure 10 shows some instantaneous streamline patterns for $H_d/H_u \approx 1.67$, $W/S \approx 1$ to 4. For $W/S \approx 1$, two snapshots of the instantaneous flow are shown to illustrate the irregular nature of the instantaneous flow, and how it might affect the averaging process when computing the mean flow. For $W/S \approx 1$, it can be seen that in the instantaneous flow, the number of *in canyon* vortices vary. The number of vortices can be conjectured to be a function of the characteristics of the shear layer separating at the upwind building rooftop. For $W/S \approx 2$, the primary vortex is confined closer to the upwind building trailing edge. For $W/S \approx 3$, although a stable counter-rotating vortex pair is observed in the mean flow (Fig. 7), instantaneously, the entire in-canyon region can be occupied by a single vortex. For $W/S \approx 4$, the instantaneous flow reveals that the secondary counter-rotating vortex can even be larger than the primary vortex.

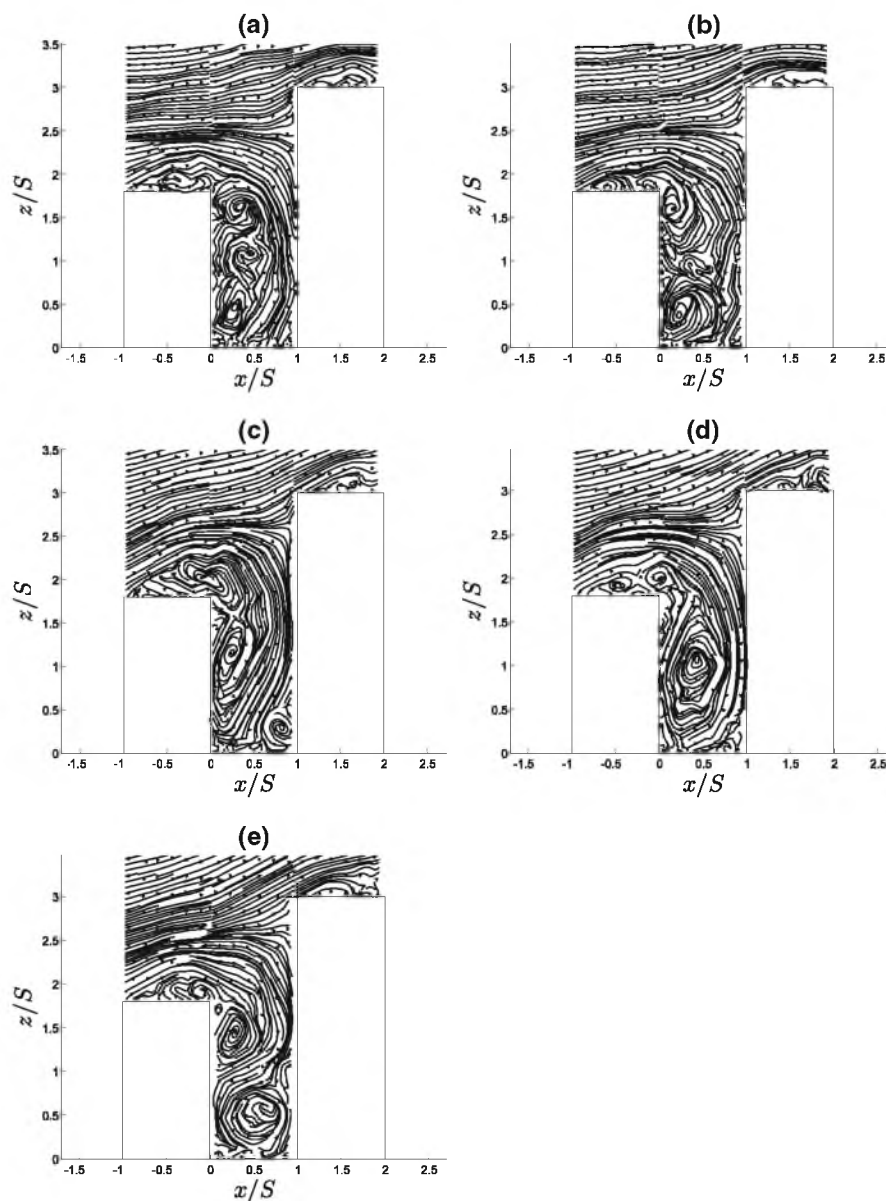


Fig. 10 Instantaneous streamline patterns for $H_d/H_u \approx 1.67$, **a** $W/S \approx 1$, **b** $W/S \approx 1$, **c** $W/S \approx 2$, **d** $W/S \approx 3$, **e** $W/S \approx 4$

4.3 Reynolds-Stress Distribution

The Reynolds stress is the contribution of turbulent motion to the mean stress tensor in the Reynolds-averaged Navier–Stokes equations, and is given by, $\tau_{ij} = -\rho \overline{u'_i u'_j}$ (Tennekes and

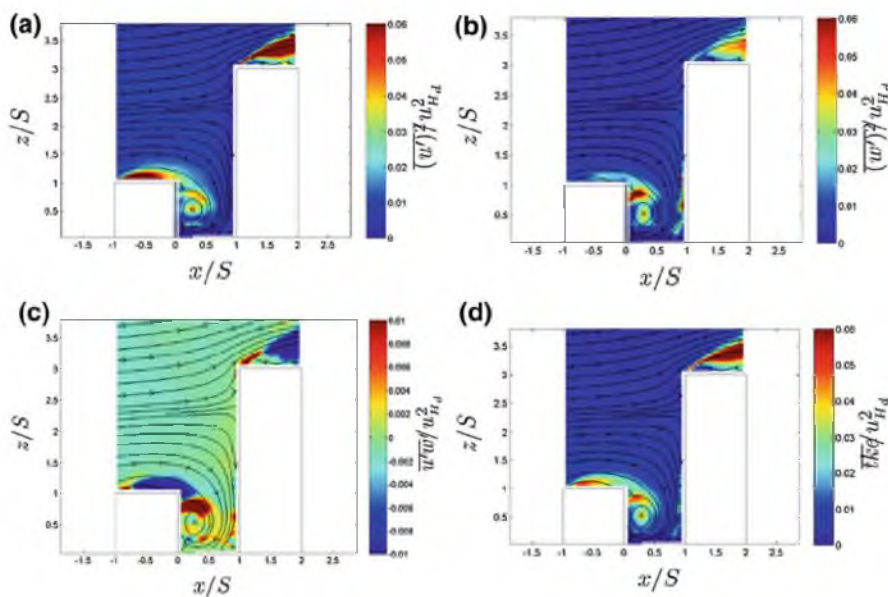


Fig. 11 For $H_d/H_u \approx 3$, $W/S \approx 2$, contours of normalized, **a** streamwise velocity variance, **b** vertical velocity variance, **c** mean Reynolds shear stress, **d** mean turbulent kinetic energy

Lumley 1972). It represents the average flux of j -momentum along the i -direction and vice versa (Kundu and Cohen 2007). Since the data acquired for the present work are 2D, four of the nine components of the Reynolds stress tensor were computed. In the following section, the normal stresses ($\overline{u'^2}$, $\overline{w'^2}$), turbulent kinetic energy ($\overline{tke} = [\overline{u'^2} + \overline{w'^2}]/2$), and Reynolds shear stress $\overline{u'w'}$ are discussed.

Measurements were made for the configurations: $H_d/H_u \approx 3$, $W/S \approx 1$ to 4. However, for conciseness, only representative contours of normalized Reynolds stresses and \overline{tke} for $H_d/H_u \approx 3$, $W/S \approx 2$ are presented. Figure 11 indicates that large values of Reynolds stresses occur in the vicinity of the buildings. Specifically, large values are observed in the upwind and downwind building rooftop cavities and in the in-canyon region. Negative values of the Reynolds shear stress in the upwind and downwind building rooftop cavities are indicative of a net downward flux of streamwise momentum in these regions. There is also an apparent advection of Reynolds stress from the upstream rooftop recirculation region down into the in-canyon region. In the above-canyon region, small and negative values of the Reynolds shear stress are observed. The behaviour of the Reynolds shear stress in this region is similar to that observed in a typical boundary layer with positive mean shear ($\partial \overline{u}/\partial z > 0$). Since in the above-canyon region $\partial \overline{u}/\partial z > 0$, there is transfer of x -momentum in the negative z -direction (resulting in negative $\overline{u'w'}$), as turbulence tends to diffuse the gradients. Relatively large positive values of Reynolds shear stress are observed in the in-canyon region suggesting either a net upward flux of horizontal momentum, or a net streamwise flux of vertical momentum. Positive, but relatively small, values of Reynolds shear stresses in street canyons were previously reported by Rotach (1993) through field experiments, by Kastner-Klein and Rotach (2004) through wind-tunnel studies, and by Kanda et al. (2004) and Gowardhan et al. (2007) through numerical simulations. In comparison to

the skimming flow regime (Gowardhan et al. 2007), relatively large positive Reynolds shear stresses occur in the in-canyon region of step-up canyons with $H_d/H_u \approx 3$. The positive Reynolds shear stresses observed are a result of the recirculating flow in the in-canyon region. Due to this, $\partial \bar{u}/\partial z$ and $\partial \bar{w}/\partial z$ are not always strictly positive, as in the case of a boundary layer.

Figure 11d shows contours of \overline{tke} in the canyon for $H_d/H_u \approx 3$, $W/S \approx 2$. Large values of \overline{tke} occur over the upwind and downwind building rooftops, and in the in-canyon region. Large values of \overline{tke} observed over the upwind and downwind building rooftops can be attributed to the separation occurring at the leading edges of these buildings, which causes non-periodic vortex shedding, thereby resulting in higher values of TKE. The values of \overline{tke} are higher over the downwind building rooftop than the upwind building rooftop. This is expected because the downwind building presents greater blockage to the incoming flow. Large values of \overline{tke} observed in the in-canyon region can be conjectured to be due to the downdrafts in the canyon. The downdrafts force the vortices shed off the upwind building into the in-canyon, resulting in significant fluctuations in the streamwise and vertical velocities. It is also worth noting that over the upwind and downwind building rooftops, the maximum value of \overline{tke} occurs not at the leading edge, but at some distance downwind of the leading edge. This can be conjectured to be due to the downstream advection of large values of TKE occurring at the leading edge by the mean flow.

For the configuration $H_d/H_u \approx 3$, $W/S \approx 2$, the maximum values of the Reynolds normal stresses ($\overline{u'^2}/u_{H_d}^2$ and $\overline{w'^2}/u_{H_d}^2$), and the turbulent kinetic energy ($\overline{tke}/u_{H_d}^2$) were, 0.13, 0.07, and 0.09. These values occurred at locations with the spatial coordinates, $(x/S, z/S) = (1.73, 3.36)$, $(0.19, 0.90)$, and $(1.77, 3.36)$. The maximum and minimum values of the Reynolds shear stress $\overline{u'w'}/u_{H_d}^2$ were, 0.05 and -0.04 . These values occurred at locations with spatial coordinates, $(x/S, z/S) = (1.11, 3.13)$ and $(1.96, 3.39)$.

For the configuration with the taller upwind building ($H_d/H_u \approx 1.67$), contours of the Reynolds normal and shear stresses are presented for $W/S \approx 4$ in Fig. 12. Most of the characteristics of the Reynolds stresses observed for $H_d/H_u \approx 3$, $W/S \approx 2$ are also present in the $H_d/H_u \approx 1.67$, $W/S \approx 4$ case. For this case, large positive values of Reynolds shear stress are observed in the primary vortex. In contrast, significant negative Reynolds shear stress values are observed in the updraft region of the secondary vortex, and significant positive values are seen in the downdraft region. It should be noted the behaviour, magnitude, and sign of the Reynolds shear stresses in step-up canyons with $H_d/H_u \approx 1.67$ is very different from that reported in previous wind-tunnel studies for street-canyon flows (see for example, Kastner-Klein and Rotach (2004)). The sign of the Reynolds shear stress can again be explained through the signs of \bar{u} , \bar{w} , $\partial \bar{u}/\partial z$, and $\partial \bar{w}/\partial z$ in this region, and is not done for conciseness.

Figure 12 shows a contour of \overline{tke} in the canyon for $H_d/H_u \approx 1.67$, $W/S \approx 4$. The behaviour of \overline{tke} in the canyon is similar to that observed for $H_d/H_u \approx 3$, $W/S \approx 2$. That is, \overline{tke} is quite large over the upwind and downwind building rooftops, and in the in-canyon region. The same reasoning used to explain the large values of \overline{tke} observed for $H_d/H_u \approx 3$, $W/S \approx 2$ can be used for $H_d/H_u \approx 1.67$; $W/S \approx 4$. For the configuration $H_d/H_u \approx 1.67$, $W/S \approx 4$, the maximum values of the Reynolds normal stresses ($\overline{u'^2}/u_{H_d}^2$, $\overline{w'^2}/u_{H_d}^2$), and the turbulent kinetic energy ($\overline{tke}/u_{H_d}^2$) were 0.13, 0.14, and 0.10. These values occurred at locations with the spatial coordinates, $(x/S, z/S) = (1.28, 3.12)$, $(0.77, 0.84)$, and $(0.64, 0.42)$. The maximum and minimum values of the Reynolds shear stress $\overline{u'w'}/u_{H_d}^2$ were 0.04 and -0.04 . These values occurred at locations with spatial coordinates, $(x/S, z/S) = (-0.81, 1.86)$ and $(0.06, 2.02)$.

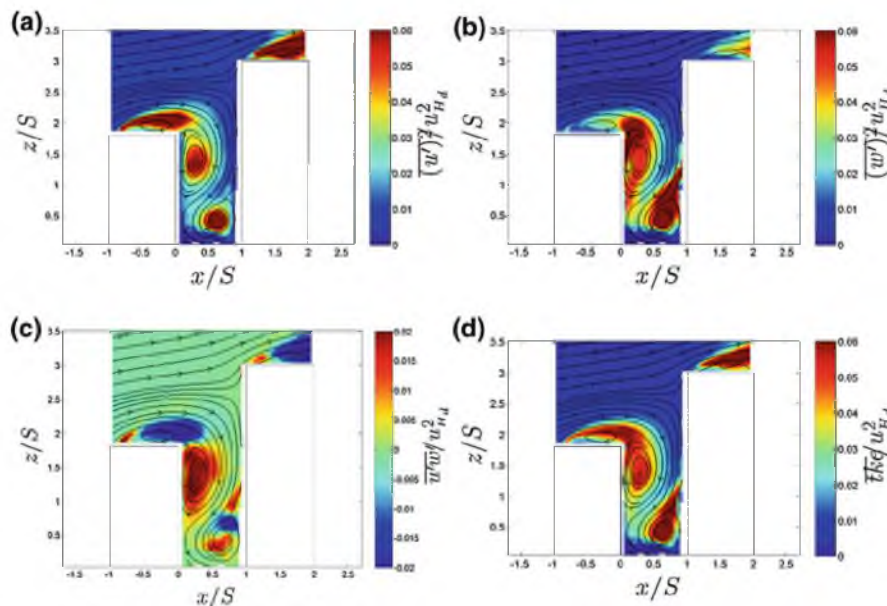


Fig. 12 For $H_d/H_u \approx 1.67$, $W/S \approx 4$, contours of normalized, **a** streamwise velocity variance, **b** vertical velocity variance, **c** mean Reynolds shear stress, **d** mean turbulent kinetic energy

4.4 Quadrant Analysis

Along with the mean values of the Reynolds shear stress ($-\overline{\rho u'w'}$), knowledge of the distribution of the fluctuations around the computed average is important to understand the mechanisms of momentum transfer between different regions of the flow by turbulence (Tennekes and Lumley 1972). In the classical turbulent boundary layer, the four quadrants of the $u' - w'$ sample space correspond to one of the four events, namely, sweeps, ejections, inward, and outward motions. In this paper, the four quadrants are called Q1 ($\bar{u} > \bar{u}; \bar{w} > \bar{w}$), Q2 ($\bar{u} < \bar{u}; \bar{w} > \bar{w}$), Q3 ($\bar{u} < \bar{u}; \bar{w} < \bar{w}$), and Q4 ($\bar{u} > \bar{u}; \bar{w} < \bar{w}$), as it is a more general definition of the various quadrants.

4.4.1 Canyon Configurations: $H_d/H_u \approx 3$, $W/S \approx 1$ to 4

As done previously for this configuration, only the results for $H_d/H_u \approx 3$, $W/S \approx 2$ are discussed. Quadrant analysis was performed at four locations in the canyon. The four locations are named L1, L2, L3, and L4. The x - and z -coordinates (x/S and z/S) of the four locations are: (1) L1: (0.5, 0.5), (2) L2: (0.25, 0.75), (3) L3: (-0.5, 1.12), and (4) L4: (0.5, 1.5). Figure 13 shows the distribution of (u' , w') at the four locations. Also shown in Fig. 13 is the percentage frequency of events occurring in each of the four quadrants, and the contributions of the various events to the computed value of the mean Reynolds shear stress at these locations. The method of data presentation is similar to that adopted in Cui et al. (2004).

The Reynolds shear stresses shown in Fig. 13 indicate that $(\overline{u'w'})_{L1} > 0$ (in the in-canyon region) and $(\overline{u'w'})_{L4} < 0$ (in the interaction region). Similar behaviour of the Reynolds shear stresses has been observed in skimming flow configurations (Gowardhan et al. 2007), wherein small positive values of Reynolds shear stresses are found in the lower regions of the canyon

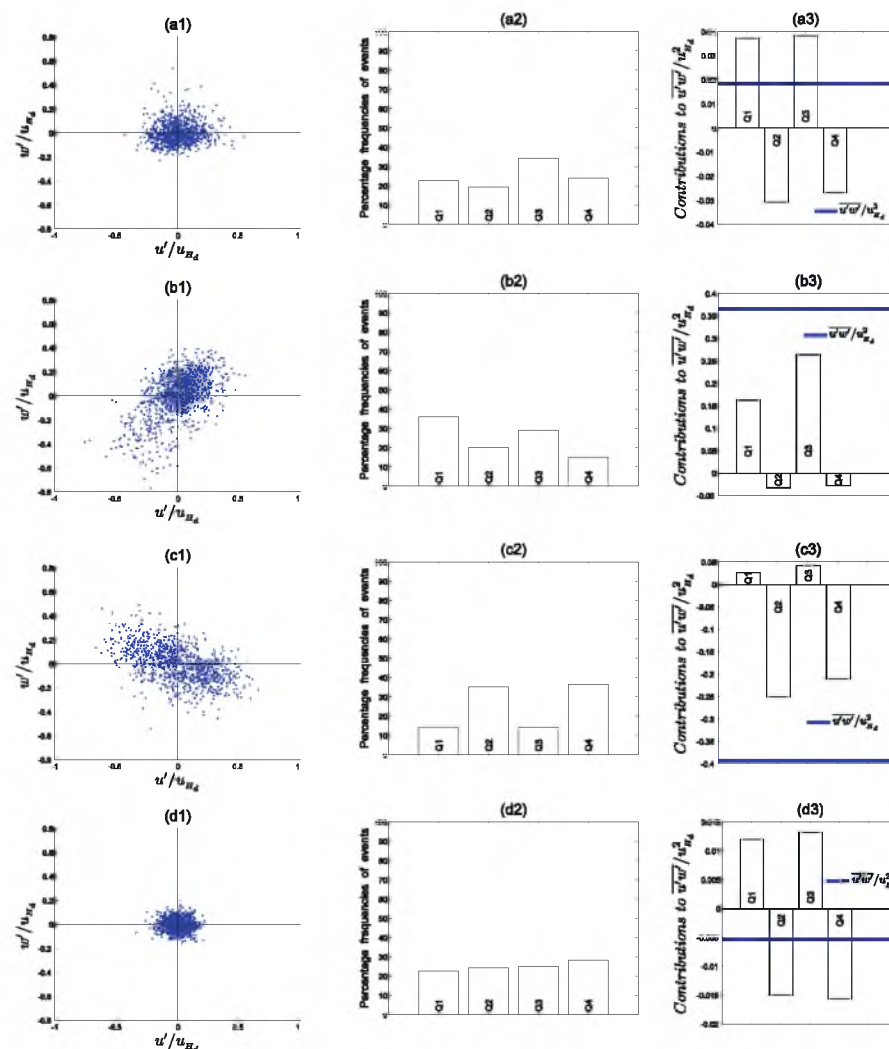


Fig. 13 For $H_d/H_u \approx 3$, $W/S \approx 2$, at locations L1 to L4, (a1–d1) distribution of streamwise and vertical velocity fluctuations, (a2–d2) percentage frequency distribution of events, (a3–d3) contribution of various events to computed value of mean Reynolds shear stress (indicated by a *solid horizontal line*)

(with contributions from all four quadrants), and negative values (Q2 and Q4 dominate) occur in the region above the canopy. For such flow regimes, the phrase *decoupling* is used to describe the behaviour of $\overline{u'w'}$ in and above the urban canopy. For normal approach flow and within the street canyon, the decoupling of Reynolds normal and shear stresses is conjectured to be due to the sheltering of the in-canyon flow from the above-canyon flow by the buildings. In step-up canyons, the flow in the in-canyon and interaction regions are not decoupled, thereby adding credence to the previous supposition that the upwind building for $H_d/H_u \approx 3$ can be thought of as an obstacle in the upwind wake of the taller downwind building. In the region comprising updrafts in the in-canyon (L2), $\overline{u} > 0$, $\overline{w} > 0$, $(\overline{u'w'})_{L2} > 0$, and the

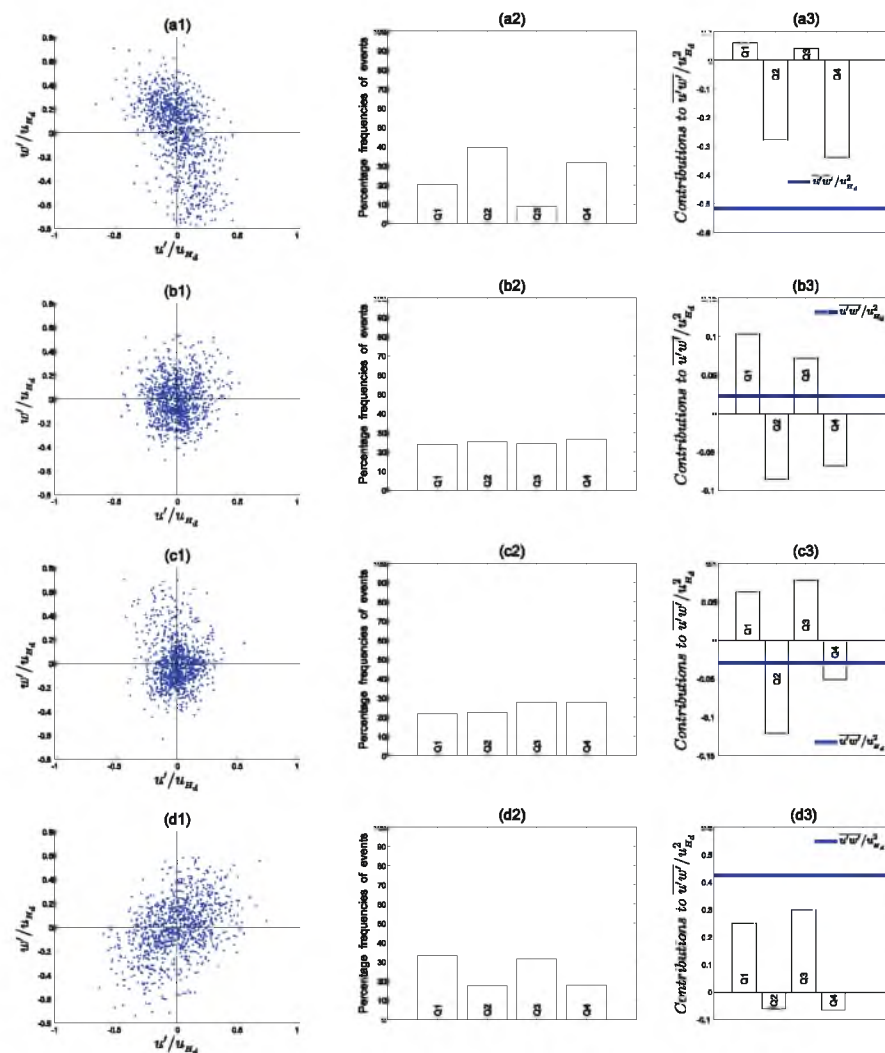


Fig. 14 For $H_d/H_u \approx 1.67$, $W/S \approx 4$, at locations G1 to G4, (a1–d1) distribution of streamwise and vertical velocity fluctuations, (a2–d2) percentage frequency distribution of events, (a3–d3) contribution of various events to computed value of mean Reynolds shear stress (indicated by a solid horizontal line)

scatter plot of (u', w') has a distinct polarity towards the first and third quadrants. At L3 (which is in the upwind building rooftop region), $\overline{u} > 0$, $\overline{w} < 0$, $(u'w')_{L3} < 0$, and Q2 and Q4 dominate, indicating that there is a net downward flux of horizontal momentum in this region.

4.4.2 Canyon Configurations: $H_d/H_u \approx 1.67$, $W/S \approx 1$ to 4

Quadrant analysis was performed for $W/S \approx 4$ at four locations in the canyon. The four locations are named G1, G2, G3, and G4. The x and z -coordinates (x/S and z/S) of the four

locations are: 1) G1: (0.75, 0.65), 2) G2: (0.15, 0.5), 3) G3: (0.5, 0.8), and 4) G4: (0.25, 1.45). Figure 14 shows the distribution of (u', w') pairs at the four locations.

Figure 14 shows that Q2 and Q4 events are the major contributors to $\overline{u'w'}$ at G1, which corresponds to the updraft region in the secondary vortex. Fewer Q4 events contribute more to the magnitude of $\overline{u'w'}$ in comparison to Q2 events. The location G2 was chosen to be in the downdraft region of the secondary vortex. In this region, $\overline{u'w'} > 0$, and all four quadrants contribute in almost equal measure to the computed value of the mean Reynolds shear stress. The location G3 was chosen to be in the interface between the primary and secondary vortices. At G3, though all events occur with almost equal frequency, the Q2 events contribute more to the total stress compared to Q1 and Q3 events, resulting in a net negative $\overline{u'w'}$. The location G4 is in the updraft region of the primary vortex. At G4, the scatter plot of (u', w') has a strong polarity towards the first and third quadrants, resulting in large positive values of $\overline{u'w'}$. The data in Fig. 14 indicate that the magnitude of $\overline{u'w'}$ is about the same in the updraft regions of the primary and secondary vortices, but the sign varies. Hence, for taller upwind building step-up canyons (e.g., $H_d/H_u \approx 1.67$) both strong positive and negative values of the Reynolds shear stress can occur in the in-canyon (sheltered) region.

5 Conclusions

A step-up street canyon is a street canyon in which the upwind building height (H_u) is less than the downwind building height (H_d). In this article, the effect of canyon geometry on the flow structure in isolated step-up street canyons is investigated through wind-tunnel 2D PIV measurements. The measurements were acquired along the vertical symmetry plane of the model buildings for normal approach flow. The building-height ratios considered were: $H_d/H_u \approx 3$, and $H_d/H_u \approx 1.67$. For each building-height ratio, the along-wind lengths (L) of the upwind and downwind buildings, and the street-canyon width (S) were kept constant, with $L \approx S$. The cross-wind widths (W) of the upwind and downwind buildings were varied uniformly from $W/S \approx 1$ through $W/S \approx 4$, in increments of $W/S \approx 1$. Our objective was to characterize the changes in flow structure as a function of W/S , for fixed L , S , and H_d/H_u values. Results obtained indicate that for $H_d/H_u \approx 3$, the mean and turbulence statistics do not vary significantly for the building widths considered. For $H_d/H_u \approx 3$, the upwind building almost behaves as an obstacle in the downwind building upwind cavity. The flow patterns observed in $H_d/H_u \approx 1.67$ configurations are unique and counter-intuitive, and depend strongly on W/S values. For the building widths $W/S \approx 1$ and $W/S \approx 2$, the sidewall flow into the canyon plays an important role in determining the in-canyon flow structure. Consequently, even the mean flow patterns are highly ambiguous at these building widths. At greater building widths, flow along the vertical symmetry plane is more shielded from the sidewall flow, and hence a stable counter-rotating vortex pair is observed in the canyon.

Acknowledgements We would like to thank Dr. Michael Brown for his help in developing the experimental strategy. This research was supported by a contract through Los Alamos National Laboratory.

References

- Addepalli B, Pardyjak ER (2007) Study of flow fields in asymmetric step-down street canyons. In: The international workshop on physical modelling of flow and dispersion phenomena (PHYSMOD 2007). University of Orleans, France

- Allwine KJ, Flaherty JE (2006a) Joint urban 2003: study overview and instrument locations. Tech. Rep. PNNL-15967, Pacific Northwest National Laboratory, 92 pp
- Allwine KJ, Flaherty JE (2006b) Urban dispersion program MSG05 field study: summary of tracer and meteorological measurements. Tech. Rep. PNNL-15969, Pacific Northwest National Laboratory, 27 pp
- Allwine KJ, Flaherty JE (2007) Urban dispersion program overview and MID05 field study summary. Tech. Rep. PNNL-16696, Pacific Northwest National Laboratory, 63 pp
- Allwine KJ, Shinn JH, Streit GE, Clawson KL, Brown MJ (2002) Overview of urban 2000: a multiscale field study of dispersion through an urban environment. *Bull Am Meteorol Soc* 83(4):521–536
- Assimakopoulos VD, ApSimon HM, Moussiopoulos N (2003) A numerical study of atmospheric pollutant dispersion in different two-dimensional street canyon configurations. *Atmos Environ* 37(29):4037–4049
- Baik JJ, Park RS, Chun HY, Kim JJ (2000) A laboratory model of urban street-canyon flows. *J Appl Meteorol* 39(9):1592–1600
- Beychok MR (2005) Fundamentals of stack gas dispersion, 4th edn. M.R. Beychok, Irvine, 193 pp
- Camelli FE, Hanna SR, Löhner R (2004) Simulation of the MUST field experiment using the feffo-urban cfd model. In: 8th annual George Mason University conference on atmospheric transport and dispersion modeling, Fairfax, VA, pp 531–544
- Chan ST, Leach MJ (2007) A validation of FEM3MP with Joint Urban 2003 Data. *J Appl Meteorol Clim* 46(12):2127–2146
- Chang CH (2001) Numerical and physical modeling of bluff body flow and dispersion in urban street canyons. *J Wind Eng Ind Aerodyn* 89(14):1325–1334
- Chang CH (2003) Concentration and flow distributions in urban street canyons: wind tunnel and computational data. *J Wind Eng Ind Aerodyn* 91(9):1141–1154
- Coirier WJ, Kim S (2006) CFD modeling for urban area contaminant transport and dispersion: Model description and data requirements. In: Sixth symposium on urban environment, 86th AMS Annual Meeting, Atlanta, GA, 11 pp
- Cui Z, Cai X, Baker C (2004) Large-eddy simulation of turbulent flow in a street canyon. *Q J R Meteorol Soc* 130(599):1373–1394
- DePaul FT, Sheih CM (1986) Measurements of wind velocities in a street canyon. *Atmos Environ* 20(3):455–459
- Gowardhan A, Pardyjak ER, Senocak I, Brown MJ (2007) Investigation of Reynolds stresses in a 3D idealized urban area using large eddy simulation. In: American Meteorological Society seventh symposium on urban environment, San Diego, CA, 8 pp
- Hanna S, Baja E (2009) A simple urban dispersion model tested with tracer data from Oklahoma City and Manhattan. *Atmos Environ* 43(4):778–786
- Hanna S, Hansen OR, Dharmavaram S (2004) FLACS CFD air quality model performance evaluation with Kit Fox, MUST, Prairie Grass, and EMU observations. *Atmos Environ* 38(28):4675–4687
- Hanna S, Brown MJ, Camelli FE, Chan ST, Coirier WJ, Hansen OR, Huber AH, Kim S, Reynolds RM (2006) Detailed simulations of atmospheric flow and dispersion in downtown Manhattan: an applications of five computational fluid dynamics models. *Bull Am Meteorol Soc* 87(12):1713–1726
- Hendricks EA, Diehl SR, Burrows DA, Keith R (2004) Dispersion in the downtown oklahoma city domain: comparison between joint urban 2003 and the rustic/meso models. In: 13th joint conference on the applications of air pollution meteorology with the air and waste management association, Vancouver, BC, Canada, pp 231–234
- Hotchkiss RS, Harlow HH (1973) Air pollution in street canyons. Tech. Rep. EPA R4-73-029, US EPA, 78 pp
- Hoydysh WG, Dabberdt WF (1988) Kinematics and dispersion characteristics of flows in asymmetric street canyons. *Atmos Environ* 22(12):2677–2689
- Hunter LJ, Watson ID, Johnson GT (1990) Modelling air flow regimes in urban canyons. *Energ Build* 15(3–4):315–324
- Hussain M, Lee BE (1980) A wind tunnel study of the mean pressure forces acting on large groups of low-rise buildings. *J Wind Eng Ind Aerodyn* 6(3–4):207–225
- Jiang Y, Liu H, Sang J, Zhang B (2007) Numerical and experimental studies on flow and pollutant dispersion in urban street canyons. *Adv Atmos Sci* 24(1):111–125
- Kanda M, Moriwaki R, Kasamatsu F (2004) Large-eddy simulation of turbulent organized structures within and above explicitly resolved cube arrays. *Boundary-Layer Meteorol* 112:343–368
- Kastner-Klein P, Rotach MW (2004) Mean flow and turbulence characteristics in an urban roughness sublayer. *Boundary-Layer Meteorol* 111:55–84
- Kastner-Klein P, Berkowicz R, Britter R (2004) The influence of street architecture on flow and dispersion in street canyons. *Meteorol Atmos Phys* 87:121–131

- Kim JJ, Baik JJ (1999) A numerical study of thermal effects on flow and pollutant dispersion in urban street canyons. *J Appl Meteorol* 38(9):1249–1261
- Kundu PK, Cohen IM (2007) *Fluid mechanics*, 4th edn. Academic Press, Amsterdam, 904 pp
- Melling A (1997) Tracer particles and seeding for particle image velocimetry. *Meas Sci Technol* 8:1406–1416
- Nelson MA, Pardyjak ER, Klewicki JC, Pol SU, Brown MJ (2007) Properties of the wind field within the Oklahoma City Park Avenue street canyon. Part I: mean flow and turbulence statistics. *J Appl Meteorol Clim* 46:2038–2054
- Ohba M (1998) Experimental study of effects of separation distance between twin high-rise tower models on gaseous diffusion behind the downwind tower model. *J Wind Eng Ind Aerodyn* 77–78:555–566
- Oke TR (1987) *Boundary layer climates*, 2nd edn. Routledge, London, 435 pp
- Oke TR (1988) Street design and urban canopy layer climate. *Energ Build* 11(1–3):103–113
- Panofsky HA, Dutton JA (1983) *Atmospheric turbulence: models and methods for engineering applications*. Wiley, New York, 397 pp
- Rotach M (1993) Turbulence close to a rough urban surface. Part I: Reynolds stress. *Boundary-Layer Meteorol* 65:1–28
- Salizzoni P, Soulhac L, Mejean P (2009) Street canyon ventilation and atmospheric turbulence. *Atmos Environ* 43(32):5056–5067
- Santiago JL, Martin F (2005) Modelling the air flow in symmetric and asymmetric street canyons. *Int J Environ Pollut* 25(1):145–154
- Singh B, Hansen B, Brown M, Pardyjak E (2008) Evaluation of the QUIC-URB fast response urban wind model for a cubical building array and wide building street canyon. *Environ Fluid Mech* 8(4):281–312
- Sini JF (1996) Pollutant dispersion and thermal effects in urban street canyons. *Atmos Environ* 30(15):2659–2677
- Snyder WH, Lawson RE (1994) Wind-tunnel measurements of flow fields in the vicinity of buildings. In: Eight joint conference on application of air pollution meteorology with A&WMA. American Meteorological Society, Nashville, TN, pp 240–250
- Soulhac L, Mejean P, Perkins R (2001) Modelling the transport and dispersion of pollutants in street canyons. *Int J Environ Pollut* 16(1):404–416
- Tennekes H, Lumley JL (1972) *A first course in turbulence*. MIT Press, Cambridge, 300 pp
- Turner DB (1994) *Workbook of atmospheric dispersion estimates*, 2nd edn. Lewis Publishers, Boca Raton, 192 pp
- Wood C, Arnold SJ, Balogun A, Barlow JF, Belcher SE, Britter R, Cheng H, Dobre A, Lingard J, Martin D (2009) Dispersion experiments in central London. *Bull Am Meteorol Soc* 90:955–969
- Xie X, Huang Z, Song Wang J (2005) Impact of building configuration on air quality in street canyon. *Atmos Environ* 39(25):4519–4530
- Xueling C, Fei H (2005) Numerical studies on flow fields around buildings in an urban street canyon and cross-road. *Adv Atmos Sci* 22(2):290–299
- Yang R, Zhang J, Shen S, Li X, Chen J (2007) Numerical investigation of the impact of different configurations and aspect ratios on dense gas dispersion in urban street canyons. *Tsinghua Sci Technol* 12(3):345–351

CHAPTER 3

**A STUDY OF FLOW FIELDS IN
STEP-DOWN STREET
CANYONS**

Addepalli B, Pardyjak ER (2015) Investigation of the flow structure in step-up street canyons - Mean flow and turbulence statistics. *Environ Fluid Mech* 15:439 - 481. Reprinted with kind permission from Springer Science and Business Media.

A study of flow fields in step-down street canyons

Bhagirath Addepalli · Eric R. Pardyjak

Received: 16 April 2013 / Accepted: 31 May 2014
© Springer Science+Business Media Dordrecht 2014


Abstract A step-down street canyon is a street canyon in which the upwind building height (H_u) is greater than the downwind building height (H_d) ($H_u > H_d$). Here, the effect of downwind building height and canyon width on the flow structure in isolated step-down canyons is investigated through wind-tunnel measurements. The measurements were acquired along the vertical symmetry plane of the model buildings using two-dimensional particle image velocimetry for normal approach flow. For the present study, H_u was kept constant at 120 mm, and H_d was increased in increments of $\approx 0.08H_u$, to span the range: $0.08 \leq H_d/H_u \leq 1$. The configuration $H_d/H_u \approx 1$ corresponds to a deep canyon. The footprints of the buildings were square, with the widths (W) and lengths (L) being, $W(=L) \approx 32$ mm. Four different street-canyon widths (S) were considered, with $S/W \approx 2.5, 2, 1.5, 1$. This resulted in a total of 48 test cases, with 12 cases for every street-canyon width. The flow topology in the near-wake of an isolated tall building ($H_d = 0$) is characterised by a bow-shaped structure comprising the vortex core, saddle point, and ground originating shear layer. For $S/W \approx 2.5, 2$, and 1.5 , increasing the downwind building height from $H_d/H_u \approx 0.08$ to 1 resulted in the in-canyon flow structure transitioning from *wake dominated* to *deep canyon wake interference regimes*. Similar increase of the downwind building height for $S/W \approx 1$ resulted in the flow structure transitioning from *wake dominated* to *deep canyon skimming flow regime*. The results indicate that in step-down canyons formed by tall and slender buildings, momentum transport into and out of the canyon around the building sidewalls plays a crucial role in the determining the overall flow patterns in the canyon.

Keywords Flow topology · Particle image velocimetry · Urban fluid mechanics · Wind tunnel study

B. Addepalli · E. R. Pardyjak (✉)
Department of Mechanical Engineering, University of Utah, Salt Lake, UT84112, USA
e-mail: pardyjak@eng.utah.edu

B. Addepalli
e-mail: addbugs@gmail.com

Published online: 15 June 2014

 Springer

1 Introduction

The study of flow fields in modelled urban areas is motivated by a number of environmental concerns such as air quality, contaminant releases, and pedestrian comfort. A vast body of literature exists that characterises flow over simple building structures such as isolated buildings and idealized street canyons [2, 5, 6, 8–14, 16–18, 21–29, 31–39, 41, 43, 44, 46, 47, 49–51, 54, 56, 58–61, 63, 64]. Tall buildings (where tall is defined with respect to the ratio of building height and the boundary layer depth) are a prominent feature of urban downtowns. Yet, there is very little literature that describes the physics governing flow fields around tall buildings, and their interactions with other buildings. Urban flows are highly complex due to the combined effects of several parameters such as, meandering winds, diverse building geometries, complex surface energy balances, vegetative canopies, etc. acting in unison. Wind-tunnel modelling provides a way to systematically control and vary several of these effects in simplified urban configurations. In the present work, the flow structure in isolated step-down street canyons is investigated through wind-tunnel measurements. Specifically, the role of three-dimensionality in the flow is investigated by looking at the adjustment of flow structures along the center plane of the canyons for a range of 3D geometries (i.e., a large suite of S/W and H_d/H_u configurations).

A step-down street canyon is a street canyon in which the upwind building height (H_u) is greater than the downwind building height (H_d) (i.e., $H_u > H_d$). The presence of tall buildings in a cluster of relatively shorter buildings (which is typical of any real urban downtown) results in the formation of step-down canyons, depending on the ambient wind direction. Variation in the building heights in a street canyon significantly alters the in-canyon flow structure. The flow structure in the vicinity of tall buildings in general, and step-down street canyons in particular depends on a number of parameters, and has been studied through wind-tunnel experiments [1, 15, 42, 55, 57] and 2D and 3D numerical simulations [6, 7, 48, 50, 59, 62]. The parameters include the shear and turbulence in the inflow [15], building separation distance [1, 42, 48], and building alignment and geometry [1, 6, 7, 55, 57, 62]. Of the mentioned studies, the works of [15, 55] have focussed on isolated tall buildings, while [7, 42] examined the flow and dispersion patterns in deep canyons (a street canyon comprised of tall buildings, with $H_u = H_d$). Though [57] reported the flow patterns in step-down canyons, they only considered a 2D configuration. In the present work, the effect of street-canyon width and the downwind building height on the flow structure in 3D isolated step-down street canyons is investigated using 2D particle image velocimetry (PIV) measurements in a wind tunnel.

In addition to understanding flow physics in the vicinity of tall buildings, wind tunnel measurements in step-down canyons (and several other configurations [4]) were acquired to evaluate the Quick Urban and Industrial Complex dispersion model (QUIC) [20, 52, 53]. The results of model-evaluation [3] are not discussed in this paper for consiency. High spatial-resolution wind-tunnel data for isolated street-canyons can help extend the existing flow regime classifications, and can be used in the development of parameterizations for fast-response and empirical flow models, and in the validation of computational fluid dynamics (CFD) codes. The current work therefore aspires to contribute to the existing knowledge of flow in urban environments.

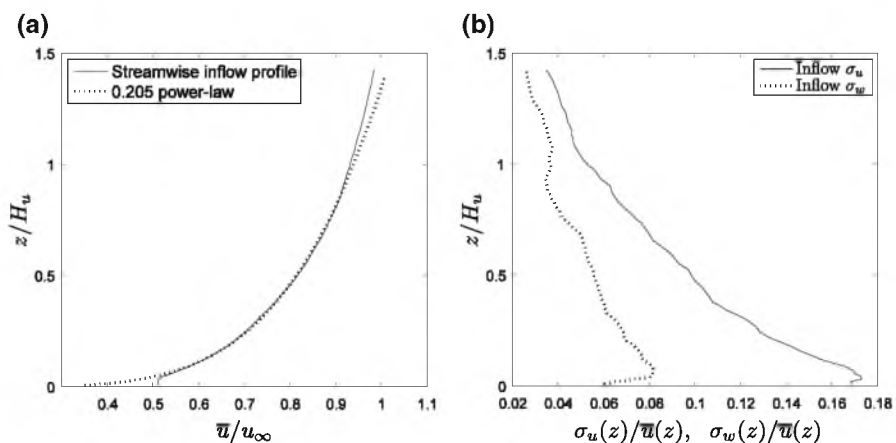


Fig. 1 Schematic showing, a the mean streamwise inflow velocity profile, b inflow streamwise and vertical velocity standard deviations

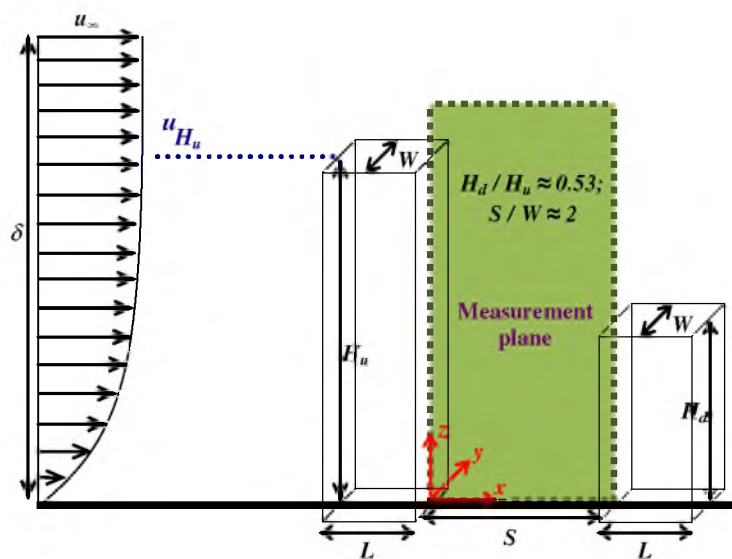


Fig. 2 Schematic showing the various terms and the coordinate system used to define a step-down canyon (figure not to scale)

2 Experimental details

The experiments were conducted at the environmental fluid dynamics (EFD) laboratory at the University of Utah, at an atmospheric pressure of 86.5 kPa of Hg, temperature of 21.5 °C, in a 7.9-m long boundary-layer wind-tunnel facility, having a working cross section of 0.61 m \times 0.91 m. For details of the experimental setup, the reader may refer to Addepalli and Pardyjak [2]. LEGO® sheets with circular dimples of height 2 mm lined the floor of the tunnel and were used to produce a uniform rough-walled turbulent flow. All of the experiments were

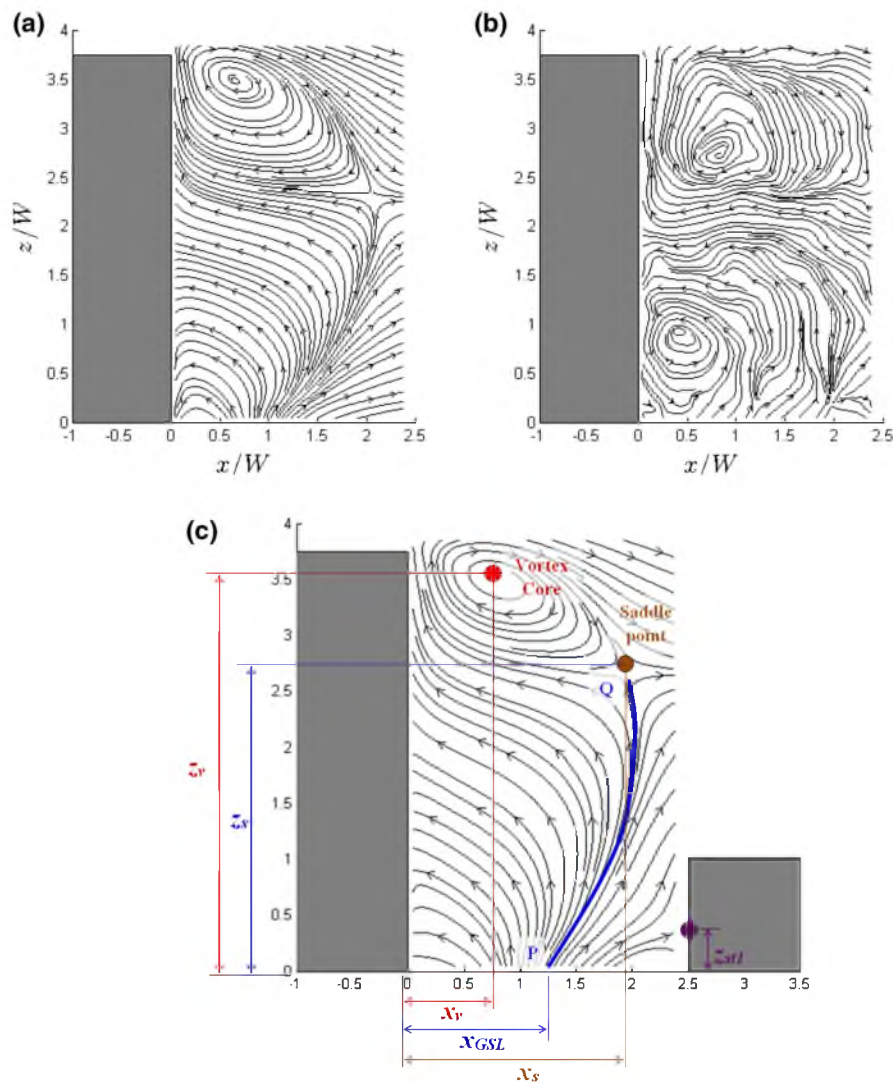


Fig. 3 Near-wake flow of an isolated tall building, **a** mean streamline patterns, **b** instantaneous streamline patterns, and **c** definitions of topological flow features from the mean flow

run at a mean streamwise freestream velocity of $u_\infty \approx 7.2 \text{ m s}^{-1}$. The corresponding mean streamwise velocity at the upwind building height (H_u) in the boundary layer (without the buildings) was $u_{H_u} \approx 6.71 \text{ m s}^{-1}$. The boundary-layer depth (δ) and power-law exponent (η) at the measurement location were $\delta \approx 240 \text{ mm}$ ($\delta/H_u \approx 2$) and $\eta \approx 0.205$. The roughness height (z_0) and the friction velocity (u_*) of the boundary layer were $z_0 \approx 0.15 \text{ mm}$ and $u_* \approx 0.26 \text{ m s}^{-1}$. The Reynolds number based on the upwind building height (Re_{H_u}) ($Re_{H_u} = u_{H_u} H_u / \nu$, $\nu = 1.5 \times 10^{-5} \text{ m}^2 \text{ s}^{-1}$) was $Re_{H_u} \approx 53,680$, and the roughness Reynolds number (Re_{z_0}) ($Re_{z_0} = u_* z_0 / \nu$) was $Re_{z_0} \approx 2.6$. Figure 1 shows the mean

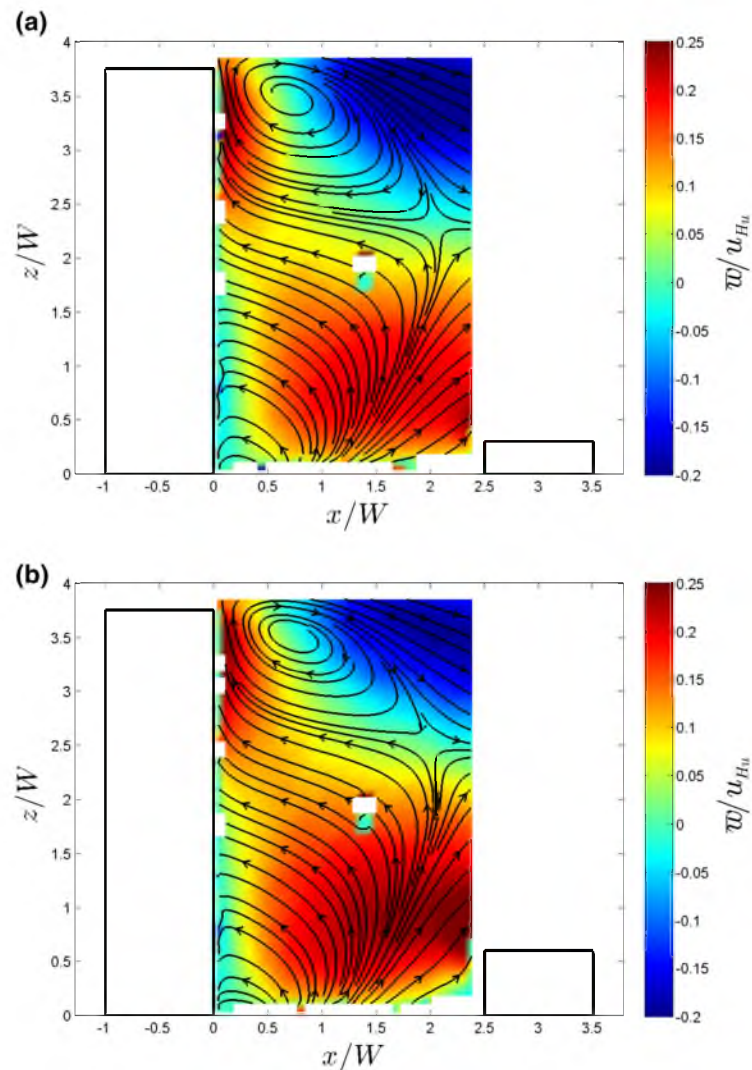


Fig. 4 Contours of the normalized mean vertical velocities (\overline{w}) in step-down canyons with $S/W \approx 2.5$ and $H_d/H_u \approx$. **a** 0.08, **b** 0.16, **c** 0.27, **d** 0.35, **e** 0.43, **f** 0.53, **g** 0.61, **h** 0.69, **i** 0.80, **j** 0.88, **k** 0.96, and **l** 1.00

streamwise inflow velocity (\overline{u}) profile and the inflow streamwise and vertical velocity standard deviations (turbulence intensities), σ_u and σ_w .

The model buildings were constructed using LEGO[®] blocks and had square footprints. The walls of the model buildings were ‘smooth’ on all sides. The plan area of the buildings was kept constant at $L \times W \approx 32 \times 32 \text{ mm}^2$, where L and W are the lengths and widths of the model buildings. In the experiments performed, the upwind building-height (H_u) was kept constant at $H_u \approx 120 \text{ mm}$. The downwind building-heights (H_d) considered were, $H_d \approx 9.6, 19.2, 32, 41.6, 51.2, 64, 73.6, 83.2, 96, 105.6, 115.2, \text{ and } 120 \text{ mm}$, resulting in H_d/H_u values of, $H_d/H_u \approx 0.08, 0.16, 0.27, 0.35, 0.43, 0.53, 0.61, 0.69, 0.80, 0.88, 0.96, \text{ and } 1.00$. This

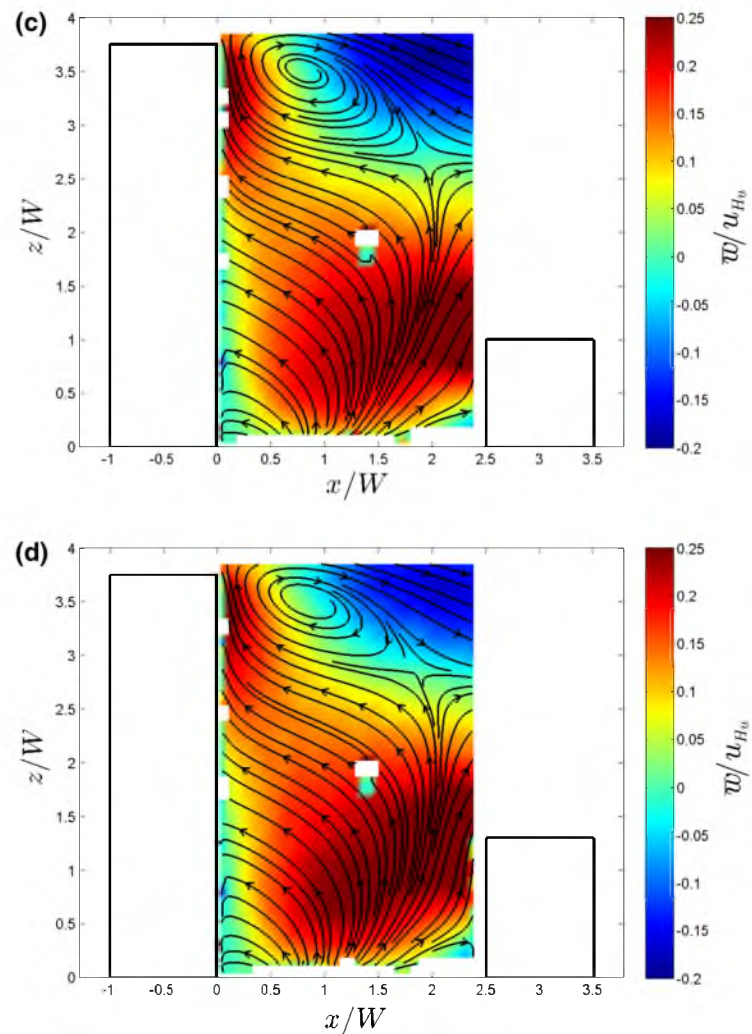


Fig. 4 continued

resulted in 12 cases (street-canyon configurations) for a given street-canyon width (S). Four different street canyon widths (S) were considered, with $S/W \approx 2.5, 2, 1.5, 1$. This resulted in a total of 48 cases for all the experiments. Definitions of critical dimensions and the region in the vertical symmetry plane where the measurements were acquired are shown in Fig. 2.

Based on the value of $\delta/H_u \approx 2$, the configurations considered in the current work correspond to tall building urban-street canyons. The blockage effects due to the presence of the buildings in the wind tunnel were characterised through velocity measurements using pitot-static probes, and were not found to be significant. The pressure gradient induced along the tunnel centreline in the measurement section due to the presence of the buildings was $\approx 2.5 \text{ Pa m}^{-1}$. The relative increase in the tunnel centreline velocity due to the presence of the buildings was $\approx 2.5\%$.

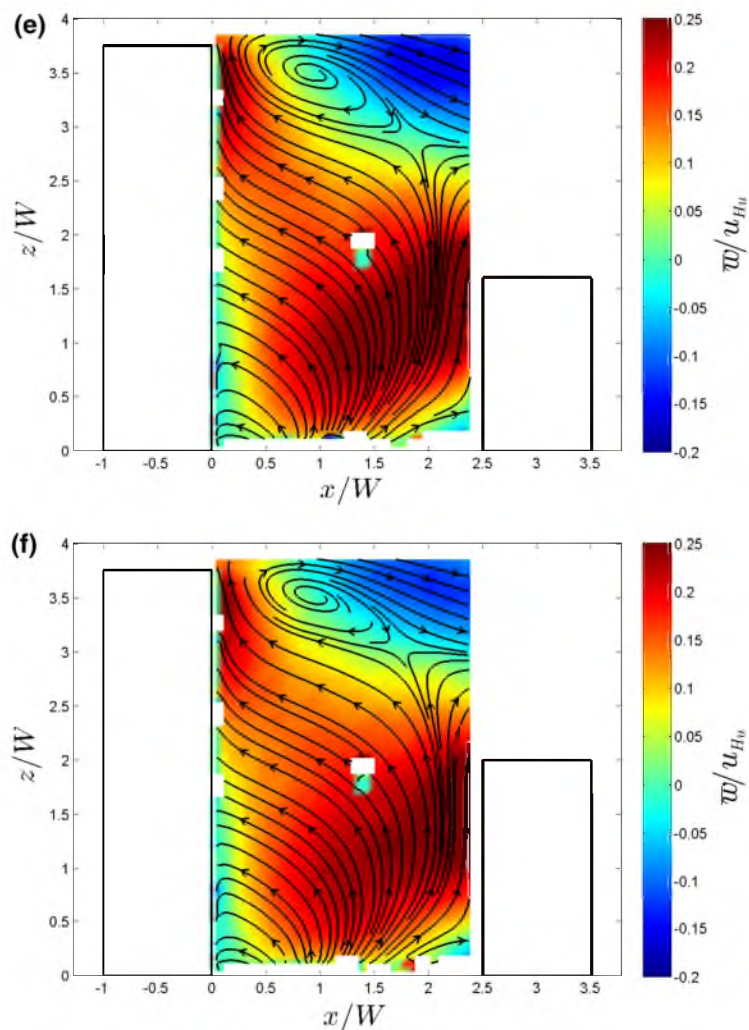


Fig. 4 continued

In the experiments conducted, 2D PIV was used as the measurement technique. The measurements were taken along the vertical symmetry plane (x - z plane) of the model buildings (shown in Fig. 2). The flow was seeded with olive oil particles having a mean diameter of approximately $0.45\ \mu\text{m}$, generated using two Laskin nozzles. According to Melling [40] these particles should be approximately non-inertial and non-buoyant. The aerosols were illuminated with a 532-nm wavelength laser sheet (1.5 mm thick), generated using a 50 mJ NewWave Research (Fremont, CA) Solo PIV III Nd-Yag laser. A 4.0MP (2048×2048 pixels) CCD camera manufactured by TSI, Inc. (Shoreview, MN) with a maximum frame rate of 17 frames per second (fps) was used in conjunction with a frame grabber for image acquisition. The image acquisition rate was set to 2 fps. A LASERPULSE synchronizer was used to control the timing between the laser pulses and the camera shutter open time through a PC

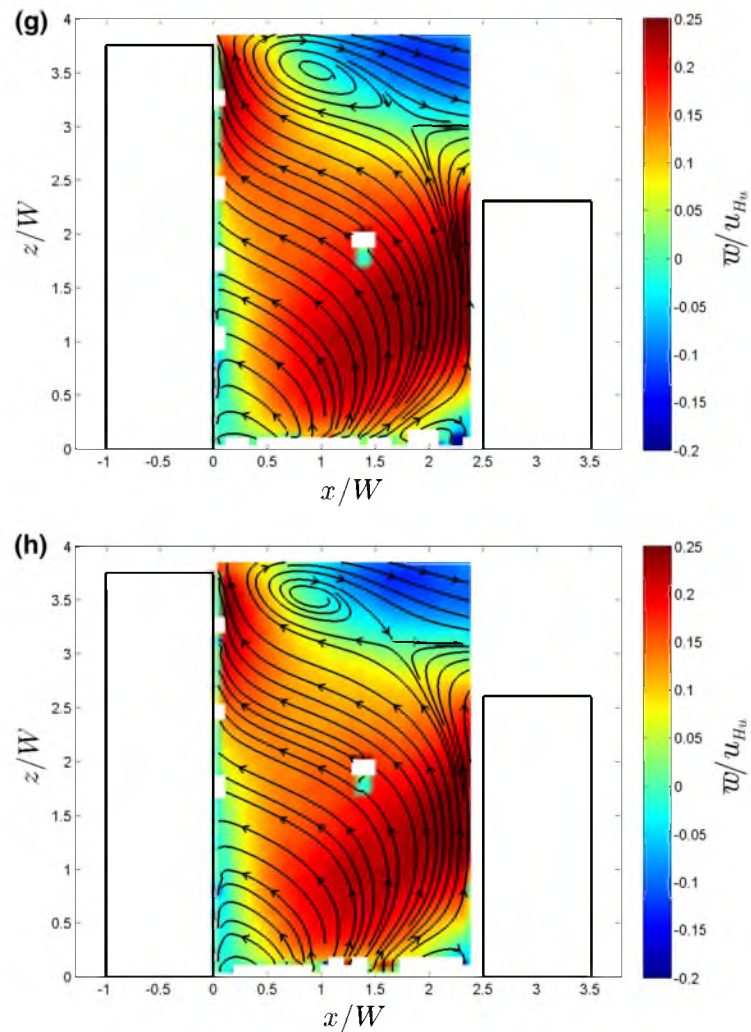


Fig. 4 continued

desktop computer. Analysis of the acquired image pairs was done using TSI INSIGHT3G analysis software. Fast Fourier transform (FFT) based cross-correlation analysis was performed on the conditioned image pairs by dividing them into 64×64 pixel interrogation regions. One thousand image pairs were considered for computing the average velocity and turbulence fields. The spatial resolution of the final datasets obtained was ≈ 2.35 mm.

3 The near-wake of an isolated tall building

An isolated tall building configuration may be viewed as a special case of a step-down street-canyon configuration with $H_d = 0$. Understanding the near-wake flow of an iso-

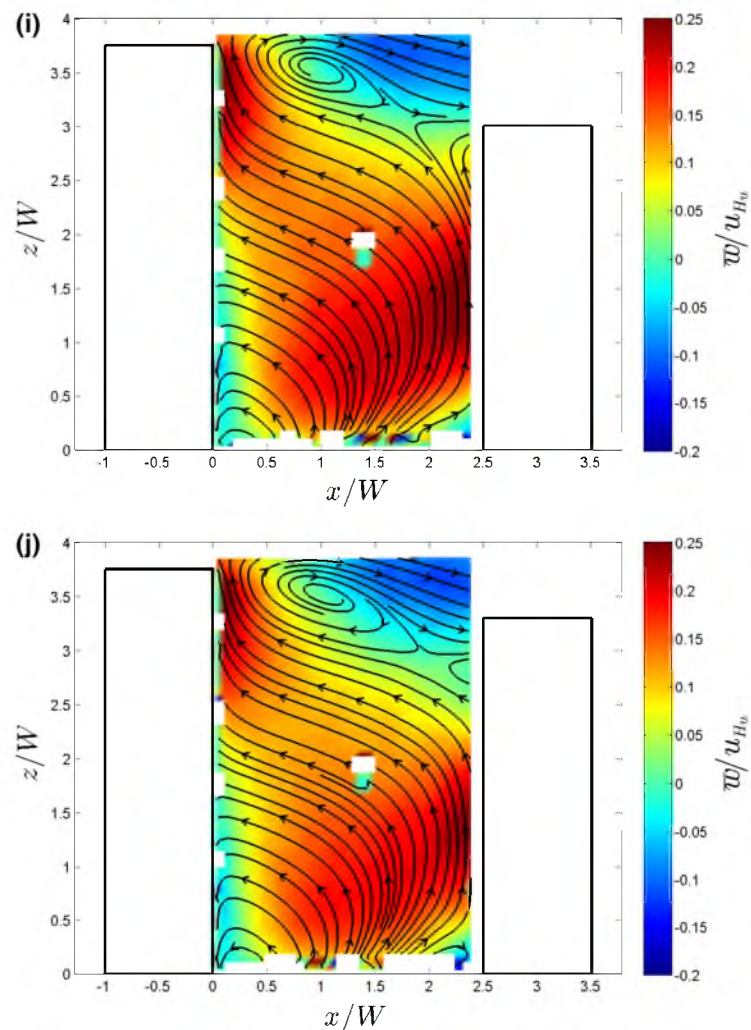


Fig. 4 continued

lated tall building is crucial to understanding step-down street-canyon flows. Figure 3a depicts the mean streamline patterns in the near-wake of an isolated tall building with height $H \approx 120\text{mm}$, and square plan area ($L \times W \approx 32 \times 32\text{mm}^2$). The inflow velocity field characteristics for this configuration were the same as those described in the previous section. Figure 3c identifies the prominent flow features in the near-wake of a tall building (step-down canyon with $H_d/H_u \approx 0.27$, $S/W \approx 2.5$). The prominent flow features are, a primary vortex near the building (upwind building) leeward face below the rooftop [with spatial coordinates of the vortex core being (x_v, z_v)], a saddle point at the interface of the near and far-wakes [with coordinates (x_s, z_s)], a (ground originating) shear layer PQ (which can also be viewed as a *cavity dividing streamline*) apparently emanating from the surface with x -coordinate x_{GSL} ($x_{GSL}/W \approx$

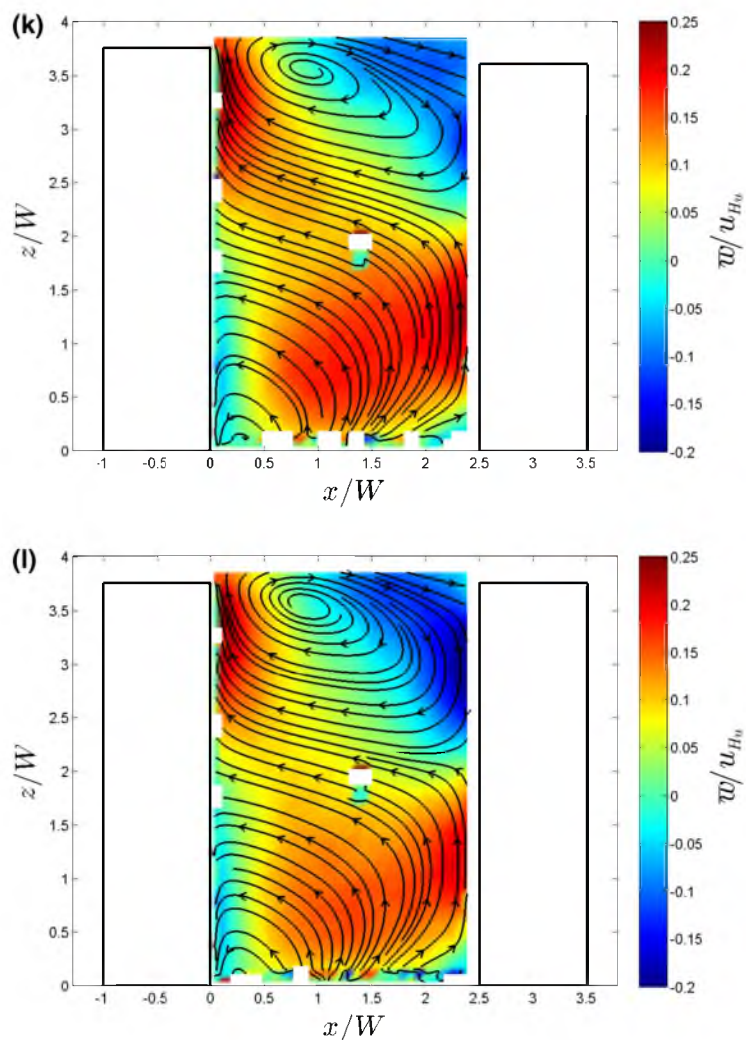


Fig. 4 continued

1.0 for the isolated tall building), a counter-rotating vortex below the primary vortex, and a stagnation point on the downwind building windward face with z -coordinate z_{st1} .

Davies et al. [15] first demonstrated the presence of a saddle point in the near-wake of a tall building with $H/W = 6$. They called it an *elevated free stagnation point*. Snyder and Lawson [55] suggested that the saddle point appeared when the height of a square footprint building was increased from $H = W$ to $H = 2W$. Ohba [42] also detected a saddle point in the wake of a tall square footprint building with $H/W = 3$. Understanding the formation of the saddle is pivotal to understanding the physics that govern the wake flow. For flows over tall buildings, the saddle point can be understood to be a result of the increased flow around the sides of the building compared to that over the rooftop. For flows over isolated

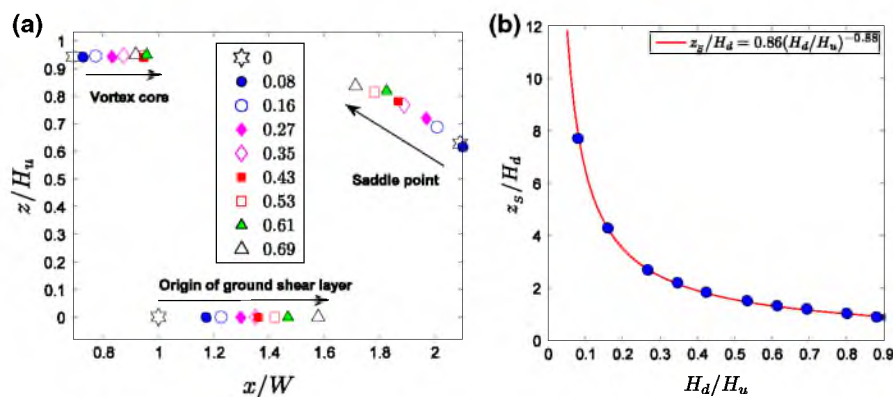


Fig. 5 For the different H_d/H_u values: a changes in the x and z locations (coordinates) of the vortex core, saddle point, and the ground originating shear layer origin and b change in the elevation (z_s) of the saddle point. These estimates are for the $S/W = 2.5$ cases

buildings, a low pressure region is created near the building leeward face. The flow over the rooftop and sidewalls moves towards the low pressure region. The ground originating shear layer is therefore indicative of the extent to which the flow over the sides penetrates into the wake before moving toward the low pressure region. The saddle point represents the point at which the sidewall and the rooftop motions come to equilibrium. Thus, above the saddle point, a primary vortex rotating in the clockwise direction is seen, and below it, a secondary counter-rotating vortex. The secondary vortex is highly unsteady and is not apparent in the averaged flow field. Examining an instantaneous snapshot (Fig. 3b) of the flow illustrates the unsteady nature of the secondary vortex.

4 Results and discussion

4.1 Step-down street canyons with $S \approx 2.5W$

In Fig. 4 contours of the normalized mean vertical velocities (\overline{w}/u_{H_u}), and the mean streamline patterns in step-down canyons with $S \approx 2.5W$ are shown. Some of the *white spots* seen in the figure are due to loss of data as a result of reflection issues caused by the laser sheet, and burnt pixels in the CCD camera used for image acquisition.

Figure 4 shows the effect of adding a downwind building of different heights to the wake of a tall building. The addition of a relatively short downwind building only slightly modifies the mean flow field such that it is still dominated by the upwind building's wake. A close inspection of the mean streamline patterns suggests that as the downwind building height (H_d) is increased from $0.08H_u$ to H_u , the flow transitions from a *wake dominated regime* to a *deep canyon wake interference regime*. The *deep canyon wake interference regime* can be regarded as the *wake interference regime* [28] for tall buildings. The transition between the regimes is found to occur in the interval $0.88 < H_d/H_u \leq 1$ for $S \approx 2.5W$, and is characterised by the conversion of the saddle point in the upwind building wake to a stagnation point on the downwind building windward face.

As much as the flow structure for $H_d/H_u \approx 1$, $S = 2.5W$ resembles the *skimming flow regime* [28] for tall buildings (characterised by a counter-rotating vortex pair), we refrain from

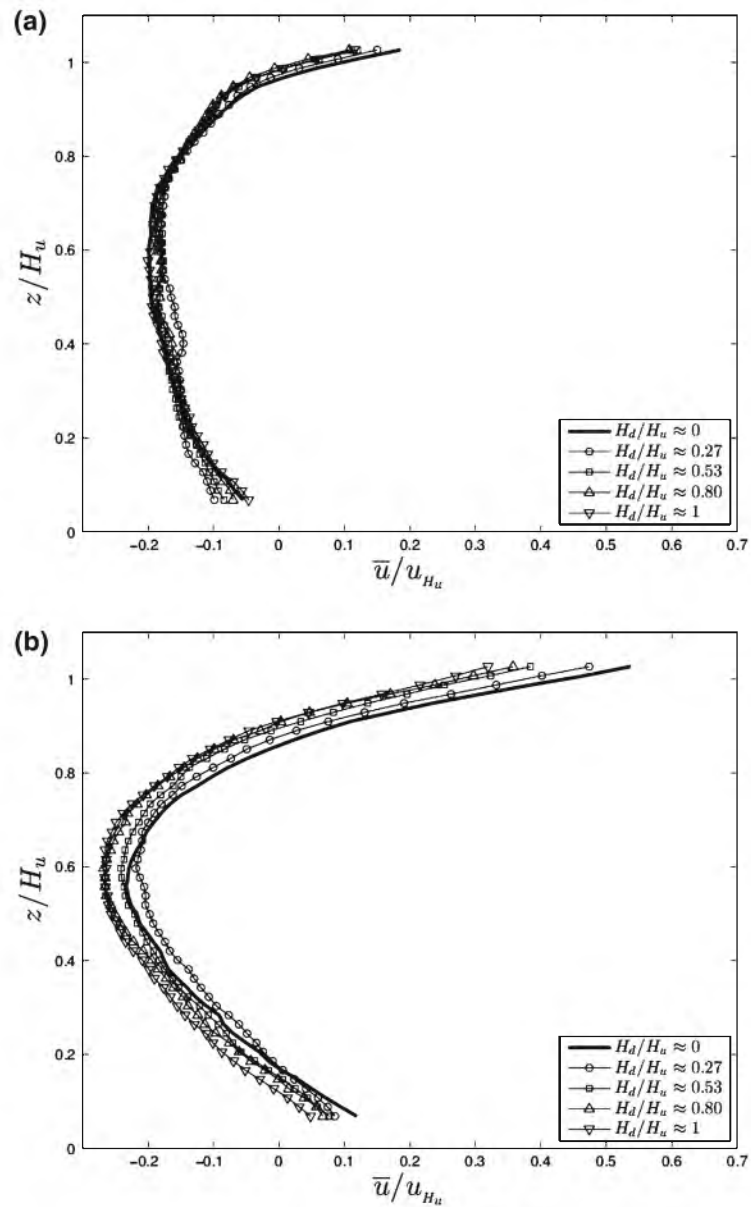


Fig. 6 Normalized vertical profiles of mean streamwise velocity (\bar{u}/u_{Hu}) for $S/W \approx 2.5$ and $H_d/H_u \approx 0, 0.27, 0.53, 0.80, 1$ at, **a** $x/S \approx 0.1 (\Rightarrow x/W \approx 0.25)$, **b** $x/S \approx 0.5 (\Rightarrow x/W \approx 1.25)$, **c** $x/S \approx 0.9 (\Rightarrow x/W \approx 2.25)$

associating it with the *deep canyon skimming flow regime* due to the presence of the ground originating shear layer in the in-canyon region. As was discussed in the previous section, the ground originating shear layer is indicative of the extent to which the flow over the sides of the upwind building penetrates into its wake. The presence of the ground originating shear

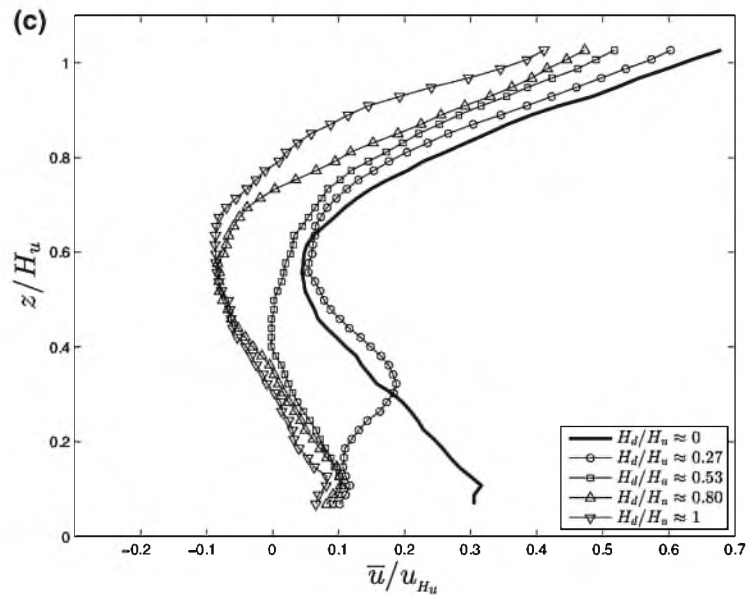


Fig. 6 continued

layer for $S \approx 2.5W$ therefore suggests that the flow structure for these cases may be labeled as the *deep canyon wake interference regime*. Though not referred to as belonging to the *deep canyon wake interference* and *deep canyon skimming flow regimes*, such flow structures have been previously reported by [7,42].

The works of [62] and [48] described the flow patterns in 2D step-down canyons with $H_d/H_u \approx 0.67$, $S = H_d$, $L = H_d$, and $H_d/H_u \approx 0.67$, $S = H_d$, $L = 0.5H_d$. It should however be noted that the configurations studied by [62] and [48] were not isolated step-down canyons, but arrangements of buildings that resulted in step-down, step-up, and square canyons. Overlooking the scaling of the building lengths and the slight differences in the scaling of the other characteristic (physical) dimensions, the configuration $H_d/H_u \approx 0.69$, $S \approx 2.5W$ from the present work may be compared to that considered by [48] and [62]. Comparing the flow structures obtained from the 3D experimental and 2D numerical experiments, it is seen that the shape and extent of the primary and secondary vortices, and the location of the saddle point differ. In the results of [62], the primary vortex extends until the downwind building trailing edge, with the vortex core at the downwind building leading edge, and the saddle point at the trailing edge. Also, a more coherent and symmetric secondary vortex is seen in the region below the downwind building roof height. The velocity vectors reported by [48] are very similar to the flow structure reported by [62]. The differences in the results illustrate the importance of accounting for momentum transport into the canyon in the lateral direction. The differences may be speculated to be due to the greater interaction between the rooftop and sidewall flows (over and around the upwind building) in the vertical symmetry plane, and the ventilation of the in-canyon flow in the lateral direction (x - y plane) around the downwind building, that the 2D simulations do not capture.

Figure 5 shows how the various flow structures in the wake of a tall building adapt to the addition of a downwind building. Among other flow features, the mean flow field

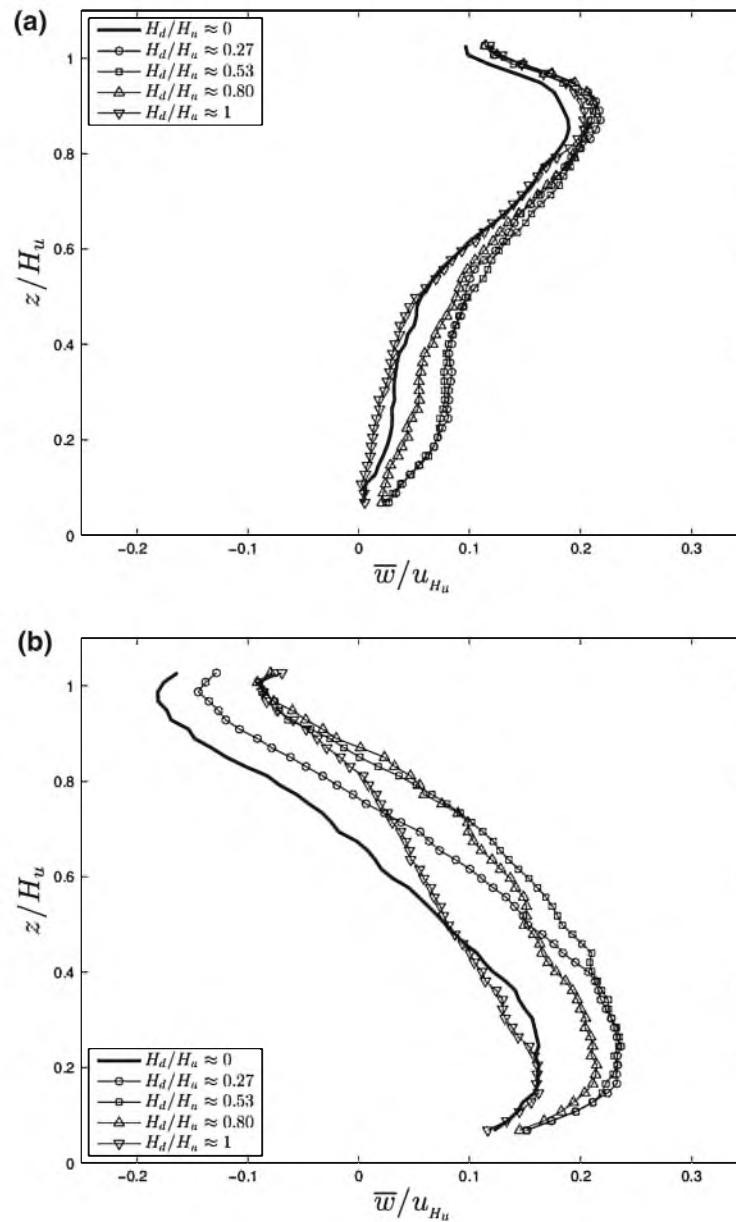


Fig. 7 Normalized vertical profiles of mean vertical velocity (\bar{w}/u_{H_u}) for $S/W \approx 2.5$ and $H_d/H_u \approx 0, 0.27, 0.53, 0.80, 1$ at, **a** $x/S \approx 0.1$ ($\Rightarrow x/W \approx 0.25$), **b** $x/S \approx 0.5$ ($\Rightarrow x/W \approx 1.25$), **c** $x/S \approx 0.9$ ($\Rightarrow x/W \approx 2.25$)

in the near-wake of a tall building is characterised by a vortex core (of the primary vortex), a saddle point, and the ground originating shear layer (as shown in Fig. 3c). The changes in the x and z -coordinates of these entities (as determined by visual inspec-

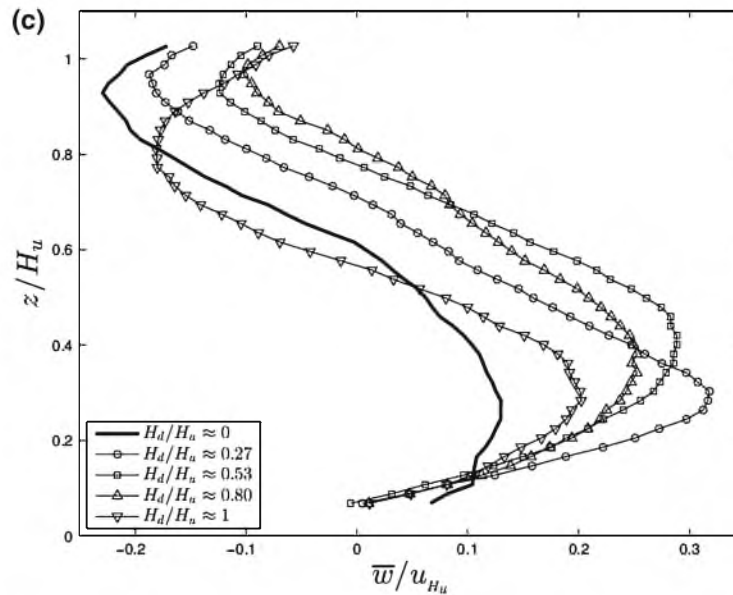


Fig. 7 continued

tion of the streamline topology) are plotted for varying downwind building heights in Fig. 5. As can be seen from Fig. 4, the near-wake of the upwind building adapts to the addition of a downwind building, while preserving the basic *bow-shaped* structure until $H_d/H_u \leq 0.69$. Beyond this ratio, the ground originating shear layer merges into the downwind building. Figure 5 shows that the vortex core and the ground originating shear layer move towards the downwind building with increasing downwind building heights. From Fig. 4, no substantial change in the stagnation point (in the lower-leg of the canyon) height on the downwind building is observed for increasing H_d values. Above the stagnation point, the flow in the vertical direction is parallel to the downwind building windward face.

Figure 5 shows how the various flow structures in the wake of a tall building adapt to the addition of a downwind building for the $S/W = 2.5$ cases. It is seen that the saddle point adjusts to the pressure field created by the downwind building. For $H_d/H_u \approx 0.80$ and $H_d/H_u \approx 0.88$ (Fig. 4i, j), it appears that the vortex core, the saddle point, and a second stagnation point (near the downwind building rooftop leading edge) exist simultaneously. Also shown in Fig. 5 is the non-dimensionalized saddle point height (z_s/H_d) for the various H_d/H_u values. From the figure it can be inferred that the non-dimensionalized saddle point height decreases as a power-law with increasing H_d/H_u values. A fit of the data suggests the non-dimensionalized saddle point height behaves like $z_s/H_d = a(H_d/H_u)^b$, where $a \approx 0.86$ and $b \approx -0.88$, with an R^2 value of 0.998.

In Figs. 6, 7, 8, 9 and 10, normalized vertical profiles of mean streamwise (\bar{u}) and vertical (\bar{w}) velocities, mean Reynolds shear stress ($\overline{u'w'}$), mean streamwise velocity gradient ($\partial\bar{u}/\partial z$), and mean turbulent kinetic energy ($TKE = [(\overline{u'})^2 + \overline{(w')^2}]/2$) for $H_d/H_u \approx 0, 0.27, 0.53, 0.80$, and 1 are shown. The profiles have been plotted at $x/S \approx 0.1 (\Rightarrow x/W \approx 0.25)$, $x/S \approx 0.5 (\Rightarrow x/W \approx 1.25)$, and $x/S \approx 0.9 (\Rightarrow x/W \approx 2.25)$ in the canyon.

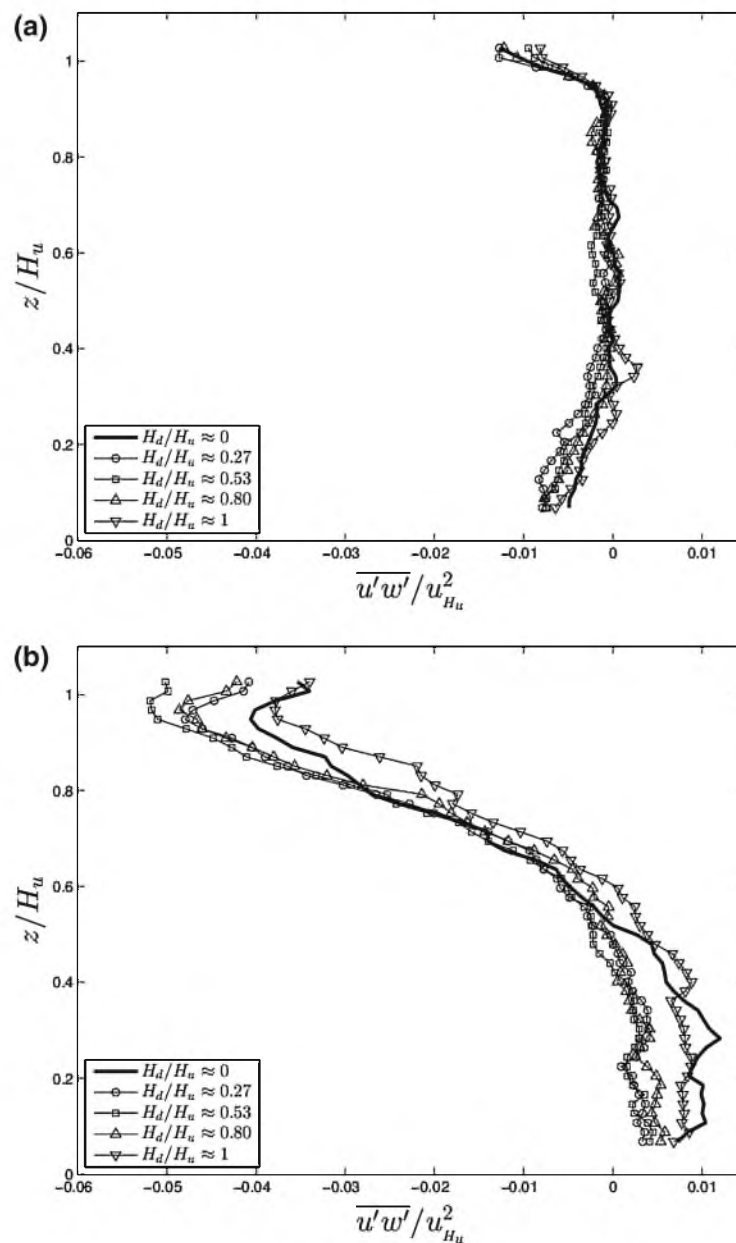


Fig. 8 Normalized vertical profiles of mean Reynolds shear stress ($\overline{u'w'}/u_{Hu}^2$) for $S/W \approx 2.5$ and $H_d/H_u \approx 0, 0.27, 0.53, 0.80, 1$ at, **a** $x/S \approx 0.1$ ($\Rightarrow x/W \approx 0.25$), **b** $x/S \approx 0.5$ ($\Rightarrow x/W \approx 1.25$), **c** $x/S \approx 0.9$ ($\Rightarrow x/W \approx 2.25$)

Figures 6b and 7b show profiles of \bar{u} and \bar{w} at the canyon centre. The shape of the streamwise velocity profile in Fig. 6b indicates the existence of the primary vortex between $0.65 \leq z/H_u \leq 1$. Specifically, the velocity is maximum in the positive streamwise direction

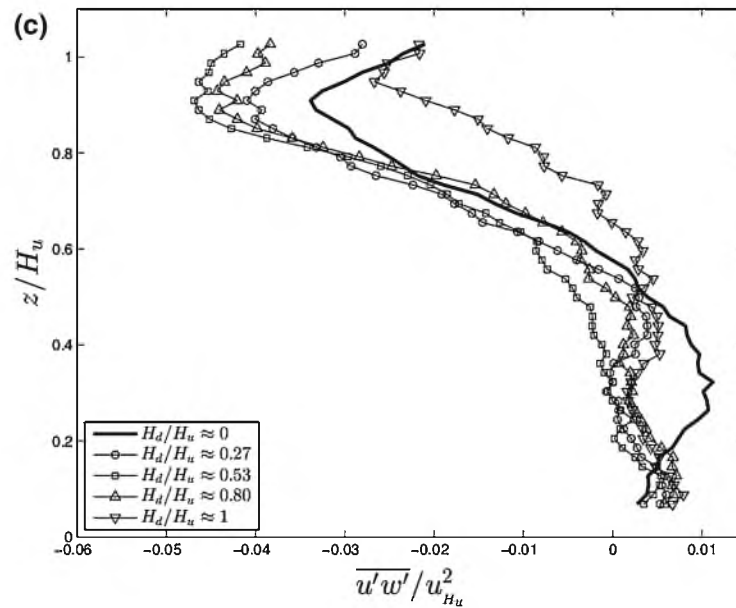


Fig. 8 continued

at $z/H_u \approx 1$, decreases through zero and then reaches a minimum negative streamwise velocity at $z/H_u \approx 0.6$. $z/H_u \approx 0.65$ is also the approximate height at which the saddle point was detected for these cases. The minimum velocity at $z/H_u \approx 0.6$ is due to enhanced momentum transport in the streamwise (negative x) direction due to interaction between the primary and secondary vortices. The region between $0 \leq z/H_u \leq 0.6$ is the region containing the secondary vortex, and is characterised by a change in the sign of \bar{u} . From Fig. 7b, it is observed that the addition of a downwind building (such that the in-canyon flow is in the *wake dominated regime*) results in weaker vertical velocities in the top-half of the canyon and stronger vertical velocities in the bottom-half, in comparison to the isolated tall building case.

Through 2D numerical simulation results, it has been suggested that in deep canyons, the streamwise and vertical velocities are significantly larger in the top-half of the canyon in comparison to the bottom-half [7]. The argument given to justify this observation is that in deep canyons, momentum transfer from the ambient wind to the top-half of the canyon is much greater than the transfer from the top-half to the bottom-half. From Figs. 6b and 7b it can be seen that the magnitudes of \bar{u} and \bar{w} are about the same in the top and the bottom halves of the canyon. In fact, the magnitude of \bar{w} is greater in the bottom-half of the canyon than the top-half. Thus, it is seen that for accurate prediction of tall building street-canyon flows, the need for accounting for momentum transport in the x - y plane cannot be overemphasized.

In Figs. 6a and 7a, profiles of \bar{u} and \bar{w} close to the upwind building leeward face are shown. From the figure it can be deduced that a change in the flow regime (from *wake dominated* to *deep canyon wake interference*) does not significantly affect the values of \bar{u} and \bar{w} in this region. In Figs. 6c and 7c, profiles of \bar{u} and \bar{w} close to the downwind building windward face are shown. From the figure it is seen that the addition of a downwind building significantly

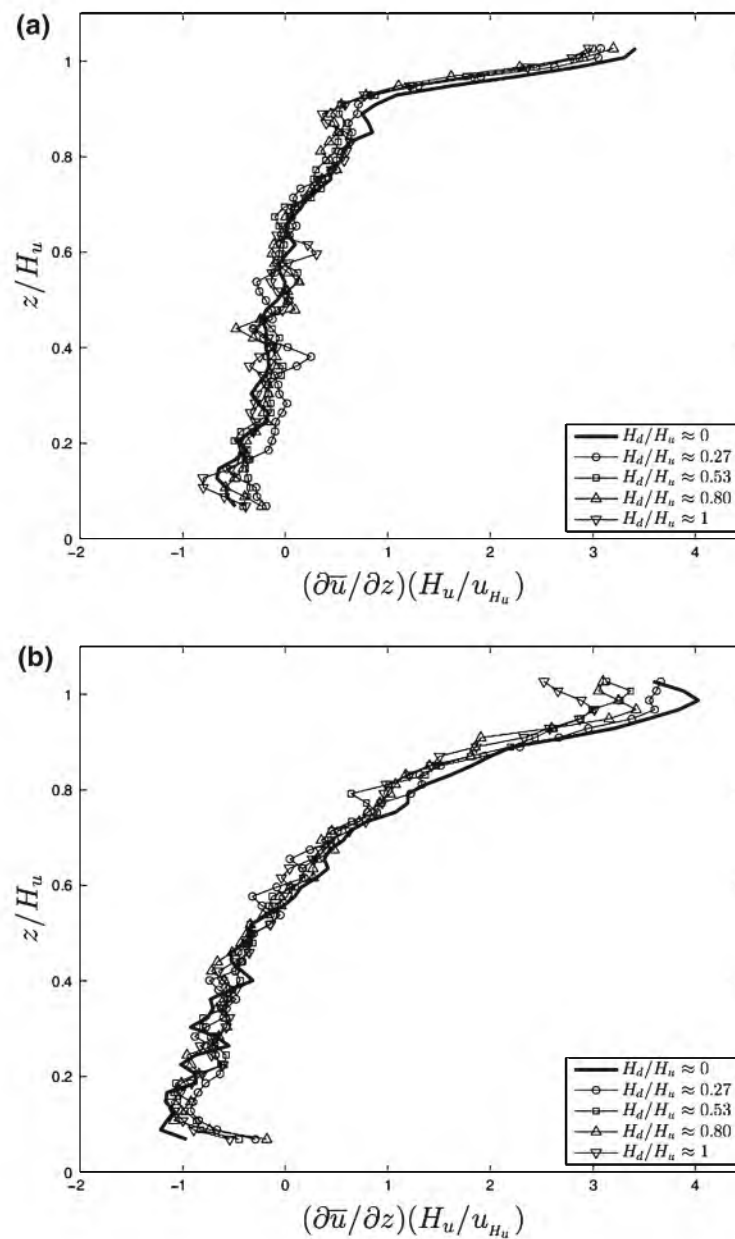


Fig. 9 Normalized vertical profiles of the mean streamwise velocity gradient $((\partial\bar{u}/\partial z)(H_u/u_{H_u}))$ for $S/W \approx 2.5$ and $H_d/H_u \approx 0, 0.27, 0.53, 0.80, 1$ at, **a** $x/S \approx 0.1 (\Rightarrow x/W \approx 0.25)$, **b** $x/S \approx 0.5 (\Rightarrow x/W \approx 1.25)$, **c** $x/S \approx 0.9 (\Rightarrow x/W \approx 2.25)$

affects the mean streamwise and vertical velocity fields in this region. For $H_d/H_u \approx 0.27$, the profiles of \bar{u} and \bar{w} for $0 \leq z/H_u \approx 0.3$ are indicative of flow separation at the downwind building leading edge. For $H_d/H_u \approx 1$ (which corresponds to the *deep-canyon*

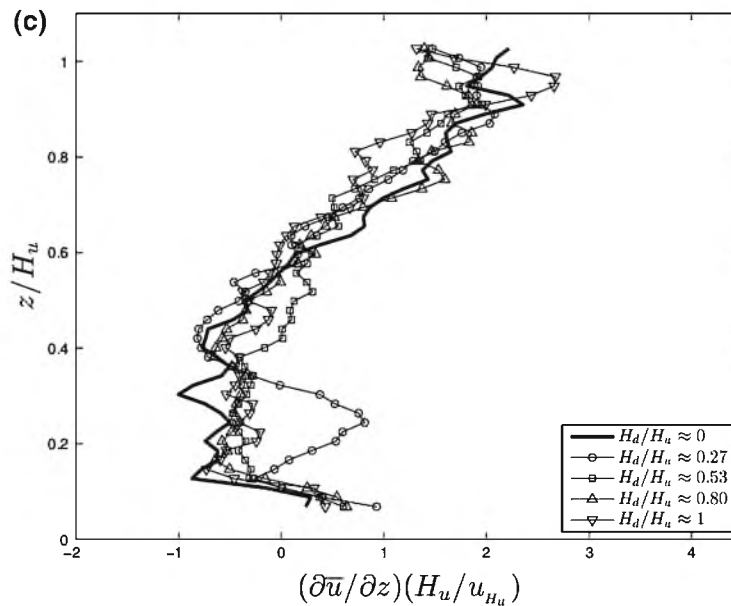


Fig. 9 continued

wake interference regime), from Fig. 7a, c it is seen that the magnitudes of the updrafts in the top-half of the canyon are slightly stronger than the downdrafts. This feature is in contrast with the field observations made by [16] for the classical *skimming flow regime* (albeit in more 2D canyons).

Figure 8a–c shows profiles of the mean Reynolds shear stress $\overline{u'w'}$. In Fig. 8b, c, as expected, peak values of $\overline{u'w'}$ occur near the top of the canyon (the upwind building roof height), and decrease to very small values in the lower-half of the canyon. Positive values of $\overline{u'w'}$ are found in the lower-half of the canyon. Positive, and relatively small values of Reynolds shear stresses in street canyons were previously reported by [45] through field experiments, by [32] through wind-tunnel studies, and by [19,30] through numerical simulations. The positive Reynolds shear stresses observed are a result of the recirculating flow in the in-canyon region. Due to this, $\partial\overline{u}/\partial z$ and $\partial\overline{w}/\partial z$ are not always strictly positive, as in the case of a boundary-layer. The form of the profiles in the lower region is unusual considering the fact that these profiles lie in the region of a secondary vortex. This behaviour can be hypothesized to be due to the momentum transfer from the lower-leg of the street-canyon due to strong updrafts. To further investigate this flow feature, profiles of the vertical gradients of the mean streamwise velocity ($\partial\overline{u}/\partial z$) are plotted at these locations (Fig. 9). From Fig. 9 it is evident that the changes in the sign and magnitude of $\overline{u'w'}$ track the changes in the sign of and magnitude of $-\partial\overline{u}/\partial z$.

Figure 10a–c shows profiles of mean turbulent kinetic energy (TKE). Large values of TKE occur in the shear layer at the top of the canyon. This is due to the strong vertical shear of the streamwise velocity in this region (profiles of $\partial\overline{u}/\partial z$ also reach their maximum in this region). At $x/S \approx 0.5$ (Fig. 10b), the profile of TKE reaches a local minimum at location where $\partial\overline{u}/\partial z$ goes to zero. Below this point, TKE begins to increase, reach-

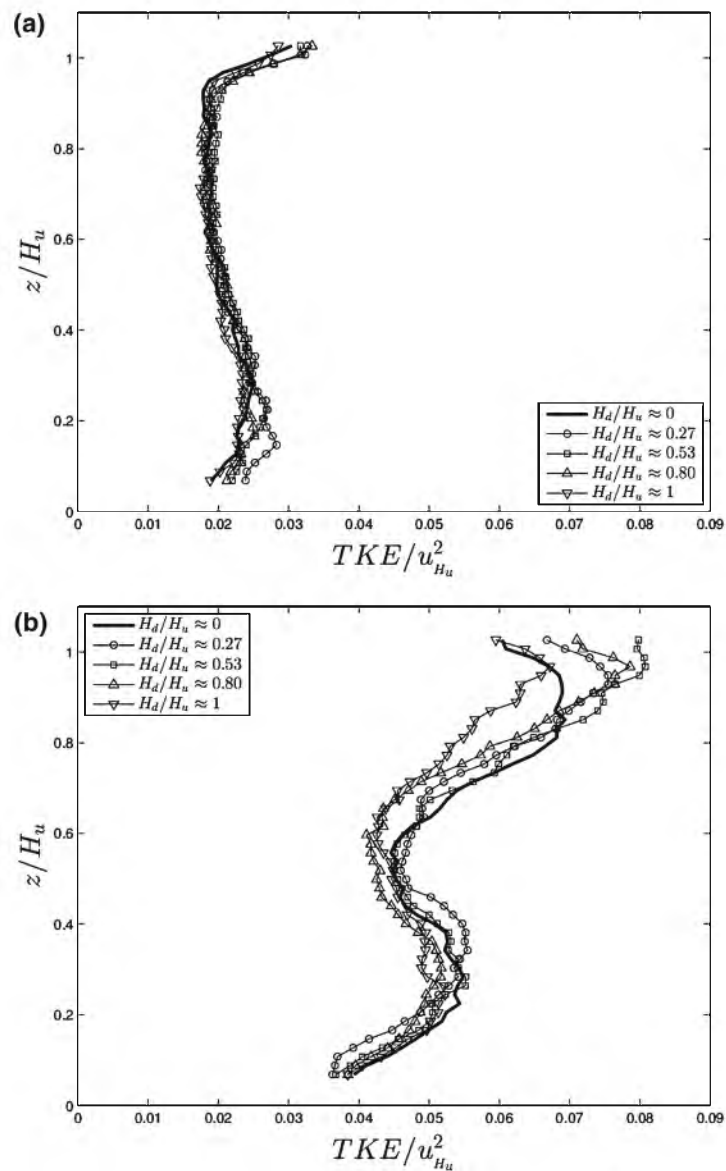


Fig. 10 Normalized vertical profiles of mean turbulent kinetic energy (TKE/u_{Hu}^2) for $S/W \approx 2.5$ and $H_d/H_u \approx 0, 0.27, 0.53, 0.80, 1$ at, **a** $x/S \approx 0.1$ ($\Rightarrow x/W \approx 0.25$), **b** $x/S \approx 0.5$ ($\Rightarrow x/W \approx 1.25$), **c** $x/S \approx 0.9$ ($\Rightarrow x/W \approx 2.25$)

ing a local maximum at $z/H_u \approx 0.3$. The second peak in the TKE profiles is associated with strong mean shear (horizontal shear of the vertical velocity) in the lower 40% of the canyon.

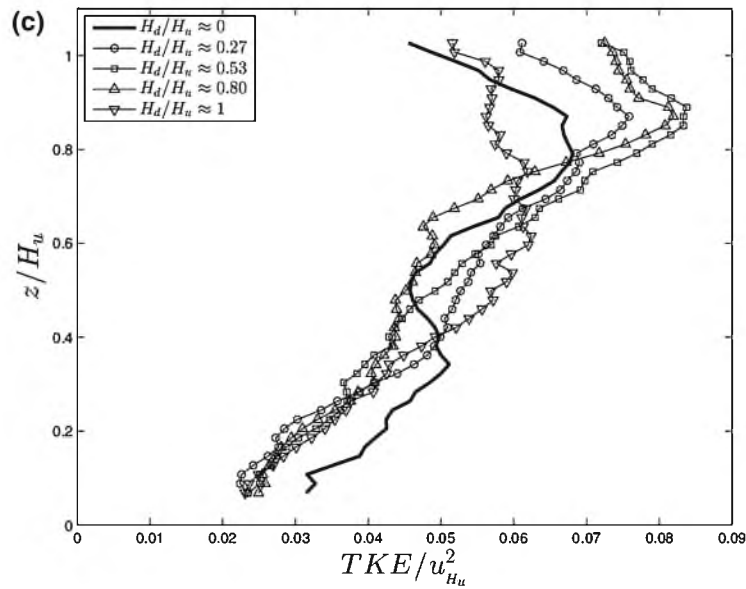


Fig. 10 continued

4.2 Step-down street canyons with $S \approx 2W$

In Fig. 11, contours of the mean vertical velocities (\overline{w}/u_{H_u}) and the mean streamline patterns in step-down canyons with $S \approx 2W$ are shown. From the figure it is seen that the change in the flow regime, from *wake dominated* to *deep canyon wake interference regime* occurs in the interval (0.69, 0.80), which is earlier in comparison to $S \approx 2.5W$ (where it occurs in the interval (0.88, 0.96)). Thus, it is seen that the effect of adding a downwind building in the upwind building's wake on the flow regime transition is enhanced as the street canyon width (S) is reduced. For $H_d/H_u \approx 1$, as was the case for $S \approx 2.5W$, the cavity dividing streamline is seen in the lower-half of the canyon for $S \approx 2W$. Due to this, the flow regime for $H_d/H_u \approx 1$ and $S \approx 2W$ is again referred to as *deep canyon wake interference regime*. Since the flow patterns for this configuration are very similar to $S \approx 2.5W$, they are not discussed for conciseness.

4.3 Step-down street canyons with $S \approx 1.5W$

In Fig. 12, contours of the mean vertical velocities (\overline{w}/u_{H_u}) and the mean streamline patterns in step-down canyons with $S \approx 1.5W$ are shown. From the figure it is seen that for this configuration, the flow field may be classified into three regimes depending on the H_d/H_u value. The flow is seen to transition from a *wake dominated* to an *intermediate regime* in the interval (0.35, 0.43), before eventually transitioning to the *deep canyon wake interference regime*. The transition from *wake dominated* to the *intermediate regime* is characterized by the disappearance of the saddle point, and the interaction of the primary vortex with the downwind building rooftop. Thus, it can be seen that among other factors, the existence of a saddle point in step-down canyons depends on the values of both H_d/H_u and S .

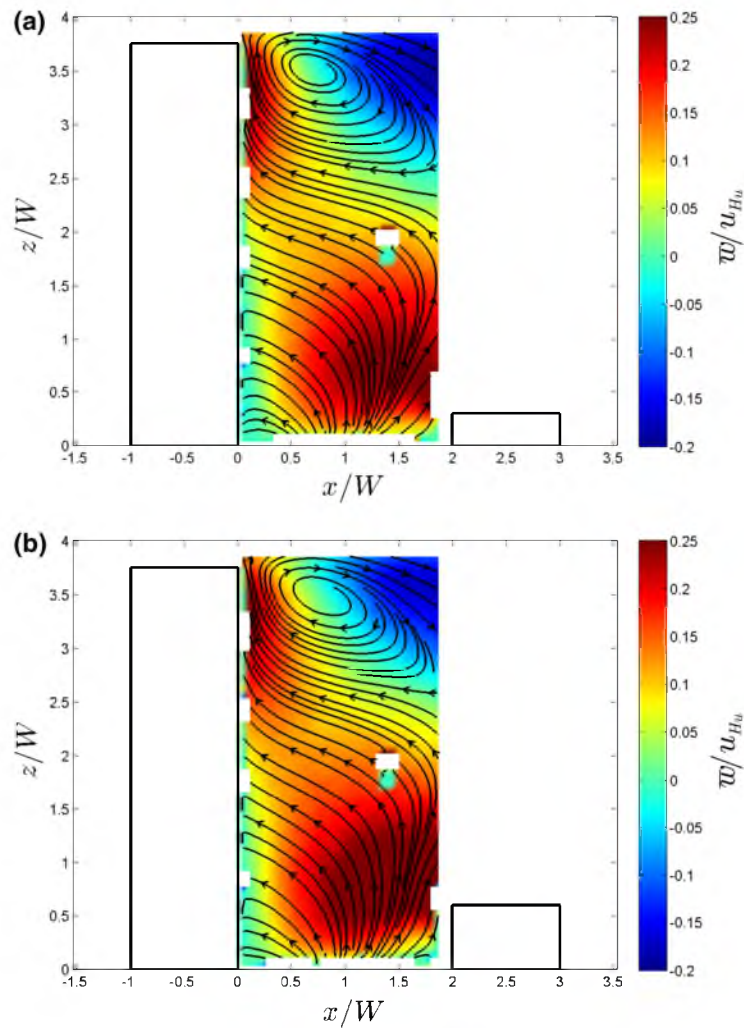


Fig. 11 Contours of the normalized mean vertical velocities (\bar{w}/u_{H_u}) in step-down canyons with $S/W \approx 2$ and $H_d/H_u \approx$, **a** 0.08, **b** 0.16, **c** 0.27, **d** 0.35, **e** 0.43, **f** 0.53, **g** 0.61, **h** 0.69, **i** 0.80, **j** 0.88, **k** 0.96, and **l** 1.00

For $S \approx 1.5W$, since the ground originating shear layer (cavity dividing streamline) for an isolated tall building is at $x_{GSL} \approx W$, addition of a downwind building with height H_d/H_u in the interval $(0, 0.43)$ modifies the wake structure of the taller upwind building, with the in-canyon flow patterns still largely driven by the taller upwind building. The saddle point heights are however lower in comparison to those observed for $S \approx 2.5W, 2W$. For higher downwind building heights ($H_d/H_u \in (0.43, 1)$), the saddle point ceases to exist and the primary vortex in the upwind building wake (near the rooftop) extends over the rooftop of the downwind building.

As was seen for $S \approx 2.5W$, differences in mean flow patterns are observed comparing the results for $S \approx 1.5W$ with those reported in [62] and [48]. The geometrical features (shape

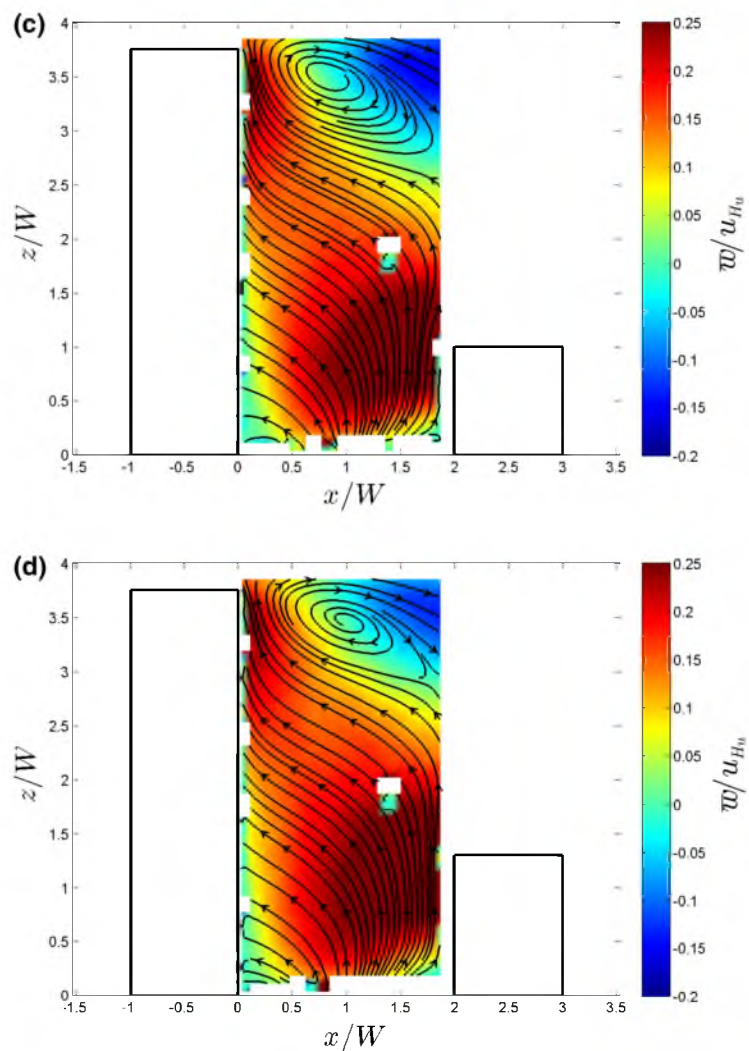


Fig. 11 continued

and extent) of the primary and secondary vortices reported in these studies are very different from that obtained from the current work. The differences again may be speculated to be due to the greater interaction between the rooftop and sidewall flows (over and around the upwind building) along the vertical symmetry plane, and the ventilation of the in-canyon flow in the lateral direction (x - y plane) around the downwind building, that the 2D simulations cannot capture.

In Fig. 13, normalized vertical profiles of the mean vertical (\bar{w}) velocities, and mean Reynolds shear stress ($\overline{u'w'}$) for $H_d/H_u \approx 0, 0.27, 0.53, 0.80,$ and 1 are shown. The profiles have been plotted at $x/S \approx 0.5 (\Rightarrow x/W \approx 0.75)$ in the canyon. From Fig. 13 it is seen that the magnitudes of the mean vertical velocities (\bar{w}) are higher in the bottom-half of the

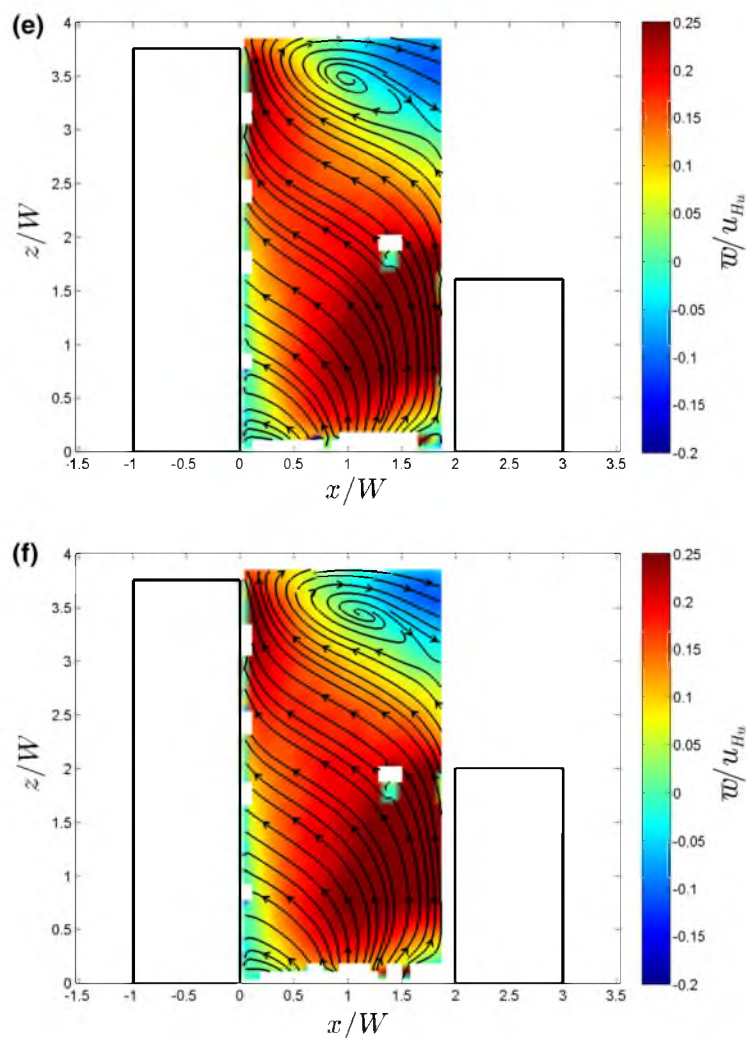


Fig. 11 continued

canyon in comparison to the top-half for $H_d/H_u \approx 0.27, 0.53, 0.80$, and are comparable for $H_d/H_u \approx 1$. This behavior is in contrast with that observed in 2D numerical simulations of deep canyon flows, wherein vertical velocities were significantly larger in the top-half of the canyon in comparison to the bottom-half [7]. Thus, it can again be seen that accurate prediction of tall building street-canyon flows requires taking into account momentum transport into the canyon in the lateral direction.

Comparing the vertical profiles of the normalized mean Reynolds shear stress at the canyon centers for $S \approx 2.5W$ and $S \approx 1.5W$, it is seen that the form of the profiles are slightly different in the lower-half of the canyon. For $S \approx 2.5W$, the Reynolds stress values in the canyon lower-half are predominantly positive, while for $S \approx 1.5W$, the values are predominantly negative. The difference in the behavior may be attributed to the

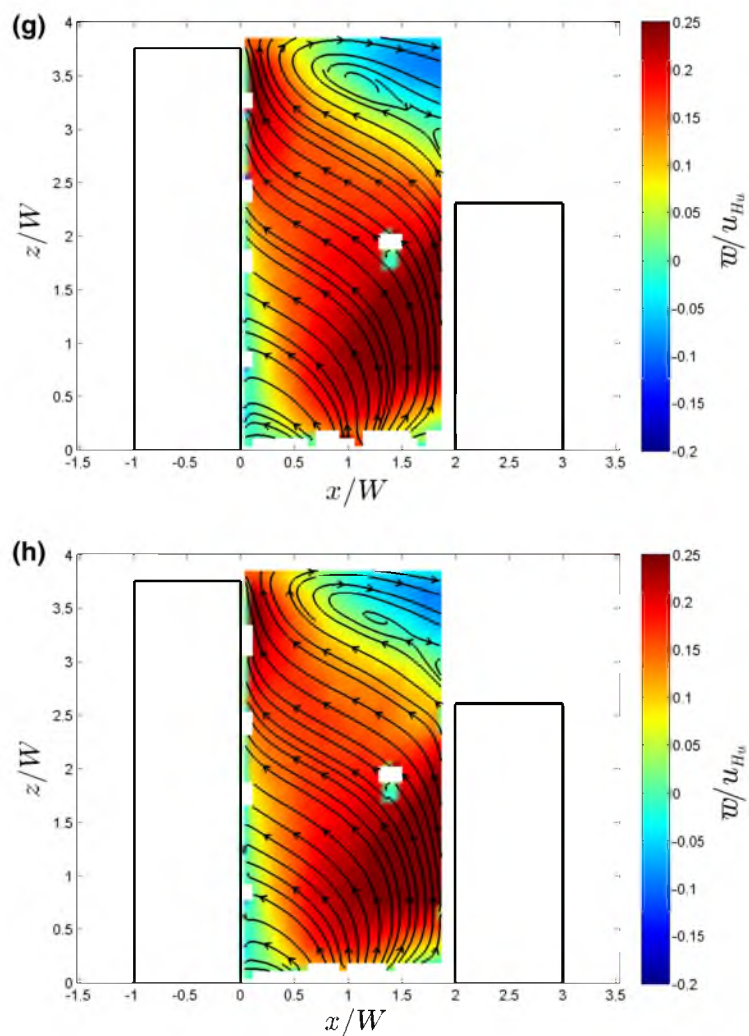


Fig. 11 continued

positioning of the downwind building relative to the ground shear layer (cavity dividing streamline). At lower street canyon widths, the interaction of the flow separating around the taller upwind building sidewalls with the downwind building affects the in-canyon flow statistics.

4.4 Step-down street canyons with $S \approx W$

In Fig. 14, contours of the mean vertical velocities (\overline{w}/u_{H_u}) and the mean streamline patterns in step-down canyons with $S \approx W$ are shown. Given that the ground originating shear layer (cavity dividing streamline) for an isolated tall building is at $x_{GSL} \approx W$, and given the

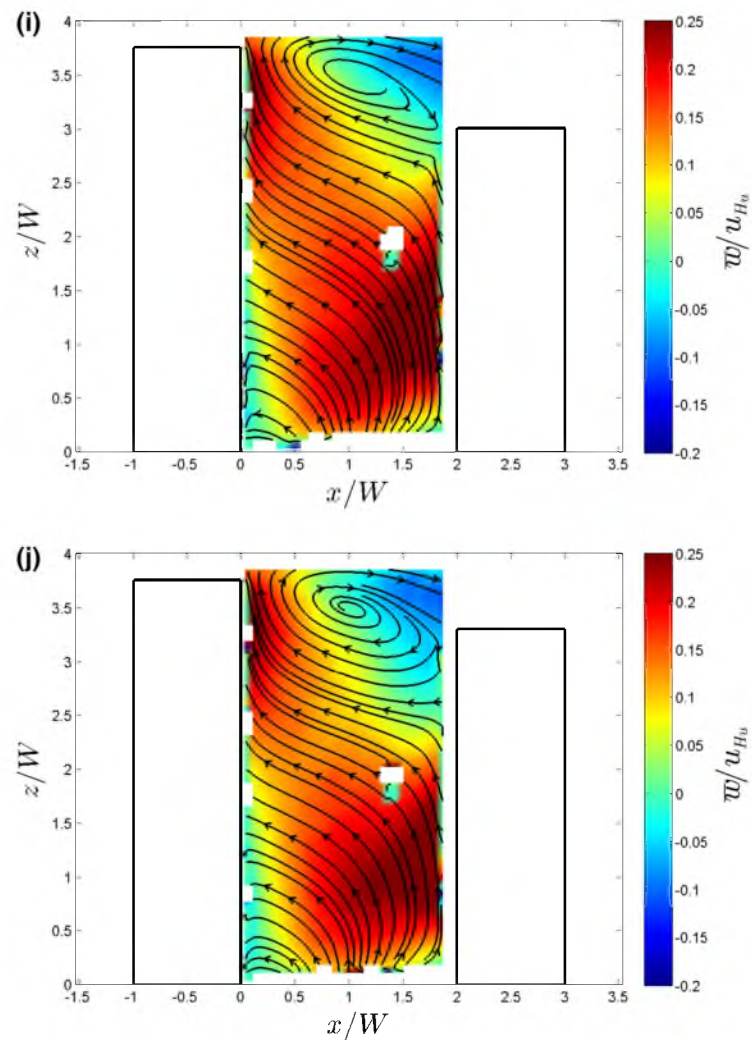


Fig. 11 continued

measurement domain (in the street canyon) for $S \approx W$, it is hard to make inferences on the effect of the downwind building height on the upwind building's wake. However, for $H_d/H_u \approx 1$, the in-canyon flow structure may be labeled as belonging to the *deep canyon skimming flow regime*. The classification is based both on the presence of a counter-rotating vortex pair, and the absence of the ground shear layer (cavity dividing streamline) in the canyon.

4.5 Effect of street canyon aspect ratio and building widths on the in-canyon flow structure

In terms of general street-canyon flows, [28] first proposed the well-known flow regime classification for pairs of cubical buildings resulting in street-canyons of varying canyon

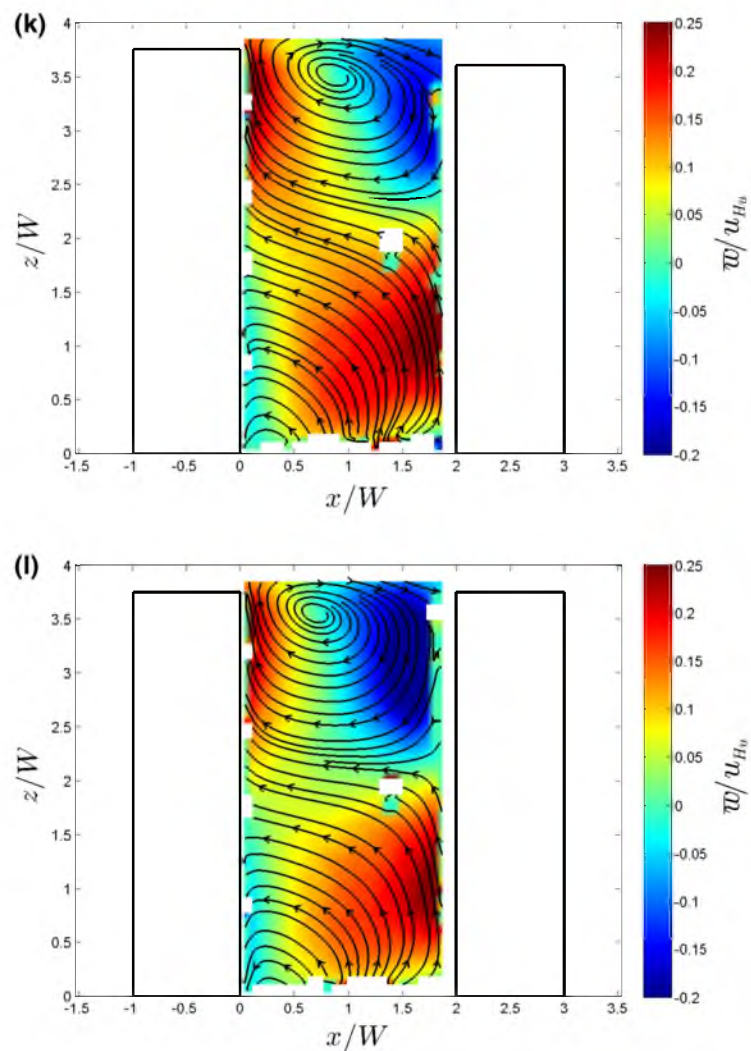


Fig. 11 continued

widths (S). Based on wind-tunnel experiments, it was proposed that the flow regime in the canyon is a function of the aspect ratio (H/S) of the street-canyon (where H is the height of the cubical building). Three flow regimes: *isolated roughness flow*, *wake interference*, and *skimming flow* were identified for different H/S values. It was reported that the in-canyon flow structure transitioned from *skimming* to *isolated roughness flow regimes* with decreasing H/S values. These flow regimes have been verified previously through wind-tunnel and field experiments, as well as numerical simulations [11, 12, 16, 24, 27, 29, 36, 43, 44, 47, 54, 63]. From these studies, it is evident that the flow regimes in a street-canyon are a function of the interaction of the downwind and upwind wakes of the upwind and downwind buildings.

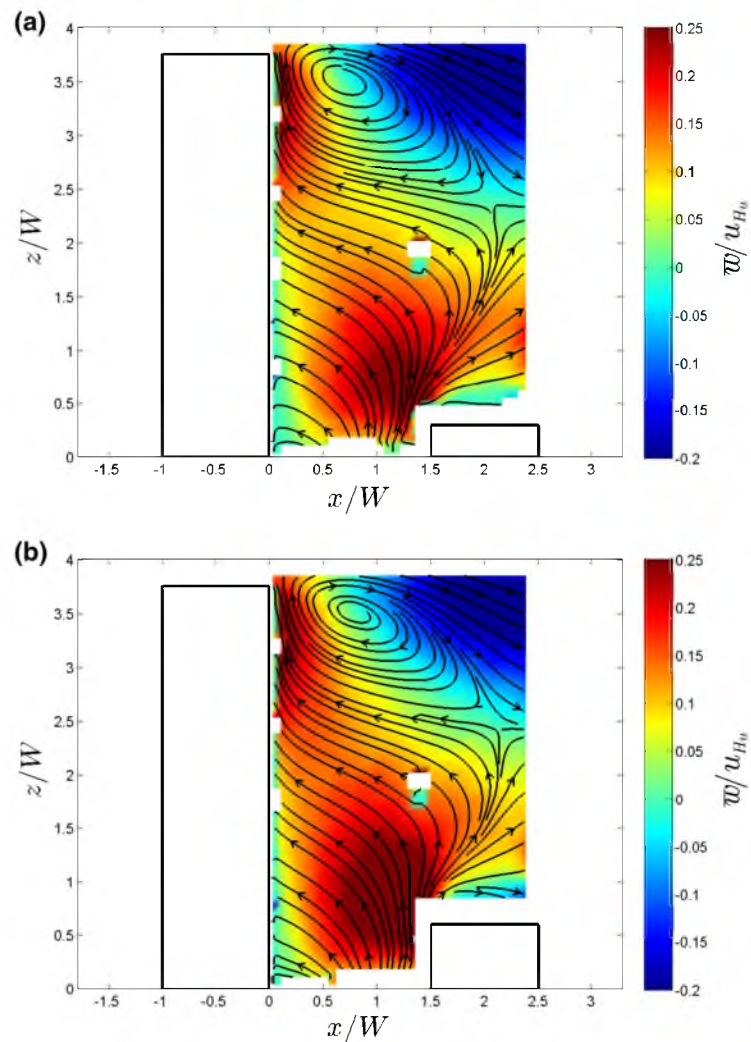


Fig. 12 Contours of the normalized mean vertical velocities (\bar{w}/u_{H_u}) in step-down canyons with $S/W \approx 1.5$ and $H_d/H_u \approx$, **a** 0.08, **b** 0.16, **c** 0.27, **d** 0.35, **e** 0.43, **f** 0.53, **g** 0.61, **h** 0.69, **i** 0.80, **j** 0.88, **k** 0.96, and **l** 1.00

The configurations for $H_d/H_u \approx 1$ and $S/W \approx 2.5, 2, 1.5, 1$ from the current work represent street canyons with aspect ratios, $H/S \approx 1.5, 1.875, 2.5, 3.75$. From the results obtained (Figs. 4, 11, 12, 14), it is seen that the flow regime classification proposed for cubical buildings may be extended to tall building (deep) street canyons. An important difference between the *skimming flow regimes* for cubical buildings and deep street canyons is the formation of the counter-rotating vortex pair for deep canyons.

From an alternate viewpoint, for a fixed building height ratio (say, $H_d/H_u \approx 1$), loosely speaking, decreasing the street canyon width from $S \approx 2.5W$ to $S \approx W$ may be argued to have effects similar to increasing the building widths (while maintaining constant street canyon width) from $W/S \approx 0.4$ to $W/S \approx 1$. Under such an assumption,

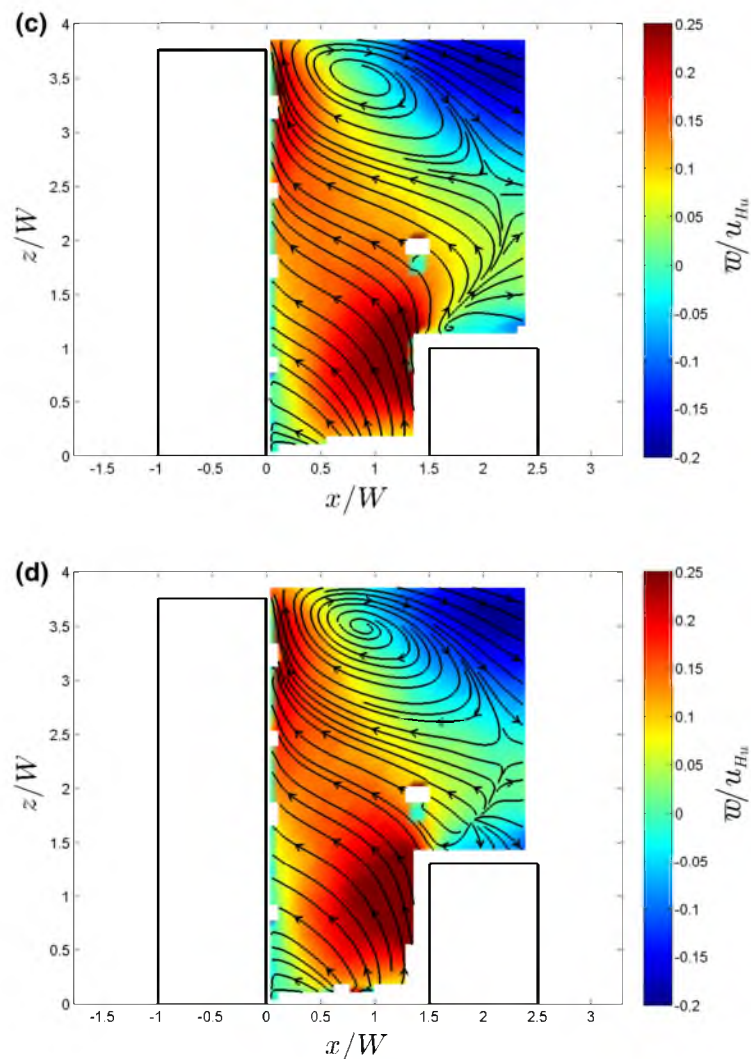


Fig. 12 continued

the formation of the counter-rotating vortex pair and the absence of the ground shear for $H_d/H_u \approx 1$ and $S/W \approx 1$ may be interpreted to be due to greater shielding of the flow along the vertical symmetry plane from the lateral flow entraining into the canyon (around the upwind building sidewalls) at lower street canyon widths (vis-a-vis higher building widths). Thus, the differences between the flow patterns observed in 2D simulations [7,48,62] and those reported in the current work, where more coherent flow structures were observed in the 2D simulations, may be attributed to the 3D street canyons considered (since a 2D street canyon may be viewed as a canyon formed by buildings of infinite widths).

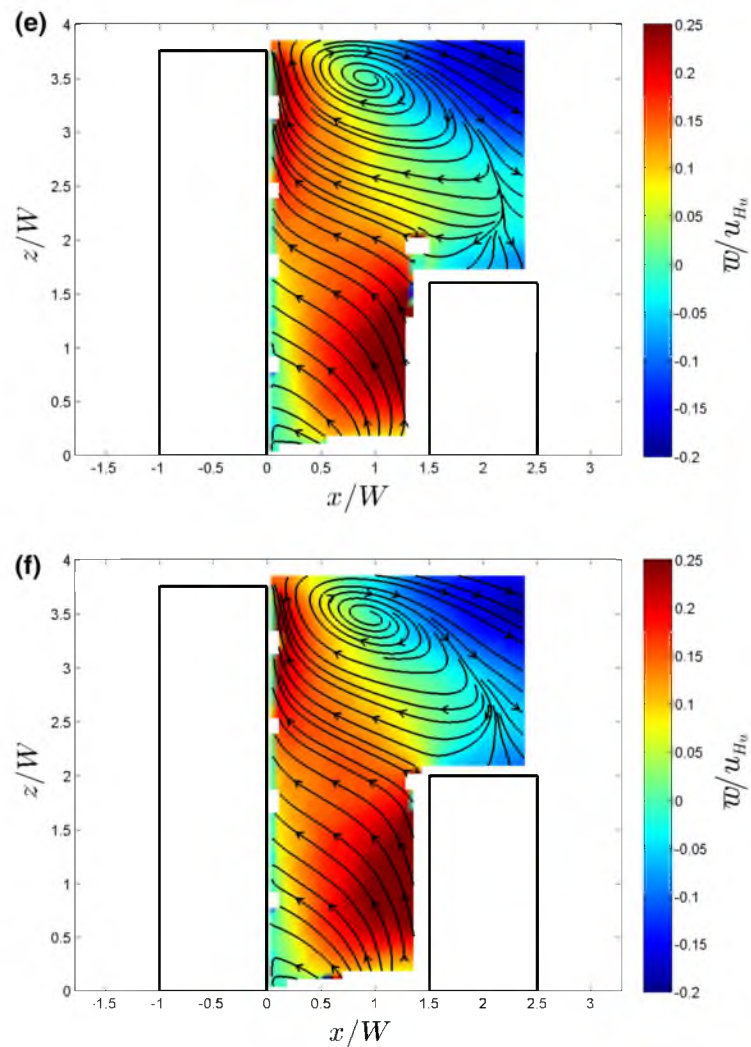


Fig. 12 continued

5 Summary

A step-down street canyon is a street canyon in which the upwind building height (H_u) is greater than the downwind building height (H_d) ($H_u > H_d$). In the work presented, the effect of the canyon geometry on the flow structure in isolated tall step-down street-canyons was investigated using wind-tunnel PIV measurements. For step-down canyons with buildings having square footprints with $H_u/W \approx 3.75$ and $S/W \leq 2.5$, the flow structure in the canyon is quite complex. For $S/W \approx 2.5, 2$, and 1.5 , increasing the downwind building height from $H_d/H_u \approx 0.08$ to 1 resulted in the in-canyon flow structure transitioning from *wake dominated* to *deep canyon wake interference regimes*. For $S/W \approx 1$, similar

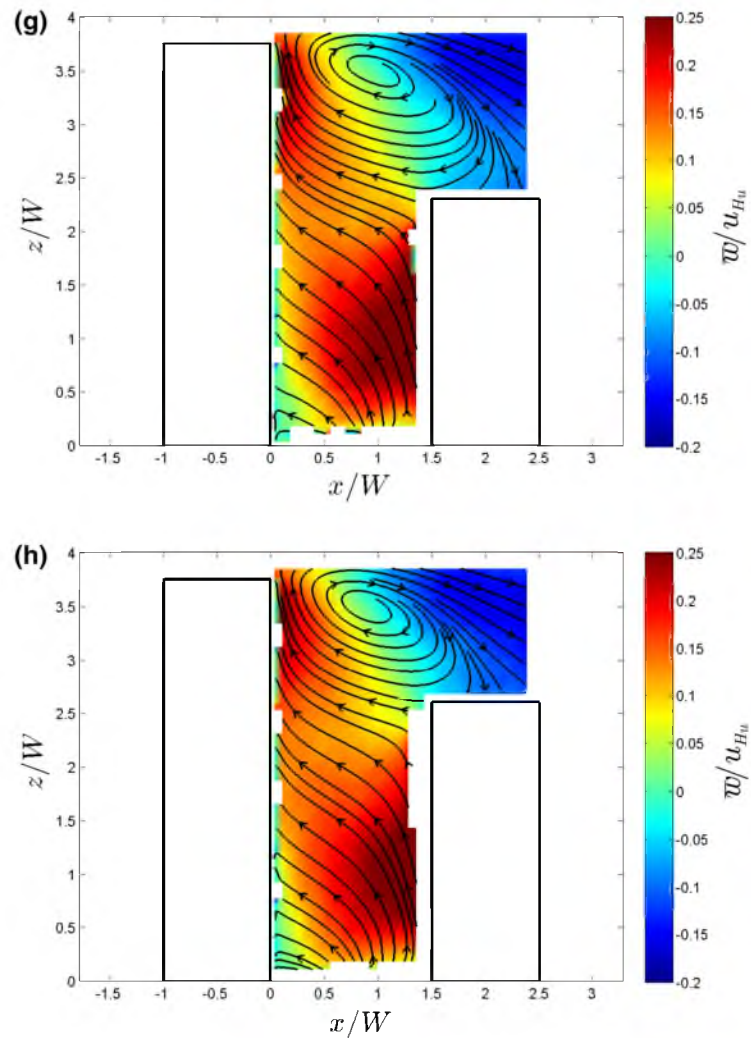


Fig. 12 continued

increases in the downwind building height resulted in the flow structure transitioning from *wake dominated* to *deep canyon skimming flow regime*. In the *wake dominated regime*, the characteristics of the flow topology are very similar to that of an isolated tall building. The basic flow topology in isolated tall building near-wake flows is characterized by a *bow-shaped* structure comprising a vortex core, a saddle point, and a ground originating shear layer. The *bow-shaped* structure adapts to the addition of a downwind building of varying heights. For the case $H_d/H_u \approx 1$ (which represents a deep canyon), decreasing the street canyon width from $S/W \approx 2.5$ to 1 resulted in the in-canyon flow structure transitioning from *deep canyon wake interference* to *deep canyon skimming flow regime*. As much as for $S/W \approx 2.5, 2,$ and 1.5 there exists a primary vortex in the top-half of the canyon (resembling that formed in lid-driven cavity flows), we hesitate to call this skimming flow, as the

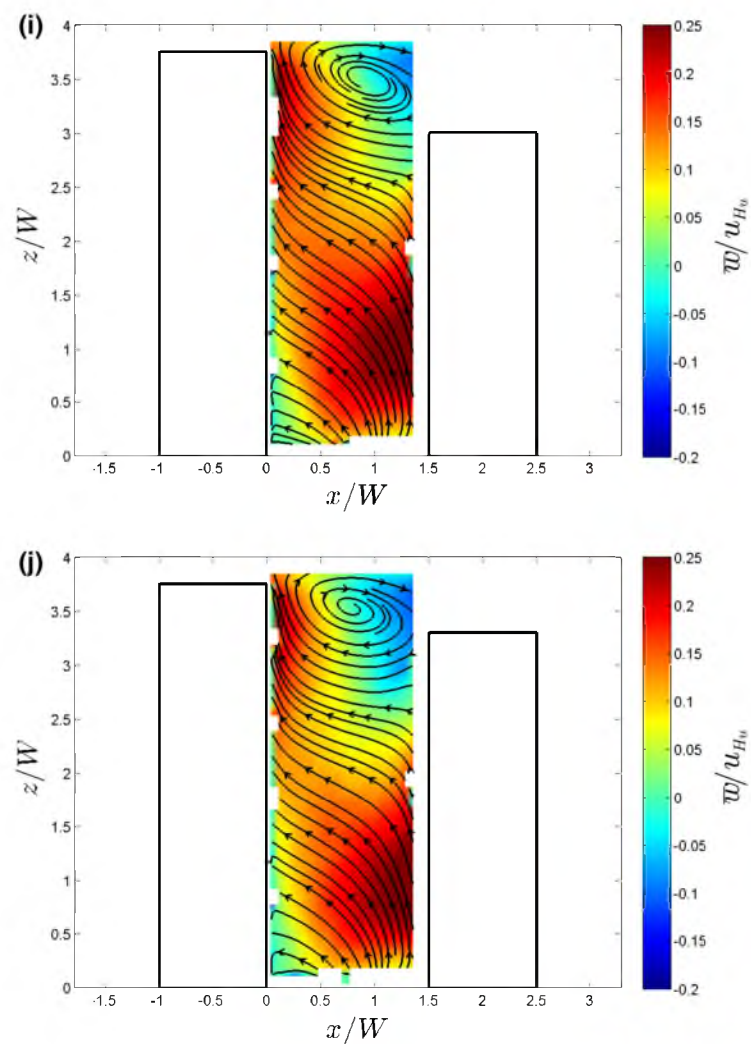


Fig. 12 continued

wake of the upstream building still results in very strong updrafts in the lower part of the canyon. In step-down canyons formed by tall and slender buildings, it can be concluded that the in-canyon flow patterns along the vertical symmetry plane strongly depend on the momentum transport into and out of the canyon around the building side walls. Among other consequences, momentum transport around the building sidewalls results in large vertical velocities (updrafts) in the lower part of the in-canyon region. Experiments run for step-up canyons [2] also demonstrated that the in-canyon flow patterns were driven largely by the taller upwind building. In summary, it seen that for normal approach flow, the flow patterns in the vicinity of tall buildings are strongly affected by the wakes of the tall buildings.

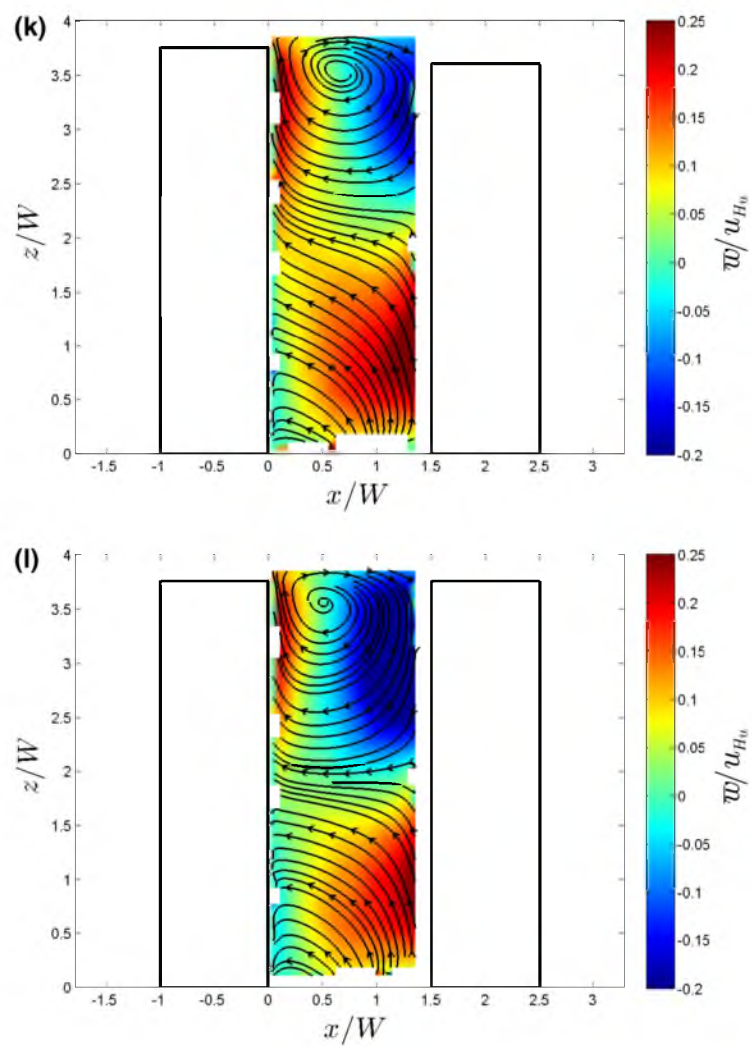


Fig. 12 continued

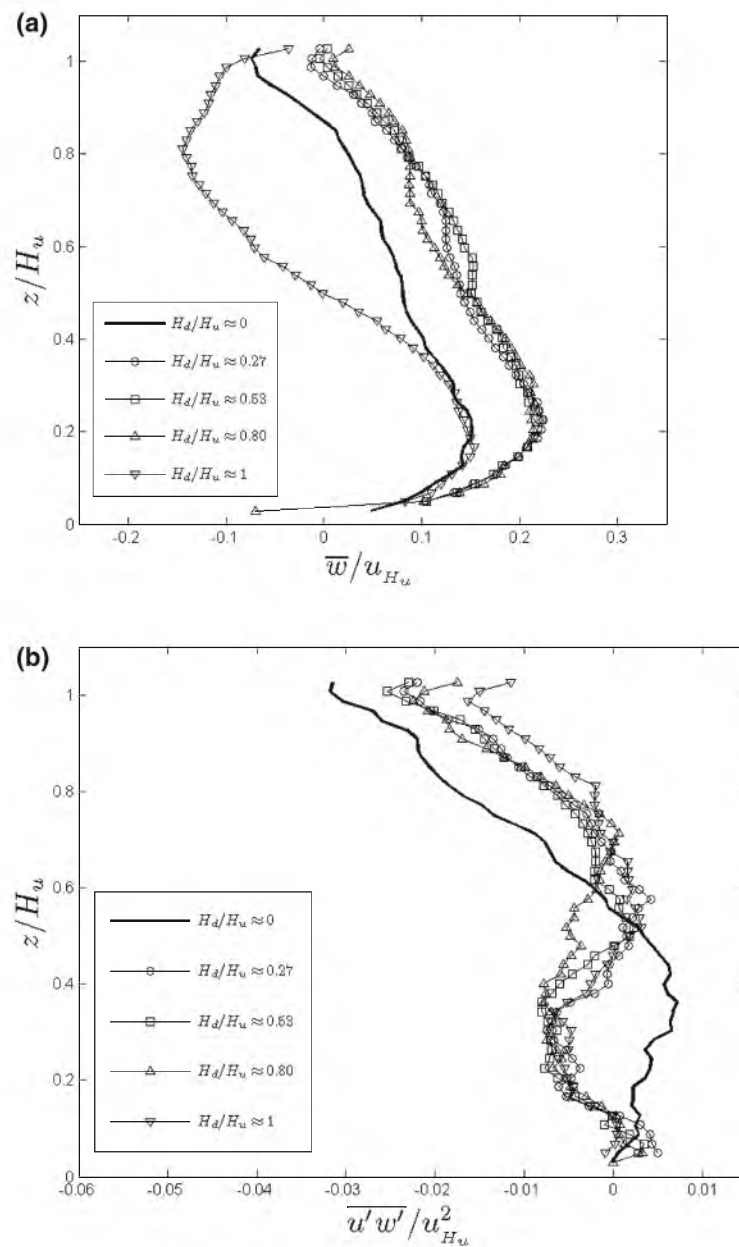


Fig. 13 For $S/W \approx 1.5$ and $H_d/H_u \approx 0, 0.27, 0.53, 0.80, 1$, at $x/S \approx 0.5$ ($\Rightarrow x/W \approx 0.75$), vertical profiles of, **a** normalized mean vertical velocity (\bar{w}/u_{H_u}), **b** normalized mean Reynolds shear stress ($\overline{u'w'}/u_{H_u}^2$)

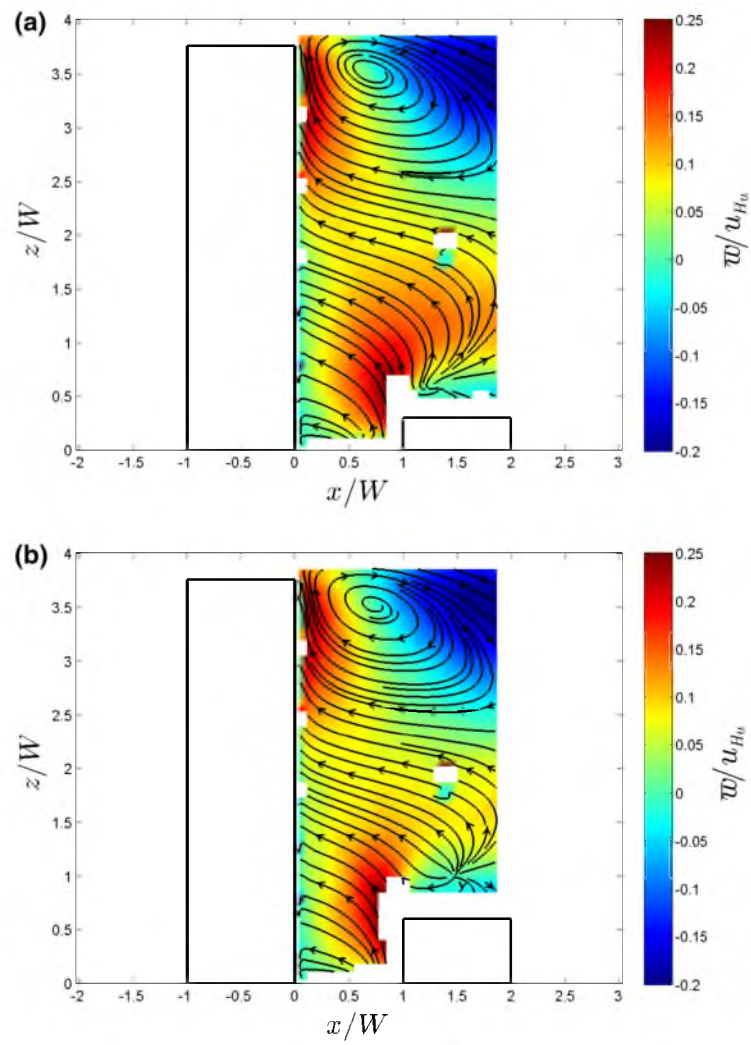


Fig. 14 Contours of the normalized mean vertical velocities (\bar{w}/u_{H_0}) in step-down canyons with $S/W \approx 1$ and $H_d/H_u \approx$, **a** 0.08, **b** 0.16, **c** 0.27, **d** 0.35, **e** 0.43, **f** 0.53, **g** 0.61, **h** 0.69, **i** 0.80, **j** 0.88, **k** 0.96, and **l** 1.00

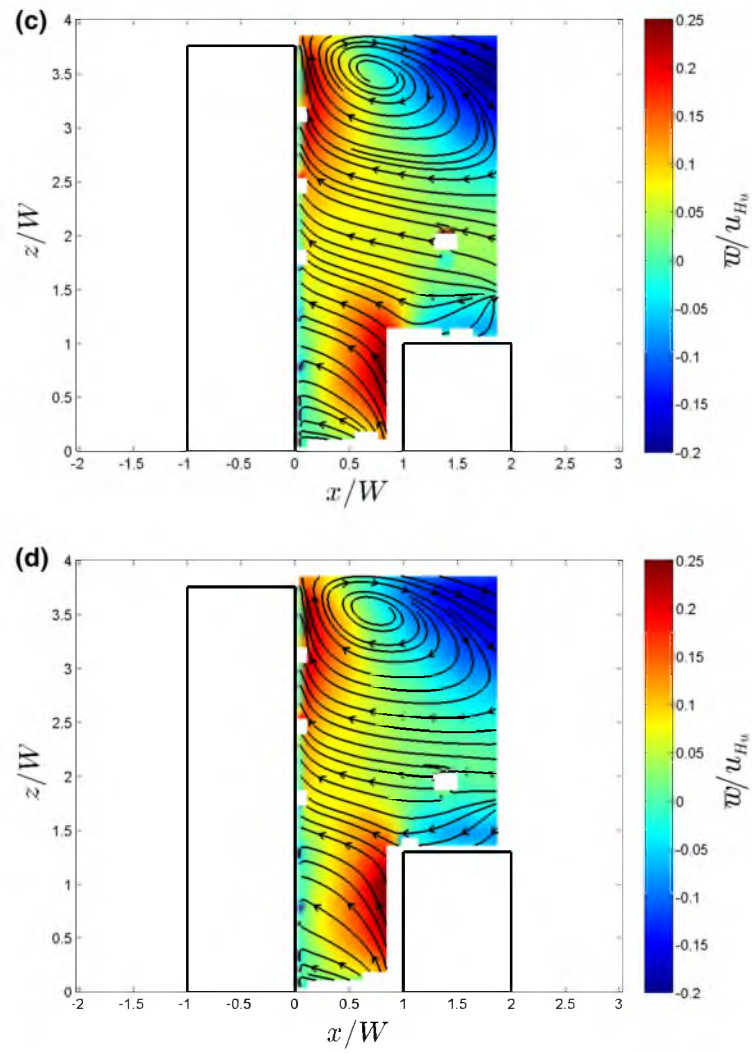


Fig. 14 continued

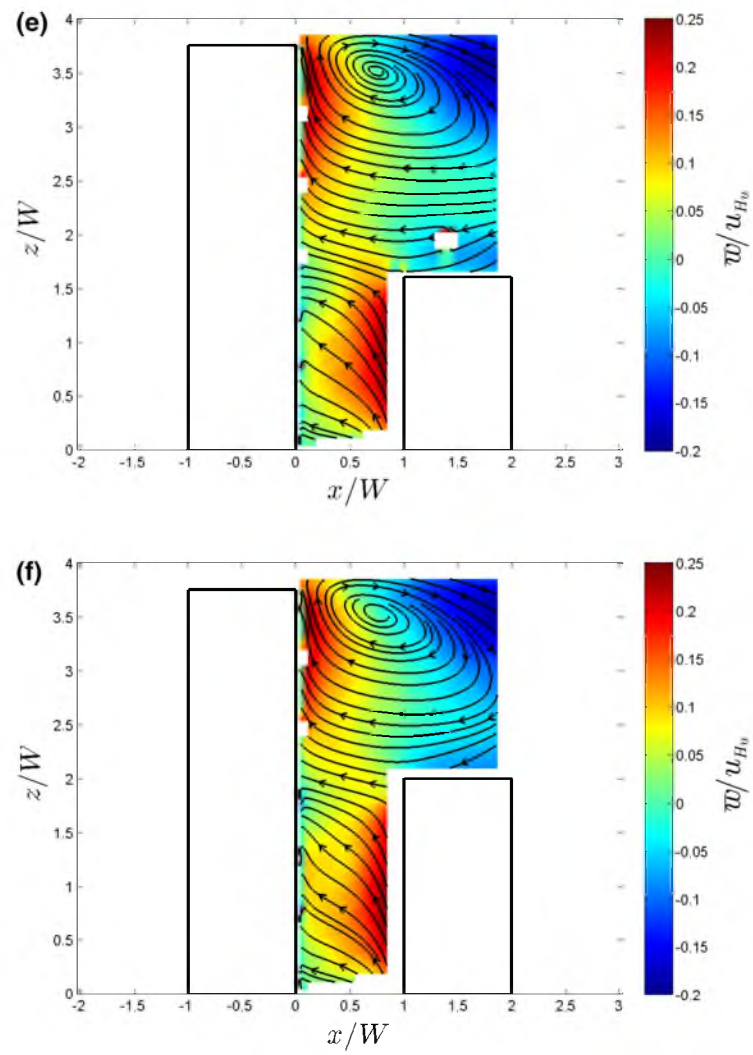


Fig. 14 continued

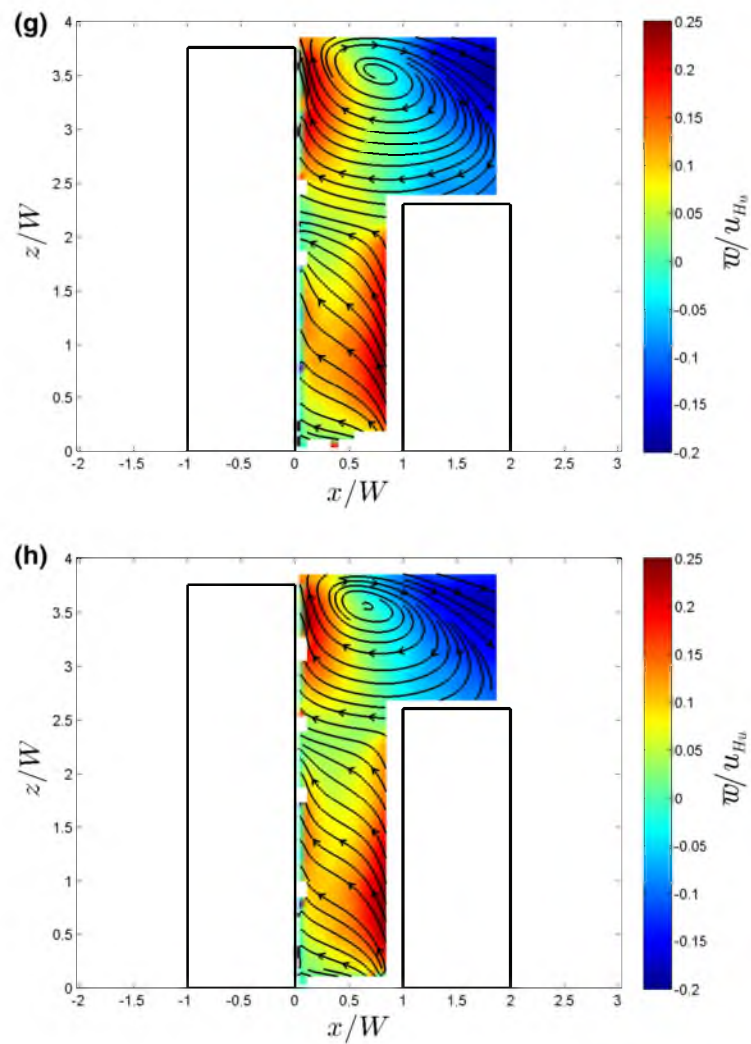


Fig. 14 continued

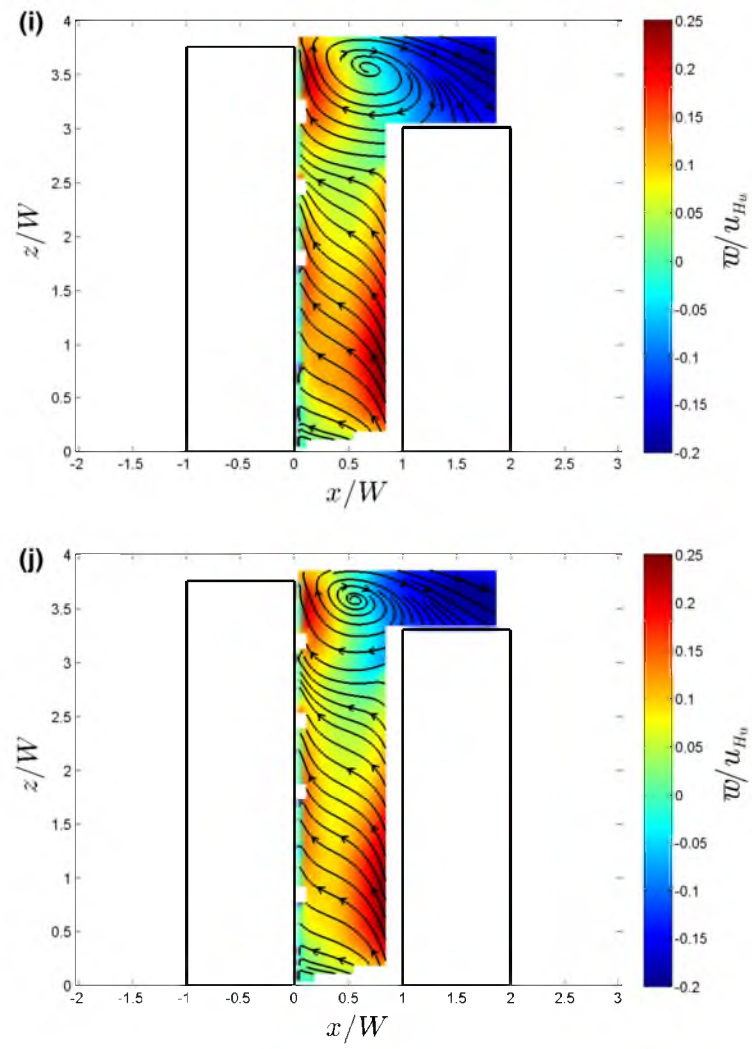


Fig. 14 continued

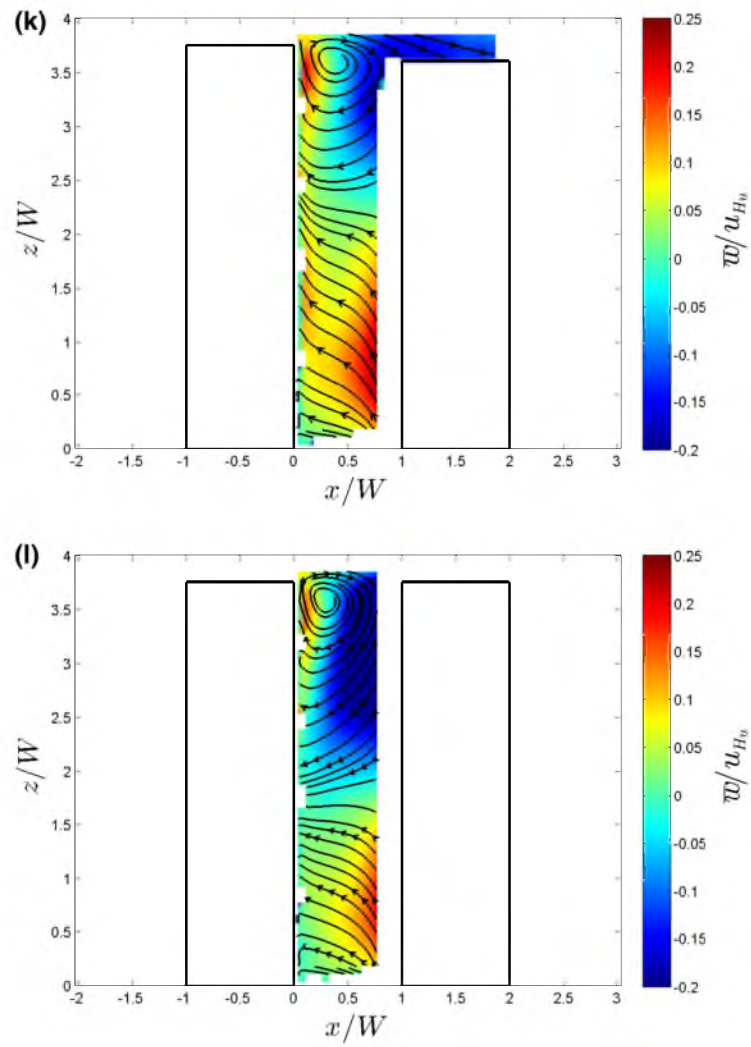


Fig. 14 continued

Acknowledgments This work was funded through an LDRD project by Dr. Robert E. Ecke, CNLS Director—Los Alamos National Laboratory. The financial support is gratefully acknowledged. We would also like to thank Dr. Michael J. Brown at the Los Alamos National Laboratory for his valuable inputs during the course of this research.

References

1. Addepalli B, Pardyjak ER (2007) Study of flow fields in asymmetric step-down street canyons. In: The international workshop on physical modelling of flow and dispersion phenomena (PHYSMOD 2007), University of Orleans, France, 10 pp
2. Addepalli B, Pardyjak ER (2013) Investigation of the flow structure in step-up street canyons—mean flow and turbulence statistics. *Boundary-Layer Meteorol* 148(1):133–155
3. Addepalli B, Brown MJ, Pardyjak ER, Senocak I (2007a) Evaluation of the QUIC-URB wind model using wind-tunnel data for step-up street canyons. In: American Meteorological Society Seventh symposium on urban environment, San Diego, CA, 11 pp
4. Addepalli B, Brown MJ, Pardyjak ER, Senocak I (2007b) Investigation of the flow structure around step-up, step-down, deep canyon, and isolated tall building configurations using wind-tunnel PIV measurements. In: American Meteorological Society seventh symposium on urban environment, San Diego, CA, 1 pp
5. Allegrini J, Dorer V, Carmeliet J (2013) Wind tunnel measurements of buoyant flows in street canyons. *Build Environ* 59:315–326
6. Assimakopoulos VD, ApSimon HM, Moussiopoulos N (2003) A numerical study of atmospheric pollutant dispersion in different two-dimensional street canyon configurations. *Atmos Environ* 37(29):4037–4049
7. Baik JJ, Kim JJ (1999) A numerical study of flow and pollutant dispersion characteristics in urban street canyons. *J Appl Meteorol* 38(11):1576–1589
8. Baik JJ, Park RS, Chun HY, Kim JJ (2000) A laboratory model of urban street-canyon flows. *J Appl Meteorol* 39(9):1592–1600
9. Baik JJ, Kwak KH, Park SB, Ryu YH (2012) Effects of building roof greening on air quality in street canyons. *Atmos Environ* 61:48–55
10. Baratian-Ghorgi Z, Kaye NB (2013) The effect of canyon aspect ratio on flushing of dense pollutants from an isolated street canyon. *Sci Tot Environ* 443:112–122
11. Chang CH (2001) Numerical and physical modeling of bluff body flow and dispersion in urban street canyons. *J Wind Eng Ind Aerodyn* 89(14):1325–1334
12. Chang CH (2003) Concentration and flow distributions in urban street canyons: wind tunnel and computational data. *J Wind Eng Ind Aerodyn* 91(9):1141–1154
13. Chang CH, Meroney RN (2001) Numerical and physical modeling of bluff body flow and dispersion in urban street canyons. *J Wind Eng Ind Aerodyn* 89(14–15):1325–1334, bluff Body Aerodynamics and Applications.
14. Dabberdt WF, Hoydysh WG (1991) Street canyon dispersion: sensitivity to block shape and entrainment. *Atmos Environ Part A* 25(7):1143–1153
15. Davies ME, Quincey VG, Tindall SJ (1980) Near-wake of a tall building block in uniform and turbulent flows. *Zement-Kalk-Gips* 1:289–298
16. DePaul FT, Sheih CM (1986) Measurements of wind velocities in a street canyon. *Atmos Environ* 20(3):455–459
17. Di Sabatino S, Solazzo E, Paradisi P, Britter R (2008) A simple model for spatially-averaged wind profiles within and above an urban canopy. *Boundary-Layer Meteorol* 127(1):131–151
18. Gousseau P, Blocken B, van Heijst G (2013) Quality assessment of large-eddy simulation of wind flow around a high-rise building: validation and solution verification. *Comput Fluids* 79:120–133
19. Gowardhan A, Pardyjak ER, Senocak I, Brown MJ (2007) Investigation of Reynolds stresses in a 3D idealized urban area using large eddy simulation. In: American Meteorological Society seventh symposium on urban environment, San Diego, CA, 8 pp
20. Gowardhan A, Brown M, Pardyjak E (2010) Evaluation of a fast response pressure solver for flow around an isolated cube. *Environ Fluid Mech* 10:311–328
21. Gromke C, Ruck B (2007) Influence of trees on the dispersion of pollutants in an urban street canyon—experimental investigation of the flow and concentration field. *Atmos Environ* 41(16):3287–3302
22. Gu ZL, Zhang YW, Cheng Y, Lee SC (2011) Effect of uneven building layout on air flow and pollutant dispersion in non-uniform street canyons. *Build Environ* 46(12):2657–2665

23. Higson H, Griffiths R, Jones C, Hall D (1996) Flow and dispersion around an isolated building. *Atmos Environ* 30(16):2859–2870, 6th EURASAP International Workshop on Wind and Water Tunnel Modelling of Atmospheric Flow and Dispersion.
24. Hotchkiss RS, Harlow HH (1973) Air pollution in street canyons. Tech. Rep. EPA R4-73-029, US EPA, 78 pp
25. Hoydysh WG, Dabberdt WF (1988) Kinematics and dispersion characteristics of flows in asymmetric street canyons. *Atmos Environ* 22(12):2677–2689
26. Hui Y, Tamura Y, Yoshida A, Kikuchi H (2013) Pressure and flow field investigation of interference effects on external pressures between high-rise buildings. *J Wind Eng Ind Aerodyn* 115:150–161
27. Hunter LJ, Watson ID, Johnson GT (1990) Modelling air flow regimes in urban canyons. *Energy Build* 15(3–4):315–324
28. Hussain M, Lee BE (1980) A wind tunnel study of the mean pressure forces acting on large groups of low-rise buildings. *J Wind Eng Ind Aerodyn* 6(3–4):207–225
29. Jiang Y, Liu H, Sang J, Zhang B (2007) Numerical and experimental studies on flow and pollutant dispersion in urban street canyons. *Adv Atmos Sci* 24(1):111–125
30. Kanda M, Moriwaki R, Kasamatsu F (2004) Large-eddy simulation of turbulent organized structures within and above explicitly resolved cube arrays. *Boundary-Layer Meteorol* 112:343–368
31. Kastner-Klein P, Plate E (1999) Wind-tunnel study of concentration fields in street canyons. *Atmos Environ* 33(24–25):3973–3979
32. Kastner-Klein P, Rotach MW (2004) Mean flow and turbulence characteristics in an urban roughness sublayer. *Boundary-Layer Meteorol* 111:55–84
33. Kastner-Klein P, Fedorovich E, Rotach M (2001) A wind tunnel study of organised and turbulent air motions in urban street canyons. *J Wind Eng Ind Aerodyn* 89(9):849–861
34. Kastner-Klein P, Berkowicz R, Britter R (2004) The influence of street architecture on flow and dispersion in street canyons. *Meteorol Atmos Phys* 87:121–131
35. Kellnerova R, Kukacka L, Jurcakova K, Uruba V, Janour Z (2012) PIV measurement of turbulent flow within a street canyon: detection of coherent motion. *J Wind Eng Ind Aerodyn* 104–106:302–313
36. Kim JJ, Baik JJ (1999) A numerical study of thermal effects on flow and pollutant dispersion in urban street canyons. *J Appl Meteorol* 38(9):1249–61
37. Kim JJ, Baik JJ (2001) Urban street-canyon flows with bottom heating. *Atmos Environ* 35(20):3395–3404
38. Kim JJ, Baik JJ (2003) Effects of inflow turbulence intensity on flow and pollutant dispersion in an urban street canyon. *J Wind Eng Ind Aerodyn* 91(3):309–329
39. Louka P, Belcher S, Harrison R (1998) Modified street canyon flow. *J Wind Eng Ind Aerodyn* 74–76:485–493
40. Melling A (1997) Tracer particles and seeding for particle image velocimetry. *Meas Sci Technol* 8:1406–1416
41. Mirzai M, Harvey J, Jones C (1994) Wind tunnel investigation of dispersion of pollutants due to wind flow around a small building. *Atmos Environ* 28(11):1819–1826
42. Ohba M (1998) Experimental study of effects of separation distance between twin high-rise tower models on gaseous diffusion behind the downwind tower model. *J Wind Eng Ind Aerodyn* 77–78:555–566
43. Oke TR (1987) *Boundary layer climates*, 2nd edn. Routledge, London 435 pp
44. Oke TR (1988) Street design and urban canopy layer climate. *Energy Build* 11(1–3):103–113
45. Rotach M (1993) Turbulence close to a rough urban surface, Part I: Reynolds stress. *Boundary-Layer Meteorol* 65:1–28
46. Sagrado APG, van Beeck J, Rambaud P, Olivari D (2002) Numerical and experimental modelling of pollutant dispersion in a street canyon. *J Wind Eng Ind Aerodyn* 90(4–5):321–339
47. Salizzoni P, Soulhac L, Mejean P (2009) Street canyon ventilation and atmospheric turbulence. *Atmos Environ* 43(32):5056–5067
48. Santiago JL, Martin F (2005) Modelling the air flow in symmetric and asymmetric street canyons. *Int J Environ Pollut* 25(1):145–154
49. Santos JM, Reis NC Jr, Goulart EV, Mavroidis I (2009) Numerical simulation of flow and dispersion around an isolated cubical building: the effect of the atmospheric stratification. *Atmos Environ* 43(34):5484–5492
50. Shao J, Liu J, Zhao J (2012) Evaluation of various non-linear $k-\epsilon$ models for predicting wind flow around an isolated high-rise building within the surface boundary layer. *Build Environ* 57:145–155
51. Simoens S, Wallace JM (2008) The flow across a street canyon of variable width—part 2: scalar dispersion from a street level line source. *Atmos Environ* 42(10):2489–2503
52. Singh B, Hansen B, Brown M, Pardyjak E (2008) Evaluation of the QUIC-URB fast response urban wind model for a cubical building array and wide building street canyon. *Environ Fluid Mech* 8(4):281–312
53. Singh B, Pardyjak ER, Norgren A, Willemsen P (2011) Accelerating urban fast response lagrangian dispersion simulations using inexpensive graphics processor parallelism. *Environ Model Softw* 26(6):739–750

54. Sini JF (1996) Pollutant dispersion and thermal effects in urban street canyons. *Atmos Environ* 30(15):2659–2677
55. Snyder WH, Lawson RE (1994) Wind-tunnel measurements of flow fields in the vicinity of buildings. In: Eight joint conference on application of air pollution meteorology with A&WMA. American Meteorological Society, Nashville, pp 240–250
56. So ES, Chan AT, Wong AY (2005) Large-eddy simulations of wind flow and pollutant dispersion in a street canyon. *Atmos Environ* 39(20):3573–3582
57. Soulhac L, Mejean P, Perkins R (2001) Modelling the transport and dispersion of pollutants in street canyons. *Int J Environ Pollut* 16(1):404–416
58. Takano Y, Moonen P (2013) On the influence of roof shape on flow and dispersion in an urban street canyon. *J Wind Eng Ind Aerodyn* 123(Part A):107–120
59. Tominaga Y, Mochida A, Murakami S, Sawaki S (2008) Comparison of various revised $k-\epsilon$ models and LES applied to flow around a high-rise building model with 1:1:2 shape placed within the surface boundary layer. *J Wind Eng Ind Aerodyn* 96(4):389–411
60. Tong NY, Leung DY (2012) Effects of building aspect ratio, diurnal heating scenario, and wind speed on reactive pollutant dispersion in urban street canyons. *J Environ Sci* 24(12):2091–2103
61. Tutar M, Oguz G (2002) Large eddy simulation of wind flow around parallel buildings with varying configurations. *Fluid Dyn Res* 31(5–6):289–315
62. Xie X, Huang Z, song Wang J (2005) Impact of building configuration on air quality in street canyon. *Atmos Environ* 39(25):4519–4530
63. Xueling C, Fei H (2005) Numerical studies on flow fields around buildings in an urban street canyon and cross-road. *Adv Atmos Sci* 22(2):290–299
64. Zhang Y, Arya S, Snyder W (1996) A comparison of numerical and physical modeling of stable atmospheric flow and dispersion around a cubical building. *Atmos Environ* 30(8):1327–1345

CHAPTER 4

**SOURCE CHARACTERIZATION OF
ATMOSPHERIC RELEASES USING
STOCHASTIC SEARCH AND
REGULARIZED GRADIENT
OPTIMIZATION**

B. Addepalli, K. Sikorski, E.R. Pardyjak, and M.S. Zhdanov, Source characterization of atmospheric releases using stochastic search and regularized gradient optimization, *Inverse Probl. Sci. Eng.* 8 (2011), pp. 1097 - 1124. Reprinted with kind permission from Taylor and Francis Group.

Source characterization of atmospheric releases using stochastic search and regularized gradient optimization

B. Addepalli^a, K. Sikorski^b, E.R. Pardyjak^{a*} and M.S. Zhdanov^c

^a*Department of Mechanical Engineering, University of Utah, Salt Lake City 84112, USA;*

^b*School of Computing, University of Utah, Salt Lake City 84112, USA;*

^c*Department of Geology and Geophysics, University of Utah, Salt Lake City 84112, USA*

(Received 31 March 2010; final version received 13 May 2011)

In this work, an inversion technique comprising stochastic search and regularized gradient optimization is used to solve the atmospheric source characterization problem. The inverse problem comprises retrieving the spatial coordinates, source strength and the wind speed and wind direction at the source, given certain receptor locations and concentration values at these receptor locations. The Gaussian plume model is adopted as the forward model and derivative-based optimization is chosen to take advantage of its simple analytical nature. A new misfit functional that improves the inversion accuracy of atmospheric inverse-source problems is developed and is used in the solution procedure. Stochastic search is performed over the model parameter space to identify a good initial iterate for the gradient scheme. Several Quasi-Monte Carlo point-sets are considered in the stochastic search stage and their performance is evaluated against the Mersenne–Twister pseudorandom generator. Newton's method with the Tikhonov stabilizer and adaptive regularization with quadratic line-search is implemented for gradient optimization. As the forward modelling and measurement errors for atmospheric inverse problems are usually unknown, issues concerning 'model-fit' and 'data-fit' are examined. In this article, the workings and validation of the proposed approach are presented using field data from the Copenhagen tracer experiments.

Keywords: inverse-source problem; Gaussian plume model; Monte Carlo; Quasi-Monte Carlo; regularized Newton's method; quadratic line-search

AMS Subject Classifications: 15A29; 11K45; 60J60

1. Introduction

The solution of inverse problems involves the retrieval of information about a physical process or phenomenon from known or observed data [1]. Inverse problems arise in various fields and hence techniques to solve such problems have been an area of extensive study. One of the contemporary applications of inversion techniques includes the source characterization problem for atmospheric contaminant dispersion. Atmospheric source characterization problems, also referred to as event reconstruction, source-inversion or

*Corresponding author. Email: pardyjak@eng.utah.edu

inverse-source problems, comprise characterizing the source of a chemical/biological/radiological (CBR) agent released into the atmosphere. Source characterization typically involves predicting the release location and rate of the CBR agent and the meteorological conditions at the release site, based on the time-averaged concentration and wind measurements obtained from a distributed sensor network in the region of interest. In this article, an inversion technique developed to retrieve the spatial coordinates, source strength and the wind speed, and wind direction at the source, using concentration measurements from known receptor locations in the domain is described.

Efficient and robust event reconstruction tools can play a crucial role in the event of accidental or deliberate release of CBR agents in or close to urban centres. Under such circumstances, quick and accurate reconstruction can help government agencies evacuate people from the affected regions. Also, using the information obtained from inversion, forward models can be run to estimate the extent of the plume spread and the consequent exposure. Event reconstruction tools can also be of use to environmental monitoring agencies as they can help evaluate the contribution of the stack releases from various industries close to urban areas to the air quality within urban areas. Therefore, from the perspective of public safety and national security, a fast, robust and accurate atmospheric event reconstruction tool is pivotal for air-quality management and to effectively deal with emergency response scenarios.

It is generally well-accepted that a single best procedure to solve an inverse problem does not exist. For inverse problems having small domains and few decision variables, conducting an exhaustive grid search is the most robust inversion technique [2]. For larger problems, the performance of a solution technique depends upon the problem at hand, the nature of the forward model, and the manner in which the inverse problem is formulated. Inverse problems are also difficult to solve owing to their inherent ill-posedness, i.e. the existence, uniqueness and stability of the computed solution. For real-life inverse problems, the question of existence is more mathematical than physical [1,3]. This is also true for the present case, wherein the sensor network recording a measurement suggests the existence of a solution to the source characterization problem. However, to date, there is no formal proof for the existence of solutions to inverse problems with contaminated data, and seldom do we obtain noise-free data from measuring devices [3]. Therefore, for the accurate retrieval of the model parameters (m), the knowledge of the uncertainty in the observed data (d_{obs}) is absolutely essential. In short, one needs to know the uncertainties (δ) in the data to know what it means to fit the data [3].

The solution phase of inverse problems can be divided into two stages [3]: (1) the estimation stage, and (2) the appraisal stage. The estimation stage involves using an inversion algorithm to predict a set of model parameters (m_{pr}) based on the observed data (d_{obs}). The appraisal stage is comprised of determining how well the data generated (d_{pr}) using the predicted model parameters (m_{pr}) fits the observed data (d_{obs}) [1]. Errors arising in inversion and the inherent ill-posedness associated with inverse problems can be accounted for in one of these two stages. Errors arising in the inversion procedure can be attributed to one of the four possible sources: (1) the forward modelling error (δ_{FM}), (2) measurement error (δ_{M}), (3) non-uniqueness and (4) nonlinear error propagation. For real-life problems, the forward modelling error (δ_{FM}) is inevitable. This is because no forward model (A) can ever incorporate all the physics associated with the problem. During inversion, the forward modelling (δ_{FM}) and the measurement errors (δ_{M}) may be accounted for in the estimation stage. Non-uniqueness arises primarily due to one of the following four factors: (1) retrieval of a model that may have infinite degrees of freedom

from finite amount of data, (2) lack of information – this is especially true when solving an under-determined system, (3) correlation between the model parameters (m) and (4) distortion of the misfit functional space due to the previously mentioned errors resulting in multiple optimal solutions. Non-uniqueness and nonlinear error propagation (that is intractable) can be accounted for during the appraisal stage. Due to these uncertainties in the solution procedure, one usually defines a ‘data-fit’ or ‘model-acceptancy’ criterion (β) based on any prior information available about the noise level (δ) [4–7]. In summary, the goal of inversion is to find a set of model parameters (m_{pr}) that fit the observed data (d_{obs}) to some prescribed level (β).

Given that the subject of source characterization of atmospheric contaminant dispersion is in its infancy, researchers have examined the applicability and effectiveness of the various available inversion procedures to solve such problems. The solution methodologies used span the range of deterministic (adjoint methods), stochastic (simulated annealing (SA), genetic algorithms (GA), Bayesian inference using Markov Chain Monte Carlo (MCMC) sampling) and ‘common-sense’ methods (collector footprint methods). The inverse-source problem has been solved over local [8,9], regional [10,11] and continental scales [12] for different model parameters (m) using empirical, diagnostic and prognostic models for scalar transport as the forward operator (A). Apart from identifying the source parameters, inversion techniques have also been used to estimate model coefficients in forward operators used to characterize atmospheric dispersion [12,13]. Table 1 summarizes the salient features of the inversion procedures adopted by some of the research groups across the world to solve the inverse-source problem.

All inversion techniques have their own merits and demerits and the approaches found in Table 1 are no exception. Adjoint methods, apart from requiring a good initial guess, also require the misfit functional to be continuous and differentiable. Hence, they are more likely to get trapped in local minima since inverse problems are often characterized by misfit functionals that have multiple critical points (maxima, minima and saddle points). Also, for problems that have complicated forward operators in the form of partial differential equations (PDEs), adjoint methods can be computationally expensive as they require the forward model evaluation and the Frechet evaluation over the entire domain on every iteration (when Newton’s method is employed, evaluation of the inverse of the Hessian over the entire domain is required). Therefore, problems that have complicated (non-convex) misfit functional surfaces often require stochastic search methods in order to distinguish the local minima from the global minima. The computational efficiency of guided-search algorithms such as SA and GA also depends on the forward operator, as every iteration of these algorithms requires the forward operator to be evaluated. Adjoint methods, SA and GA also carry the added disadvantage that they only provide a single model that fits the data rather than giving a set of acceptable models. Though Bayesian inference techniques appear robust and give probabilistic answers, they rely heavily upon the manner in which prior information is included into the initial probability distribution [14]. The posterior distribution is then computed using MCMC sampling, which also requires the forward model to be evaluated on every iteration, and hence can get computationally intractable in higher dimensions [3].

In this article, an approach that has the combined benefits of stochastic search and gradient descent methods is presented. The workings of the proposed approach are explained using field experiment data (the Copenhagen tracer experiments – TCTE) [15]. The objective of conducting stochastic search is to provide the gradient optimization scheme a good starting solution (m_{STOCH}). It should be noted that the stochastic search is

Table 1. Salient features of various inversion techniques used to solve atmospheric source characterization problems.

Ref.	Model parameters (m)	Forward model (A)	Inversion technique	Validation procedure	Application	Performance
[10]	Q_s	Steady laminar incompressible Navier-Stokes solver + ADE	Adjoint method	Synthetic data without noise	Contamination dispersion	
[16]	$x_s, y_s, z_s, Q_s, u_s, \theta_s, \delta_s$	Gaussian puff	GA	Synthetic data without noise	Atmospheric source inversion	
[17]	x_s, y_s, Q_s	GPM	Detector footprint method	Synthetic data with and without noise	Atmospheric source inversion	
[8]	x_s, y_s, z_s, Q_s	FEM3MP – 3D	Bayesian inference + MCMC	Synthetic and field data	Atmospheric source inversion	(1) 2560 forward runs (2) Total computation time: over 12 h on 1024 2.4 GHz Xeon processors
[11]	z_s, I_s	Chemistry transport model – POLAIR 3D	Adjoint method		Reconstruction of Chernobyl accident source term	
[18]	$x_s, y_s, Q_s, u_s, \theta_s$	GPM	GA	Synthetic data without noise	Atmospheric source inversion	(1) 2000 generations meteorological parameters

	stability class					(2) 10,000 generations for x_s, y_s, Q_s, θ_s & stability
[12]	$f_{j,m}, s_{OH}, s_{stea}, c_0$	Global atmospheric CTM	Adjoint method	Field data	Global-scale sources & sinks of methane	
[19]	x_s, y_s, z_s, Q_s	GPM	Expectation maximization	Synthetic data without noise	Atmospheric source inversion	
[20]	x_s, y_s, Q_s, θ_s	Gaussian puff	GA + simplex optimization	Synthetic data without noise		(1) 1200 chromosomes (2) 100 GA iterations
[21]	Q_s	Langevin model	Quasi-Newton and SA	Field data	Atmospheric source inversion	(1) 65 quasi-Newton iterations (2) 1575 SA iterations
[9]	$x_s, y_s, z_s, Q_s, u_s, \theta_s$	GPM	Bayesian inference + MCMC	Field data	Atmospheric source inversion	50,000 MCMC evaluations
[13]	K_{xx}, u^*, L, z_0	2D ADE	Levenberg–Marquardt method	Field data	Identification of atmospheric boundary layer parameters	
[22]	x_s, y_s, z_s, Q_s	GPM	SA	Field data	atmospheric ethane used to locate ground-level sources	4×10^6 iterations

Note: t_s – temporal release profile, $f_{j,m}$ – integrated surface emission over region j & month m , s_{OH} – parametrization for chemical removal of methane with hydroxyl radical, s_{stea} – stratospheric methane loss, c_0 – global mean methane concentration, K_{xx} – longitudinal turbulent diffusivity, u^* – friction velocity, L – Monin-Obukhov length, z_0 – aerodynamic surface roughness, CTM – chemistry transport model, GPM – Gaussian plume model, SA – simulated annealing, ADE – advection–diffusion equation, GA – genetic algorithm.

not a guided-search and this ensures that the misfit functional space has been uniformly sampled, thereby reducing the possibility of getting stuck in local minima. Three strategies for solving the inverse-source problem in general and computing the ‘data-fit’ criterion (β_{STOCH}) for the stochastic search stage in particular are discussed. Gradient optimization (Newton’s method) is performed with the initial iterate provided by the stochastic search stage (m_{STOCH}). The ‘model-acceptancy’ criterion (β_{GD}) for the gradient scheme is based on the L_2 -norm of the difference between predicted and observed data vectors in the iteration space. The Gaussian plume dispersion model is adopted as the forward model because of its theoretical and computational simplicity. The proposed approach is used to retrieve the source parameters from TCTE [15], and the results obtained are compared against the true parameters. The works of [9,21] also used the Copenhagen data to demonstrate quasi-Newton and Bayesian inference approaches to the inverse problem. The results obtained from this work are compared to those obtained by [9,21].

Apart from the hybrid approach proposed, this article also investigates some of the vital aspects of the atmospheric source characterization problem when using the Gaussian plume model (GPM) as the forward operator. The first feature examined is the effect of the misfit functional formulation on the accuracy and complexity of inversion. Based on this study, a new misfit functional that takes into account both the zero and non-zero measurements recorded by the receptors and improves the inversion accuracy of atmospheric inverse-source problems is developed and is used in the solution procedure. Several Quasi-Monte Carlo (QMC) point-sets are considered in the stochastic search stage and their performance is evaluated against the conventional Monte Carlo (MC) sampling using the Mersenne–Twister pseudorandom generator. The choice of the descent methods (steepest descent, Newton’s and conjugate gradient methods), stabilizing functional (Tikhonov) and the regularization parameter (α) for gradient optimization were also examined. Gradient descent methods are an attractive choice for the current problem as analytical expressions for the Frechet and Hessian can be pre-computed for the Gaussian plume equation. For the current inverse problem, Newton’s method with adaptive regularization and quadratic line-search is implemented. Since the forward modelling and measurement errors for atmospheric inverse problems are usually unknown, issues concerning ‘model-fit’ and ‘data-fit’ are examined.

As has been the central theme of this discussion, the area of application of inversion techniques to atmospheric source characterization problems is in its nascency and various methods are being tested and their performance is being evaluated. In the work presented in this article, a solution procedure different from the ones published in the literature is outlined. As with most of the other inversion techniques, the speed and accuracy of the present solution methodology depends on the noise level (δ) in the observed data (d_{obs}) and the quality of the forward model (A). When properly formulated, the solution to an inverse problem can help identify the necessary physics that need to be incorporated into A . Thus, inverse problems can in-turn be used to improve the speed and accuracy of the solution to the forward problem by enhancing or pruning the physics in the forward model.

2. Problem definition

In this section, the atmospheric inverse-source problem is defined mathematically.

2.1. The forward problem

The GPM is the simplest model that describes the dispersion of atmospheric contaminants. It is an analytical solution to the simplified advection–diffusion equation [19,23,24]. Of all the models used to characterize atmospheric dispersion, the GPM has the least computational complexity (requires minimum number of arithmetic operations). In emergency-response situations, the two most important factors are the speed and accuracy of reconstruction. The accuracy of reconstruction depends as much on the forward model (A) as it does on the inversion technique. Therefore, within its range of applicability, the GPM is the most desirable in such situations, due to the meagre cost associated with the forward model evaluation. Accordingly, the inverse-source problem is solved using the GPM for continuous point-releases as the forward operator. The GPM for steady, continuous and uniform wind conditions can be written as [23,24],

$$C_i(x_i, y_i, z_i) = \frac{Q_S}{2\pi u_S \sigma_y \sigma_z} \exp\left(\frac{-y^2}{2\sigma_y^2}\right) \left[\exp\left(\frac{-(z_i - z_S)^2}{2\sigma_z^2}\right) + \exp\left(\frac{-(z_i + z_S)^2}{2\sigma_z^2}\right) \right], \quad (2.1)$$

$$\sigma_y = \xi_1 x / \sqrt{1 + 0.0004x}, \quad \sigma_z = \xi_2 x, \quad (2.2)$$

$$x = -(y_R - y_S)\cos(\theta_S) - (x_R - x_S)\sin(\theta_S), \quad (2.3)$$

$$y = -(y_R - y_S)\sin(\theta_S) + (x_R - x_S)\cos(\theta_S). \quad (2.4)$$

Equation (2.1) gives an estimate of the concentration (C_i) at a receptor i with the position vector $\vec{X} = [(x_R - x_i), (y_R - y_i), (z_R - z_i)]$, where, x_S, y_S, z_S , and x_i, y_i, z_i represent the source and the i th receptor spatial coordinates, respectively. The emission rate is Q_S , and the wind speed (u_S), and wind direction (θ_S) are assumed to be constant over the region of interest. The distances $(x_i - x_S)$, $(y_i - y_S)$, and $(z_i - z_S)$ are measured in the along-wind, cross-wind and vertical directions with the origin of the coordinate system being the source location. The parameters σ_y and σ_z (Equation (2.2)) are called the Gaussian plume spread parameters and account for the turbulent diffusion of the plume. They are empirical parameters and are defined for various meteorological stability conditions. For the present problem, Brigg's formulae for Pasquill C-type stability conditions were chosen [23,24]. These parameters, however are terrain and problem dependent and therefore for this work, the dimensionless empirical constants ξ_1 and ξ_2 , which in Brigg's formulae are 0.22 and 0.20, were replaced by 0.12 and 0.10 for TCTE [15] as per the work of [9]. There are several other assumptions that are tacit in the Gaussian dispersion equation for which the reader may refer to [23,24].

It should be realized that the GPM is not a 'building-aware' model, in that it does not account for the changes in flow and dispersion patterns caused by buildings and other roughness elements when estimating the concentration value at a receptor in an urban domain. Therefore, depending on the terrain, the GPM may or may not be accurate in the near-field of a point source. In the far-field, since the plume is transported in the mesoscale wind direction, the constant wind direction assumption in the GPM becomes more admissible [25]. The solution methodology that will be developed in the subsequent sections is independent of the forward model used. The solution procedure developed can be applied with other versions of the GPM, or forward models that solve the governing equations for

fluid flow and dispersion [26]. It should however be noted that depending on the forward model used, the performance of the proposed solution procedure will vary.

The forward problem can be defined as estimating the concentrations at the desired receptor locations based on the given model (source) parameters (m) and can be written as

$$A(m) = d. \quad (2.5)$$

Here, A is the forward modelling operator (which in this case is the GPM), m is the set of model or source parameters and d is the vector of concentration measurements at the various receptor locations. For the computation of the concentration values at any point downwind of the source, the GPM requires eight model parameters (m_{GPM}). Hence, when using the GPM as the forward model, (2.5) can be written as

$$A(m_{\text{GPM}}) = d, \quad (2.6)$$

$$m_{\text{GPM}} = [x_S \ y_S \ z_S \ Q_S \ u_S \ \theta_S \ \xi_1 \ \xi_2]_{8 \times 1}^T, \quad (2.7)$$

$$d = [d_1 \ d_2 \ \dots \ d_N]_{N \times 1}^T. \quad (2.8)$$

2.2. The inverse problem

The inverse problem can be defined as the solution of the operator equation,

$$d = A(m). \quad (2.9)$$

The solution to the inverse problem requires determining such a model m_{pr} (predicted model) that generates predicted data, d_{pr} , which ‘fits-well’ the observed data d_{obs} [1]. If the forward operator is nonlinear, the solution to the inverse problem can only be found iteratively. Therefore, nonlinear inverse problems are often cast as minimization or optimization problems as shown below:

$$\arg\left(\min_{m_{\text{pr}}} \|A(m_{\text{pr}}) - d_{\text{obs}}\|_2\right). \quad (2.10)$$

From (2.1) and (2.7), it can be deduced that when solving the source-inversion problem using the GPM, at most eight model parameters can be retrieved (m_{GPM}). Of these eight parameters, since the source strength (Q_S) and the wind velocity at the source (u_S) are a fraction of each other in the Gaussian equation (Equation (2.1)), attempting to retrieve them individually can result in non-unique solutions for these parameters. Therefore, they were combined into a single term (Q_S/u_S) in the present solution procedure.

The following five ($m_{\text{STOCH+GD}}$) of the eight model parameters (m_{GPM}) (Equation (2.7)) in the GPM (Q_S and u_S combined into a single term (Q_S/u_S)) are retrieved in this work for TCTE:

$$m_{\text{STOCH+GD}} = [x_S \ y_S \ z_S \ Q_S/u_S \ \theta_S]_{5 \times 1}^T. \quad (2.11)$$

Hence, the inverse-source problem is a five-dimensional (5D) inverse problem. The rationale behind retrieving five model parameters is based on the relationship between the increasing nonlinearity of inversion and the number of model parameters to be retrieved.

With the GPM, if only Q_S or u_S are to be retrieved, the inverse problem is in fact linear (Equation (2.1)). Nonlinearity creeps into the GPM from the remaining six model parameters. It is also well-accepted that an increase in the number of unknown model parameters leads to greater correlation between the model parameters, thereby resulting in non-unique solutions. The simple analytical nature of the Gaussian dispersion equation therefore raises the important question of the number of model parameters that one would want to retrieve (ideally eight) versus the accuracy of inversion. Non-uniqueness in inverse problems may be mitigated by including any prior information (m_{apr}) about the parameter values. But including prior information can compromise the robustness of the inversion technique as it can be inaccurate for a certain source release scenario. Hence, when using a simple analytic forward model such as the GPM for inversion, the question of number of retrievable model parameters should be addressed *a priori*. Therefore, in this work, five model parameters are retrieved (Equation (2.11)). The stochastic search stage is implemented with broad bounds on the model parameter values and unconstrained gradient optimization is performed with the initial iterate provided by the stochastic search stage.

3. The Copenhagen tracer experiments

In this work, data from the Copenhagen field experiments [15] is used to explain and validate the proposed solution procedure. The dataset used from the Copenhagen experiments is briefly described in this section.

As part of the Copenhagen experiment, the tracer sulphurhexafluoride (SF_6) was released without buoyancy from a tower of height 115 m. It was collected 2–3 m above the ground-level by sensors placed in three crosswind arcs positioned 2–6 km from the point of release. The first (Arc 1), second (Arc 2) and third (Arc 3) arcs were at radial distances of 2, 4 and 6 km from the source. The receptor locations and the source release location are shown in Figure 1. A total of 40 tracer-samplers were used with 15 sensors placed in Arc 1, 12 in Arc 2 and 13 in Arc 3. Three consecutive 20-min averaged tracer concentrations were measured, allowing for a total sampling time of 1 h. The site was mainly residential having a roughness length (z_0) of 0.6 m. The experiments were conducted on different days under neutral and unstable meteorological stability conditions. For this work, the experiment conducted on 19 October 1978/1979 is considered. The experiment was conducted mid-day, thereby resulting in unstable meteorological conditions (Monin–Obukhov length $L \sim -108$ m, friction velocity $u_* \sim 0.39$ m s⁻¹, inversion height ~ 1120 m, standard deviation of the lateral and vertical velocities at the release point $\sigma_v \sim 0.85$ m s⁻¹ and $\sigma_w \sim 0.68$ m s⁻¹, stability class = Pasquill C-type) The emission rate was 3.2 g s⁻¹ and the limit of estimation (LOE) of the sensors was 9 ng m⁻³. In the Copenhagen dataset [15], the mean value of the three consecutive 20-min averaged concentration datasets for the experiment conducted on 19 October is provided. In this work, this dataset is used as the observed data for inversion. The minimum positive concentration in the observed data vector from TCTE is 6 ng m⁻³. Therefore for inversion, the value of LOE is set to 6 ng m⁻³ instead of 9 ng m⁻³. The average temperature (t_S), wind speed (u_S) and direction (θ_S) at the release height during the course of the experiment were $t_S \sim 283.72$ K, $u_S \sim 4.92$ m s⁻¹ and $\theta_S \sim 308.6^\circ$. For the validation of the proposed inversion technique, the height of the sensors is considered to be 2.5 m.

It is worth noting that for the 19 October experiment, 34 out of the 40 sensors recorded positive concentrations (received a hit). These have been denoted by the ‘squares’ (□)

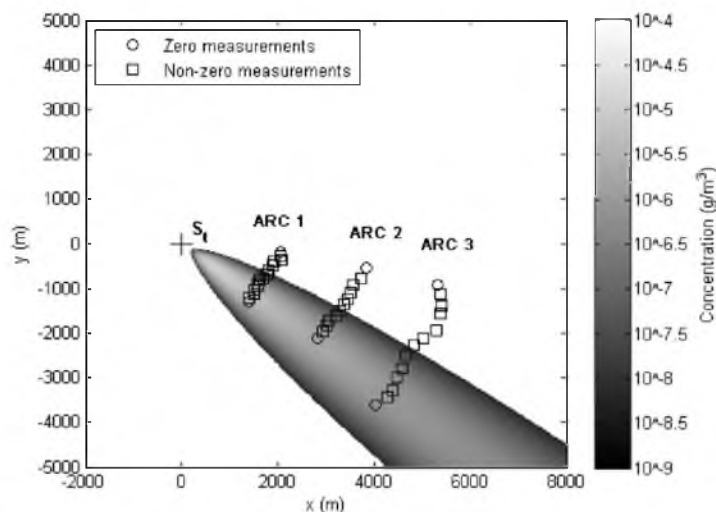


Figure 1. Schematic depicting the sensor positioning and the number of non-zero (\square) and zero (\circ) measurements recorded for TCTE on 19 October. Also shown is the plume spread predicted by the GPM for true source parameters (m_i). ' S_i ' is the true source location.

in Figure 1. As stated in Section 1, the total error that needs to be accounted for during the estimation stage is the sum of the following individual error components:

$$\begin{aligned} \text{Estimation error } (\delta_E) = & \text{forward modelling error } (\delta_{FM}) \\ & + \text{measurement error } (\delta_M). \end{aligned} \quad (3.1)$$

Since the authors of the report [15] make no mention of the uncertainties in the measurements, δ_M is assumed to be zero (i.e. $\delta_E = \delta_{FM}$). The rationale behind setting $\delta_M = 0$ lies in the definition of the LOE in atmospheric source-inversion problems. For instance, assuming 5% noise in the observed data can result in certain non-zero measurements going below the LOE, thereby becoming zero. Since the locations of zero and non-zero measurements are of paramount importance for source characterization, the measurements were not tampered with by assuming noise levels. In order to get a feel for δ_{FM} when using the GPM, the forward problem was solved with the known source parameters, with $\xi_1 \approx 0.12$ and $\xi_2 \approx 0.1$ (from the work of [9]). The results obtained are shown in Figure 1. From the figure it is evident that despite using the modified σ_y and σ_z values, the plume spread predicted by the GPM does not match the experimental measurements.

The difference in the plume spread predicted by the GPM can be attributed to the complexities associated with real-world flows that are incorporated into the present version of the GPM. Since $\delta_E = \delta_{FM}$, and δ_{FM} is due to the inadequacies of the forward model and cannot be quantified, the inversion procedure developed (and described in subsequent sections) is designed to drive the forward model to match the zero and non-zero measurements recorded by the sensors. That is, the inversion procedure developed ensures that at the end of inversion, the plume spread predicted by the GPM is as close as possible to that observed in the experiments, not in terms of magnitudes of

concentration measurements, but in terms of the zero and non-zero measurements recorded by the respective sensors.

Definition 1 Whenever the predicted model parameters generate non-zero (\geq LOE) predicted data at a receptor that recorded a non-zero concentration (\geq LOE), or zero ($<$ LOE) predicted data at a receptor that recorded a zero concentration value ($<$ LOE), it will from hereon be said that the predicted model parameters ‘satisfy’ the concentration measurement at the receptor location.

The true model parameters (m_t) for TCTE are shown in Equation (3.2). The bounds of the model parameter space considered during inversion are shown in Equation (3.3).

$$\begin{aligned} m_t &= [x_S(m) \quad y_S(m) \quad z_S(m) \quad Q_S/u_S(g/m) \quad \theta_S(^{\circ})]_{5 \times 1}^T \\ &= [0 \quad 0 \quad 115 \quad 0.65 \quad 308.6]_{5 \times 1}^T, \end{aligned} \quad (3.2)$$

$$x_S \in [-2000, 8000], \quad y_S \in [-5000, 5000], \quad z_S \in [0, 200], \quad Q_S/u_S \in [0, 1], \quad \theta_S \in [0, 360]. \quad (3.3)$$

4. Solution procedure

4.1. The Tikhonov parametric functional

In this work, the atmospheric inverse-source problem is solved using a combination of stochastic search and regularized gradient optimization methods. Regularization provides a mechanism by which any prior information can be included in the inversion procedure. Including prior information can help improve the stability of inversion. The regularized solution of an inverse problem can be obtained by minimizing the unconstrained parametric functional shown in Equation (4.1).

$$P(m, d, \alpha) = \mu_D(A(m), d) + \alpha s(m), \quad (4.1)$$

$$\arg\left(\min_m P(m, d, \alpha)\right). \quad (4.2)$$

In Equation (4.1), $\mu_D(A(m), d)$ is the misfit functional (over the data space (D)), $s(m)$ is the stabilizing functional and $P(m, d, \alpha)$ is the parametric functional. The parametric functional is a linear combination of the misfit and the stabilizing functionals, and the parameter α is called the regularization parameter.

The role of the misfit functional is to check if, on every step of inversion, the discrepancy between the observed and the predicted data is increasing or decreasing. Since most real-life inverse problems are ill-posed, casting the inverse problem as the minimization of the misfit functional can result in unstable solutions. This is because the operator A^{-1} may not be continuous (may not exist) over the entire model space (M). The inherent ill-posedness of inverse problems can be overcome by considering a family of well-posed problems ($d = A_{\alpha}(m)$) that approximate the original ill-posed problem ($d = A(m)$). The scalar parameter $\alpha > 0$ in the above expression is called the regularization parameter and regularization is imposed under the constraint $m_{\alpha} \rightarrow m_T$; as $\alpha \rightarrow 0$

(where m_T is the true solution). That is, regularization approximates the non-continuous operator A^{-1} by the family of continuous operators $A_\alpha^{-1}(d)$ for different values of α . The family of continuous $A_\alpha^{-1}(d)$ operators that approximate the original non-continuous operator A^{-1} are called the regularization operators $R_\alpha(R(d, \alpha) = A_\alpha^{-1}(d))$. Regularization operators can be constructed by adding a stabilizing functional to the misfit functional. The task of the stabilizing functional is to help identify from the set of all possible models that fit the data, a solution that belongs to the correctness-set $M_C(M_C \subset M)$, such that the operator A^{-1} is continuous over M_C . Formulating an inverse problem in this manner converts an ill-posed problem into a ‘conditionally well-posed problem’, expressed by the parametric functional in Equation (4.1)

In this article, Equation (4.1) is minimized using Newton’s method. Gradient methods require the misfit functional to be convex, continuous and differentiable (C-C-D) to converge to the global minimum. Examining the GPM, one can recognize that the misfit functional generated by the GPM (using Equation (4.4)) has multiple critical points (maxima, minima and saddle points). In fact, when using the GPM, the number of maxima in the misfit functional space is a function of the domain size, the wind direction at the source (θ_S) and the number of sensors (N) in the domain. This can be shown by considering the GPM in Equation (2.1). For instance, if in Equations (2.1)–(2.4), $x_S = x_i$, $y_S = y_i$, and $z_S = z_i$, then, in (2.1), $C_i(x_i, y_i, z_i) = NaN (= 0/0)$. If x_i , y_i and z_i , approach x_S , y_S and z_S at the same rate, for some fixed θ_S , the predicted concentration in (2.1) approaches infinity.

Thus, it is seen that when using the GPM, whenever the predicted source location is close to any of the receptor locations, there is an increase in the misfit functional value. The presence of the various maxima in addition to the various error components (δ_E and δ_A) results in the formation of several critical points interspersed around the global minimum. Therefore, to employ gradient schemes to solve such problems, a good starting solution is pivotal. The starting solution needs to be in the C-C-D region surrounding the global minimum in the misfit functional space. For this reason, the approach proposed in this article is comprised of stochastic search to provide a good initial iterate to the gradient descent scheme (that may be in the C-C-D region).

In order to illustrate that the proposed approach works for inverse-source problems with the GPM as the forward operator, the domain of TCTE (Figure 1) was discretized and the misfit functional at every grid node was computed using Equation (4.4). This was done in two-dimensions (2D) by considering the x and y coordinates of the source (x_S and y_S) to be the unknown model parameters (m). The results obtained are shown in Figure 2(a) and (b). From the figures it can be seen that as $x_S \rightarrow x_i$ and $y_S \rightarrow y_i$, $|(d_{\text{obs}})_i - (d_{\text{pr}})_i| \uparrow$ (increases). This behaviour is in agreement with the previously stated assertion that as $x_S \rightarrow x_i$ and $y_S \rightarrow y_i$, $C_i(x_i, y_i, z_i) = (d_{\text{pr}})_i \rightarrow \infty$. From the figures it can also be deduced that there exists a region in the misfit functional space in which the misfit functional appears to be convex and continuous, and houses the global minimum. The plots also shed light on the distortion of the misfit functional by the forward modelling error δ_{FM} (assuming $\delta_{\text{M}} = 0$). The distortion manifests itself in terms of the discrepancy observed in the predicted S_p (square – ■) and the true source locations S_i (hexagon – ★) as shown in Figure 2(b). However, not too many conclusions should be drawn from these plots as they are in 2D. In 5D, the hyper-volume that spans the C-C-D region might be of different size and corrugated, due to the effects of nonlinear error propagation.

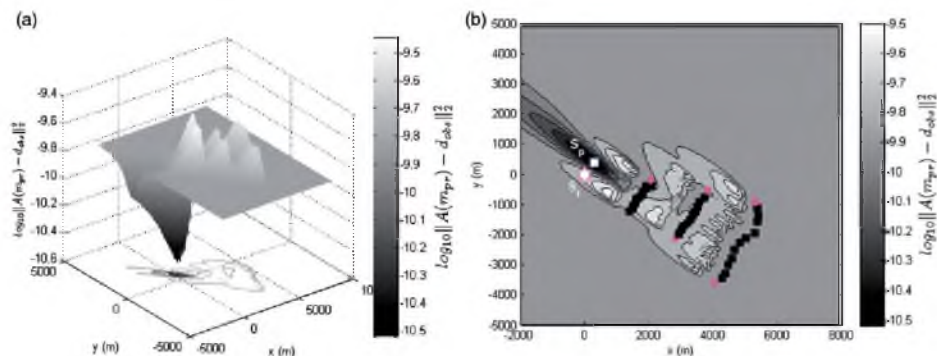


Figure 2. (a) Surface of the misfit functional for TCTE, (b) 2D contour of the misfit functional for TCTE data with the true (S_t) and predicted (S_p) source locations.

4.2. The misfit functional

The definition of the misfit functional is one of the most important components of an inverse problem. When properly formulated, it guides the inversion algorithm to the global minimum. Misfit functional formulation, just like the choice of an inversion algorithm, is highly problem dependent. Some of the popular formulations of misfit functionals are based on the L_1 - and L_2 -norms of the misfit (Equations (4.3) and (4.4)), the L_1 - and L_2 -norms of the relative misfit, the Kullback–Leibler information divergence functional (Equation (4.5)) and the negative Poisson log-likelihood functional (Equation (4.6)) [27,28].

$$\mu_{L_1}(A(m_{pr}), d_{obs}) = \|A(m_{pr}) - d_{obs}\|_1, \quad (4.3)$$

$$\mu_{L_2}(A(m_{pr}), d_{obs}) = \|A(m_{pr}) - d_{obs}\|_2, \quad (4.4)$$

$$\mu_{KL}(A(m_{pr}), d_{obs}) = \langle A(m_{pr}), \log(A(m_{pr})/d_{obs}) \rangle, \quad (4.5)$$

$$\mu_{LHD}(A(m_{pr}), d_{obs}) = \langle A(m_{pr}), 1 \rangle - \langle d_{obs}, \log(A(m_{pr})) \rangle. \quad (4.6)$$

Computing the L_2 -norm or the L_1 -norm of the misfit to determine the class of models (m_{pr}) that fit the observed data (d_{obs}) can lead to erroneous results for the atmospheric source-inversion problem. This is primarily because atmospheric inverse-source problems suffer from sparse number of measurements (N) in general, and very few non-zero measurements (N_{NZ}) in particular. Therefore, computation of the L_1 - or L_2 -norms (Equations (4.3) and (4.4)) does not take into account the zero-measurements recorded by the sensors, as the magnitude of these norms are driven only by the non-zero measurements. Also, since the observed and predicted data vectors in atmospheric inverse-source problems consist of concentration values of varying orders of magnitudes, the larger components of the observed and predicted data vectors suppress the effect of the smaller components in the computed value of the norm of the residuals.

To mitigate the above-mentioned problems, one can use an appropriate data-weighting matrix such that the significance of the individual components of the predicted and observed data vectors is preserved during inversion. In this article, an even simpler approach (misfit functional) is proposed and is described in the following paragraphs.

Our new misfit functional takes into account zero and non-zero measurements in the observed and predicted data vectors and treats both of them equally. The new functional uses the base 10 logarithm of the ratio of the observed (d_{obs}) and predicted data (d_{pr}), and is shown in Equation (4.7). In Equation (4.7), $I\{\}$ is the indicator function, and is defined in Equation (4.8). The positive constant ε ($\varepsilon \ll \text{LOE}$) accounts for the zero measurements and becomes insignificant for non-zero measurements. For the present work, ε value was set to 10^{-16} .

$$\mu_D(d_{\text{obs}}, d_{\text{pr}}) = \left(\sum_{i=1}^N I \left\{ \left(\log_{10} \left[\frac{(d_{\text{obs}})_i + \varepsilon}{(d_{\text{pr}})_i + \varepsilon} \right] \right) \in \Omega \right\} \right)^{-1}, \quad (4.7)$$

$$\begin{aligned} \Omega &= [\beta_{\text{LB-STOCH}}, \beta_{\text{UB-STOCH}}] \\ I_{\Omega}(x) &= \begin{cases} 1, & \text{if } x \in \Omega, \\ 0, & \text{if } x \notin \Omega. \end{cases} \end{aligned} \quad (4.8)$$

The applicability of the proposed misfit functional is based on the fact that for inversion without noise, the end result of inversion should give predicted model parameters (m_{pr}), such that for $m_{\text{pr}} \approx m_i$, $((d_{\text{obs}})_i + \varepsilon) / ((d_{\text{pr}})_i + \varepsilon) \approx 1$, $\forall i$. The bounds $\beta_{\text{LB-STOCH}}$ and $\beta_{\text{UB-STOCH}}$ are the lower and upper bounds (data-fit criteria) of the stochastic search stage and depend upon the noise level (δ_{M}) in the observed data (d_{obs}), the forward modelling error (δ_{FM}) and the accuracy to which one wants to implement the search stage. Depending on the values of $\beta_{\text{LB-STOCH}}$ and $\beta_{\text{UB-STOCH}}$, the search stage can either be computationally exorbitant or inexpensive. Strategies to solve the inverse-source problem in general, and to compute the bounds $\beta_{\text{LB-STOCH}}$ and $\beta_{\text{UB-STOCH}}$ in particular are described in the subsequent sections.

The new misfit functional is used in the stochastic search stage to identify a good starting solution for the gradient descent scheme. It should be noted that the starting solution (m_{STOCH}) is a function of the values of $\beta_{\text{LB-STOCH}}$ and $\beta_{\text{UB-STOCH}}$, and the values of $\beta_{\text{LB-STOCH}}$ and $\beta_{\text{UB-STOCH}}$ characterize the size of the hyper-volume constituting the C-C-D region (based on L_2 -norm) around the global minimum in the misfit functional space. Due to this, care should be taken in the selection of $\beta_{\text{LB-STOCH}}$ and $\beta_{\text{UB-STOCH}}$ values, since large values of these parameters may no longer provide an initial iterate (m_{STOCH}) in the C-C-D region surrounding the global minimum for problems with misfit functional spaces comprising several critical points. Since gradient methods only work with continuous and differentiable misfit functionals, the conventional misfit functional based on L_2 -norm (Equation (4.4)) is used for computing the new iterates for the gradient scheme.

4.3. Strategies for solving the atmospheric source-inversion problem

In this section, strategies for solving the atmospheric source characterization problem in general and computing the bounds $\beta_{\text{LB-STOCH}}$ and $\beta_{\text{UB-STOCH}}$ in particular are discussed.

Three strategies are proposed to solve the inverse-source problem. They are described in the following sections:

4.3.1. *Rigorous strategy*

The objective of this strategy is to ‘satisfy’ (Definition 1) all the sensor measurements (N). This is the preferred strategy for evaluating atmospheric dispersion models (forward models) using field experiment data. The same approach can be adopted to solve inverse-source problems using the forward model (dispersion model). In spite of being the most rigorous method to solve such problems, this approach cannot be implemented for all real-life atmospheric dispersion situations and for increasing number of sensor measurements (N). This is because, the effects of myriads of real-world processes are not captured in totality by the existing forward dispersion models (A) in general, and the GPM in particular. Since in this article, field experiment data (TCTE) are used to retrieve the model parameters ($m_{\text{STOCH+GD}}$), the rigorous strategy is not adopted. However, 10^8 MC simulations (points) with the semi-rigorous strategy described in Section 4.3.2.1 and with $\beta_{\text{LB-STOCH}}$ and $\beta_{\text{UB-STOCH}}$ values prescribed in Section 4.4 were run to illustrate that in spite of running an astronomical number of MC simulations, all the sensor measurements for TCTE cannot be satisfied. For the final model parameters obtained (m_{STOCH}), the maximum number of sensor measurements ($N_{\text{max-S}}$) satisfied were 39 out of the available 40 measurements, and out of the 10^8 random samples (model parameter vectors) only four model parameters satisfied 39 measurements.

4.3.2. *Semi-rigorous strategy*

The objective of this strategy is to satisfy most, but not all the sensor measurements (N). The number of sensor measurements that should be satisfied (N_S), or the percentage of the total number of measurements (N) that should be satisfied ($\lambda_N = 100 \times N_S/N$) for the predicted solution to be in the vicinity of the true solution is problem-specific, and depends upon the number of available sensor measurements (N), the number of model parameters to be retrieved (N_m), and the quality of the forward model (A). While λ_N values close to 100% make the stochastic search stage computationally intensive, relaxed values of λ_N might produce initial iterates that do not belong to the C-C-D region surrounding the global minimum.

It should be noted that while solving inverse-source problems, fixing values of N_S might result in erroneous source locations. This is because the inversion algorithm might end up not accounting for either only the zero or non-zero measurements to satisfy the λ_N value assigned. To avoid such pitfalls, if N_{NZ} and N_Z represent the number of zero and non-zero measurements recorded ($N_{\text{NZ}} + N_Z = N$), it is suggested that N_S should be divided into its individual components based on the number of zero ($N_{\text{S-Z}}$) and non-zero ($N_{\text{S-NZ}}$) measurements ($N_S = N_{\text{S-Z}} + N_{\text{S-NZ}}$) that should be satisfied. Assigning λ_N values based on the percentage of zero ($\lambda_Z = 100 \times N_{\text{S-Z}}/N_Z$) and non-zero ($\lambda_{\text{NZ}} = 100 \times N_{\text{S-NZ}}/N_{\text{NZ}}$) measurements should (will) improve the accuracy of the inverse problem solution. Based on how the λ_N values are determined, the semi-rigorous strategy can be implemented in three ways, which are as given in the following sections.

4.3.2.1 *Semi-rigorous strategy 1 (SR1)*. SR1 comprises satisfying λ_N measurements without assigning individual values for λ_{NZ} and λ_Z . It is the least robust of all the

semi-rigorous strategies and produces initial iterates in the C-C-D region only for large values of λ_N . To get an idea about the minimum λ_N value for the TCTE that makes the solution procedure fail-safe, the MC simulations used to compute $N_{\max-S}$ were utilized. From the simulations it was deduced that for making the stochastic search stage fail-safe (i.e. generate initial iterates in the C-C-D region), at least 37 sensors (92.5% of the observed data) had to be satisfied. To evaluate the performance of the various QMC point-sets, the number of MC and QMC points required for satisfying $N_S = 37, 38$ and 39 sensors are compared in this article (discussed in section 5.2).

4.3.2.2 *Semi-rigorous strategy 2 (SR2)*. SR2 comprises assigning individual values for λ_{NZ} and λ_Z . For the TCTE, based on the 10^8 MC simulations, the following details were observed: (1) if all the zero measurements are satisfied ($N_{S-Z} = 6$), the minimum number of non-zero measurements that need to be satisfied to make the solution procedure fail-safe is $N_{S-NZ} \geq 27$, (2) if $N_{S-Z} = 5$, then $N_{S-NZ} \geq 31$ and (3) for $1 \leq N_{S-Z} \leq 4$, $N_{S-NZ} \geq 33$. These details are illustrated in Figure 3. The benefit of assigning individual values for λ_{NZ} and λ_Z is that the value of N_S required for identification of an initial iterate can be brought down. That is, if all six zero measurements are satisfied, then the minimum number of non-zero measurements that need to be satisfied is 27, which makes $N_S \geq 33$ ($N_S \geq 37$ for SR1 for the solution procedure to be fail-safe). In this article, for conciseness, the results for SR2 are not presented.

4.3.2.3 *Semi-rigorous strategy 3 (SR3)*. In SR3, all non-zero measurements must be satisfied. The number of zero measurements that should be satisfied is problem dependent. The rationale behind setting $\lambda_{NZ} = 100\%$ is based on the idea that over-prediction is always better than under-prediction. Setting $\lambda_{NZ} = 100\%$ and $\lambda_Z \leq 100\%$ implies over-predicting the extent of the plume spread, which implies over-predicting the

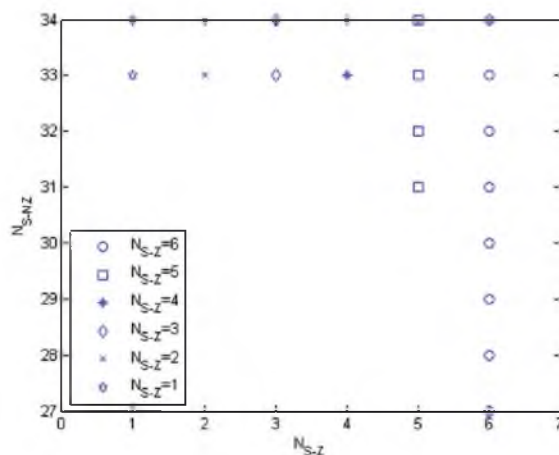


Figure 3. The number of zero (N_{S-Z}) and non-zero (N_{S-NZ}) measurements that should be satisfied to obtain initial iterates in the C-C-D region for TCTE. The details of this figure are highly problem-dependent. They also depend on the plume spread parameters chosen.

source strength. This is the preferred approach in atmospheric dispersion problems as over-prediction implies a higher factor of safety. For evaluating the performance of the various QMC point-sets, results for the cases when $N_{S-Z} \geq 1, 2, 3, 4$ and 5 are reported (in Section 5.2).

4.4. Computing the bounds $\beta_{LB-STOCH}$ and $\beta_{UB-STOCH}$

The two scenarios that should be avoided when solving the inverse-source problem are:

- (1) predicting non-zero concentrations at sensors that recorded zero measurements, and
- (2) predicting zero concentrations at non-zero sensor locations. Whenever these scenarios occur, the stochastic search algorithm must be able to identify them and reject the generated (predicted) model parameters (m_{pr}). The two scenarios mentioned help compute the bounds for the stochastic search stage. The method for computing the bounds is described below.

Case 1

$$(d_{obs})_i = 0, \quad (A(m_{pr}))_i \neq 0$$

At a sensor location where the observed data is zero (< 6 ng), the predicted data can take either a zero (< 6 ng) or a non-zero value (≥ 6 ng). The smallest non-zero value that $(d_{pr})_i$ can take so that the definition of LOE is preserved is 6×10^{-9} g (= LOE (=6 ng)). From this, $\beta_{LB-STOCH}$ can be estimated as

$$\beta_{LB-STOCH} \approx \log_{10}[\varepsilon/LOE] \approx \log_{10}[10^{-16}/6 \times 10^{-9}] \approx -7.78. \quad (4.9)$$

Case 2

$$(d_{obs})_i \neq 0, \quad (A(m_{pr}))_i = 0$$

Predicted data values of zero can occur at receptor locations with non-zero measured values. If zero concentration is predicted at the receptor that recorded the maximum concentration, it is more likely that the predicted model parameters (m_{pr}) that generated the predicted data (d_{pr}) are incorrect. The likelihood of the predicted model parameters being close to the true model parameter is higher if $(d_{pr})_i = 0$ occurs at the receptor that recorded the minimum concentration value. Since the noise level in the data is unknown, the smallest non-zero value that the observed data vector (d_{obs}) can take is 6 ng. Hence, $\beta_{UB-STOCH}$ can be estimated as

$$\beta_{UB-STOCH} \approx \log_{10}[LOE/\varepsilon] \approx \log_{10}[6 \times 10^{-9}/10^{-16}] \approx 7.78. \quad (4.10)$$

Based on the values of $\beta_{LB-STOCH}$ and $\beta_{UB-STOCH}$ derived, it can be seen that the semi-rigorous strategy allows for considerable over- and under-prediction of the concentrations at the receptors.

4.5. MC and QMC sampling

QMC point-sets and MC sampling are considered in the stochastic search stage. QMC sampling is recommended over the conventional MC sampling as quasi-random numbers

were developed to fill an s -dimensional hyper-cube on $[0, 1]^s$ more uniformly than pseudorandom numbers [29]. Additionally, QMC point-sets provide the extra advantage of being completely deterministic. This property of QMC point-sets is highly desirable for atmospheric event reconstruction problems. This is because, for known receptor locations, stochastic algorithms developed to solve the inverse-source problem for a real city can be tested for a large set of possible model parameter values, and the performance of the algorithm in terms of total execution time (which is equivalent to the number of forward model evaluations) can be determined *a priori*.

QMC sampling is performed using the Halton, Hammersley, Sobol, SpecialNeiderreiter and NeiderreiterXing point-sets [29,30], in their original and scrambled forms. The scrambled versions of the Halton, Hammersley, SpecialNeiderreiter, and NeiderreiterXing point-sets were obtained by applying Faure permutations over the original set [29]. The scrambled version of the Sobol point-set was obtained by applying the scrambling procedure described in [31], a random linear scramble combined with a random digital shift.

For comparing the performance of the various QMC point-sets with the Mersenne-Twister pseudorandom generator, the expected number of MC points $E(\text{MC})$ required for satisfying a given set of sensor measurements were used. The quantity $E(\text{MC})$ was computed from the 10^8 MC simulations run to compute $N_{\text{max-s}}$. Leaving the Hammersley point-set, the i th components of all other QMC point-sets considered are independent of the number of points generated ($n: n \geq i$). This is because, only in the Hammersley point-set, the first dimension is a regular one-dimensional (1D) lattice evenly distributed on the interval $[0, 1]$. Therefore for accurate comparison of the performance of the Hammersley point-set with the pseudorandom generator, $E(\text{MC})$ number of Hammersley points were generated to satisfy $N_s = k$ measurements.

4.6. The stabilizing functional, regularization parameter and gradient methods

The stabilizing functional $s(m)$ in conjunction with the regularization parameter α is used to construct the regularization operator R_α that converts an ill-posed problem into a ‘conditionally-well-posed’ problem (Equation (4.1)). For the inverse-source problem, the standard Tikhonov stabilizing functional was chosen as the stabilizing functional. The Tikhonov stabilizer is shown in Equation (4.11). The vector m_{apr} represents some prior information that we might have about the model parameters (m). No prior information was assumed in the solution procedure for the atmospheric event reconstruction problem. However, a modified version of the stabilizer shown in Equation (4.11) was used in the descent algorithm and is shown in Equation (4.12). The rationale behind using this stabilizer is based on the initial iterate provided by the stochastic search stage. The stochastic search stage was designed to provide a starting solution that belongs to the C-C-D hyper-volume around the global minimum. Therefore, to ensure that the gradient scheme does not bounce out of the C-C-D region, the model parameters on the current (j) and previous iterations ($j-1$) were used to stabilize the gradient scheme.

$$s(m) = \|m - m_{\text{apr}}\|_2^2, \quad (4.11)$$

$$s(m) = \|m^j - m^{j-1}\|_2^2, \quad j = 2, 3, \dots \quad (4.12)$$

The regularization parameter α determines the relative significance of the misfit and the stabilizing functionals. Choosing extremely small values of α leads to the situation where the inverse problem reduces to the minimization of the misfit functional, which can result in unstable solutions. Large values of α correspond to the situation where the inverse problem is driven in the direction of the stabilizer. Hence, accurate reconstruction requires optimal regularization parameter selection. Several methods have been proposed for optimal regularization parameter selection. Prominent among these are the Morozov condition [28] and the L-curve criterion [1,27,28,32]. In this article, a more heuristic approach as suggested in [1] was adopted. The regularization parameter was estimated following Equations (4.13) and (4.14). The first iteration of the gradient scheme is run without regularization and α^1 is calculated at the end of the iteration following Equation (4.13). Values of α on the subsequent iterations are computed using (4.13). In Equation (4.14), the scalar q helps control the extent of regularization. Lower values of q favour faster convergence, but can lead to instabilities in the inversion procedure. Higher values of q promote better stability, but result in more iterations for convergence. In this work, the initial value of q was set to 0.7 and was decreased by raising it to the power of the previous iteration number ($j-1$) as shown in Equation (4.14).

$$\alpha^1 = \|A(m^1) - d_{\text{obs}}\|_2^2 / \|m^1 - m^0\|_2^2, \quad (4.13)$$

$$\alpha^j = \alpha^1 q^{j-1}, \quad (0 < q < 1), \quad j = 2, 3, \dots \quad (4.14)$$

Following Equations (4.4) and (4.12)–(4.14), the unconstrained parametric functional described in Equation (4.1) can be written as

$$P^j(m^j, d_{\text{obs}}, \alpha^j) = \|A(m^j) - d_{\text{obs}}\|_2^2 + \alpha^j \|m^j - m^{j-1}\|_2^2. \quad (4.15)$$

The parametric functional shown in Equation (4.15) is minimized using Newton's method. To ensure convergence and to prevent overshooting of the Newton jump, quadratic line-search was implemented. For computational efficiency, the Hessian is approximated by calculating the residual assuming unit-step with linear line-search. Additional details of the algorithm implemented can be found in [1].

4.7. The hybrid algorithm conundrum

Hybrid algorithms are an attractive choice for solving optimization problems as they can help increase the speed of convergence of the algorithm. It is for this reason that they have been used extensively in several problems from diverse fields and also in problems involving atmospheric source characterization [18,20,33]. The solution procedure described in this article is also a hybrid approach comprising stochastic search and gradient optimization, with different misfit functionals implemented in each stage. The stochastic search stage can be regarded as a crude maximization stage (because the likelihood of the initial iterate being close to the true source parameters increases with increasing N_S values), and the gradient descent stage can be regarded as the minimization stage (the residual of the observed and predicted data is minimized). The predicament arises when model parameters that maximize the number of sensors satisfied are different from model parameters that minimize the residual. This situation arises in real-life problems as the estimation error (Equation (3.1)) that needs to be accounted for is unknown. If the stochastic search stage is implemented with tight error bounds

Table 2. Computed inversion model parameters for TCTE.

Model parameters	x_S (m)	y_S (m)	z_S (m)	Q_S/u_S (gm^{-1})	θ_S (degrees)	N_S
m_t	0	0	115	0.64	308.57	–
m_{STOCH}	–650.81	736.72	3.08	0.73	297.22	37
$m_{\text{STOCH}*\text{max}(N_S)}$	91.05	–21.44	85.97	0.86	294.63	39
$m_{\text{STOCH}+\text{GD}}$	–339.78	73.6	193.42	1.06	291.73	34

(for safety), and if the model parameters obtained from this stage (m_{STOCH}) satisfy $N_{\text{STOCH}} \leq N$ sensors, and if the model parameters computed by the gradient scheme ($m_{\text{STOCH}+\text{GD}}$) (using m_{STOCH}) are closer to the true model parameters (m_t), but satisfy lesser number of sensor measurements ($N_{\text{STOCH}+\text{GD}}$) than N_{STOCH} , then the question of which model parameters to believe more emerges. That is, if $N_{\text{STOCH}+\text{GD}} < N_{\text{STOCH}}$, but $\|m_{\text{STOCH}+\text{GD}} - m_t\| < \|m_{\text{STOCH}} - m_t\|$, in a real-time situation, should one go with m_{STOCH} or $m_{\text{STOCH}+\text{GD}}$? When using field experiment data to evaluate hybrid algorithms, since m_t is known *a priori*, the decision is relatively easy to make. However, in real-time, where m_t is unknown, then the question becomes: should one choose the model parameters that give the best ‘data-fit’ or ‘model-fit’? Therefore, in this article, when the Mersenne–Twister generator is used, model parameters that produce the maximum N_S value, as well as the minimum residual, are presented (Section 5.1, Table 2).

4.8. Implementing the proposed approach

Almost all algorithms developed to solve inverse problems either have tuning parameters or parameters that require a good initial value or distribution. The approach proposed in this article is no different in that it also requires the specification of the parameter (λ) for its successful implementation. It should be realized that one might get away by considering the misfit functional based on the L_2 -norm in the stochastic stage for some source-receptor configurations, and hence circumvent the need for the specification of a λ value, making the solution procedure free of tuning parameters (the convergence criterion for the L_2 -norm can be deduced from the available data). However, a new misfit functional, and thereby the λ value were introduced only to make the solution procedure fail-safe. Since the optimum λ value is never available in real-life situations, it is recommended that the proposed approach be implemented with large λ values (using SR1, SR2 or SR3), or, implemented multiple times starting with λ values of 90% (for SR1: $\lambda_N = 90\%$, for SR2: $\lambda_{\text{NZ}} = \lambda_Z = 90\%$, for SR3: $\lambda_{\text{NZ}} = 100\%$ and $\lambda_Z = 90\%$) and with increments that result in integer values of $N_{\text{S-NZ}}$ and $N_{\text{S-Z}}$. When choosing the initial λ value of 90% option, it is advantageous to note that since QMC point-sets are deterministic, the entire simulation need not be re-run in case λ values need to be incremented. Instead, only the QMC points that succeed the points required for satisfying the previously rejected λ value can be used for satisfying the current λ value. Also, since atmospheric inverse-source problems always comprise sparse number of sensor measurements (N), the maximum number of times that the proposed approach needs to be run is theoretically N . To provide the reader an estimate for the values of N , currently, approximately 500 sensors have been placed in

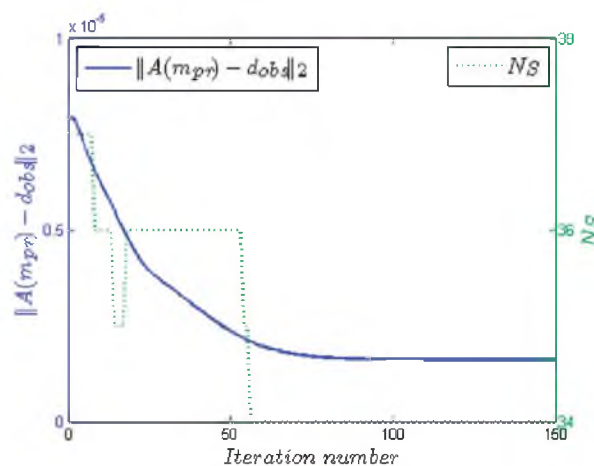


Figure 4. Convergence of Newton's method for TCTE.

31 US cities according to the Bio-Watch program, which on an average reduces to 16 sensors per city ($N=16$) [34].

5. Results and discussion

5.1. Final model parameters and comparison with results from the literature

The final model parameters obtained using Newton's method are shown in Table 2. For these simulations, the Mersenne–Twister generator was used in the stochastic search stage (the random number seed was set equal to zero). In Table 2, m_t represents the true model parameters from TCTE. The parameters m_{STOCH} are the initial iterates obtained from the stochastic stage when SR1 was used with $N_S \geq 37$. The parameters $m_{\text{STOCH} \cdot \max(N_S)}$ represent the model parameters that satisfy the maximum number of sensor measurements ($N_S = 39$). The final solution from Newton's method is denoted as $m_{\text{STOCH}+\text{GD}}$. The convergence of Newton's method is illustrated in Figure 4. Based on the value of the norm of the residuals in the iteration space, as well several runs (using the Mersenne–Twister generator), it was found that when Newton's method converged, it converged at $N_S = 34$, after about 100 iterations (Figure 4). Irrespective of the strategy (SR1, SR2 or SR3) chosen to identify an initial iterate, Newton's method always converged to the final model parameters given by $m_{\text{STOCH}+\text{GD}}$. This brings us to the question raised in Section 4.7 concerning 'model-fit' and 'data-fit'. From the results in Table 2 it can be clearly seen that the solution provided by Newton's method results in the minimum value of the norm of the residuals, while that provided by the stochastic search results in better 'data-fit'. The performance of the various QMC point-sets in terms of number of points required for identifying an initial iterate are discussed in the subsequent sections (Section 5.2). The performance of Newton's method in terms of number of iterations required to converge to the final solution depending on the strategy chosen is discussed in Section 5.3.

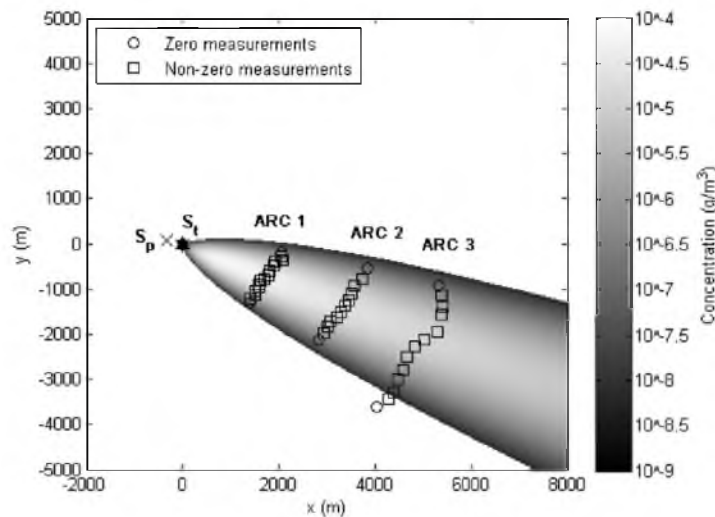


Figure 5. Plume spread predicted by model parameters from inversion. The squares (\square) and the circles (\circ) represent sensors that recorded non-zero and zero measurements. ' S_t ' (hexagon - \star) is the true source location in, and ' S_p ' (cross - \times) the location predicted by Newton's method.

The work of [9] used data from TCTE to demonstrate the Bayesian approach to solve the atmospheric inverse-source problem. The model parameters obtained from Newton's method cannot be directly compared to those obtained by [9] as [9] did not provide the expected values for the final model parameters. However, Figure 6 in their work shows the probabilistic plume spread for 95% confidence level. In Figure 5, the plume spread predicted by the parameters from Newton's method is shown. Comparing the figures it can be seen that the plume spread predicted by both the approaches has the same underlying characteristics in terms of the zero and non-zero measurements satisfied. Comparing Figure 5 with Figure 1 from this work, it can be seen that the plume spread predicted by parameters obtained from inversion matches the plume spread observed in TCTE better than the plume spread predicted by the true parameters.

The work of [20] also used the Copenhagen data for inversion. They employed a Langevin equation-based forward model and used the dataset recorded between 12:13 h and 12:33 h on 19 October 1978 (instead of the mean dataset, which is used in this work). To compare with the results of [20], the present approach is implemented with the dataset adopted by [20].

From Table 3 it can be seen that the predicted data from Newton's method matches 26 out of the 27 non-zero measurements, and 6 out of the 12 zero measurements, resulting in total number of matched measurements of 32 out of 39. In comparison, the predictions from [20] match all the non-zero measurements, but do not match any of the zero measurements, resulting in total matched measurements of 27 out of 39. Also, the values predicted by the present approach are closer to the observed data, than those predicted by [20]. The final model parameters predicted by Newton's method for the dataset between 12:13 h and 12:33 h are shown in Table 4. From Table 4 it is seen that using this dataset leads to improvement in inversion accuracy.

Table 3. Comparison of the predicted concentrations from Newton's method with Copenhagen data (12:13 h–12:33 h on 19 October 1978) and [16].

Position	Sensor x-coordinate (m)	Sensor y-coordinate (m)	Observed concentration (ng m ⁻³)	Predicted concentration [16] (ng m ⁻³)	Predicted concentration from this work (ng m ⁻³)
9	1398	-1312	0	721	0
10	1404	-1214	0	135	28
11	1492	-1131	186	2271	259.4
12	1516	-1044	614	3266	896
13	1582	-964	1816	4478	2672
14	1592	-884	5455	5105	4642.9
15	1602	-798	7016	5727	6682.1
16	1703	-767	6770	5582	7161.6
17	1766	-681	5472	5077	5860.7
18	1800	-593	3806	4067	3523.4
19	1877	-485	1114	2842	1053.1
20	1921	-405	919	1969	320.4
21	2067	-371	77	1902	101.6
22	2061	-284	0	1001	22.5
23	2055	-180	0	463	0
11	2818	-2134	0	1400	53.3
12	2920	-1987	107	1579	295.3
13	3002	-1830	840	2635	1022.3
14	3075	-1704	1478	2691	2029.3
15	3204	-1629	3133	2580	2797.2
17	3380	-1367	2563	2249	2627.3
18	3448	-1231	2225	2033	1614.8
19	3518	-1093	538	1282	722.2
20	3558	-919	0	1050	194.8
21	3729	-787	0	361	33.4
22	3837	-550	0	121	0
9	4027	-3616	0	306	0
10	4283	-3447	18	788	0
11	4390	-3277	21	1087	12.4
12	4459	-3010	85	1117	97.6
13	4572	-2795	800	1552	396.8
14	4668	-2514	1502	1236	1180.5
15	4824	-2260	2035	1297	1762.0
16	5029	-2108	1112	1063	1476.7
17	5286	-1939	434	778	761.8
18	5378	-1570	53	124	129.9
19	5395	-1399	0	49	42.1
20	5375	-1139	0	109	0
21	5323	-913	0	47	0

5.2. Performance of the various QMC point-sets in the stochastic search stage

The performance of the various QMC point-sets for SR1 and SR3 for the different N_S values described in Sections 4.3.2.1 (SR1) and 4.3.2.3 (SR3) is compared against the Mersenne–Twister pseudorandom generator. In the stochastic search stage, the number of

Table 4. Computed inversion model parameters for TCTE using the dataset between 12:13 h and 12:33 h.

Model parameters	x_S (m)	y_S (m)	z_S (m)	q_S/u_S (gm^{-1})	θ_S (degrees)	N_S
m_t	0	0	115	0.64	308.57	–
$m_{\text{STOCH+GD}}$	64.001	2.58	181.49	1.11	295.11	32

Table 5. Performance of the various original QMC point-sets with SR1.

Point-sets	$N_S \geq 37$	$N_S \geq 38$	$N_S \geq 39$
$E(\text{MC})$	12,633	82,102	25,000,000
O -Halton	6521	50,081	6666,989
O -Hammersley	678	17,730	4903,807
O -Sobol	1649	18,761	437,165
O -SplNie	24,377****	97,632****	1150,264
O -NieXing	10,040	159,266****	4434,687

Table 6. Performance of the various scrambled QMC point-sets with SR1.

Point-sets	$N_S \geq 37$	$N_S \geq 38$	$N_S \geq 39$
$E(\text{MC})$	12,633	82,102	25,000,000
S -Halton	797	43,565	1740,461
S -Hammersley	2047	9250	–
S -Sobol	1230	23,758	1213,246
S -SplNie	29,265****	49,313	–
S -NieXing	6087	6087	2414,141

Table 7. Performance of the various original QMC point-sets with SR3.

Point-sets ($N_{S-NZ} = 34$)	$N_{S-Z} \geq 5$	$N_{S-Z} \geq 4$	$N_{S-Z} \geq 3$	$N_{S-Z} \geq 2$	$N_{S-Z} \geq 1$
$E(\text{MC})$	25,000,000	114,943	32,342	12,533	9371
O -Halton	6666,989	50,081	50,081****	50,081****	50,081****
O -Hammersley	5258,175	–	4010	678	90
O -Sobol	437,165	18,761	1649	1649	1649
O -SplNie	1150,264	97,632	81,072****	10,224	10,224****
O -NieXing	–	171,000****	22,536	2240	2240

QMC points required to satisfy a given N_S value ($N_S = k$) was determined by the minimal number of points that satisfy $N_S \geq k$. The results obtained are shown in Tables 5–8.

In Tables 5–8, $E(\text{MC})$ stands for the expected number of random samples required from the Mersenne–Twister generator to satisfy the given criteria. The letters O and S

Table 8. Performance of the various scrambled QMC point-sets with SR3.

Point-sets ($N_{S-NZ}=34$)	$N_{S-Z} \geq 5$	$N_{S-Z} \geq 4$	$N_{S-Z} \geq 3$	$N_{S-Z} \geq 2$	$N_{S-Z} \geq 1$
$E(MC)$	25,000,000	114,943	32,342	12,533	9371
S -Halton	18,025,133	188,933****	19,841	10,961	10,961
S -Hammersley	–	–	–	262	262
S -Sobol	–	23,758	1230	1230	1230
S -SplNie	–	49,313	29,265	10,609	9473****
S -NieXing	2414,141	6087	6087	4651	4651

before the various QMC point-sets are indicative of their original or scrambled nature. *SplNie* and *NieXing* are abbreviations for the SpecialNiederreiter and Niederreiter point-sets.

Based on the results obtained for SR1 and SR3 from Tables 5–8, the following conclusions can be made: (1) the QMC point-sets on average perform better than Mersenne–Twister generator for most of the cases, and (2) of all the QMC point-sets, the original Sobol sequence and the scrambled NiederreiterXing point-set perform better than the others (and the Mersenne–Twister generator).

The arguments based on which the original Sobol sequence and the scrambled NiederreiterXing point-set were determined to be the best of the point-sets considered are as follows: (1) The Hammersley point-set is not recommended as its first dimension is the regular 1D lattice evenly distributed on the interval $[0, 1)$. Therefore, based on the number of points generated, the Hammersley sequence changes in the first dimension. Since the optimum number of points that should be generated for identifying the initial iterate with the fewest possible points is not known *a priori*, the Hammersley point-set is not recommended. Also, if the proposed approach is implemented with initial $\lambda = 90\%$ option, and if the λ value needs to be incremented subsequently, the entire simulation should be re-run if the Hammersley sequence is used. (2) Apart from the original Sobol and the scrambled NiederreiterXing point-sets, all other point-sets exceed the number of MC points required in at least one of the reported results in Tables 5–8. Such results are indicated either by the asterisk superscript (****), or have not been reported (indicated by ---) (whenever the number of QMC points required is much larger than $E(MC)$).

5.3. Overall performance of the proposed approach

The overall computational cost and thereby the execution time of the proposed approach can be divided between the stochastic and gradient stages. Depending on the strategy and the QMC point-set chosen in the stochastic stage, the computational costs and the execution times of the stochastic and the gradient stages vary. For TCTE, Newton’s method always took less than 200 iterations irrespective of the strategy employed. The choice of SR1, SR2 and SR3 depends on the complexity of the problem at hand and on how much one is willing to expend on the stochastic search stage. To get an estimate for the execution time of the present approach, stochastic search was performed with the criteria, $N_S \geq 37$. Stochastic search was performed with the Mersenne–Twister generator, with the random number seed set to zero. With the initial iterate provided by the stochastic stage, 200 Newton iterations were run. The algorithm was implemented in 32-bit Matlab

7.8.0 (R2009a) and was executed on a 64-bit Dell desktop machine running Windows Vista, with 8Gb RAM, and 3.0 GHz QuadCore processor. The overall execution time was ~ 3 s, with the stochastic stage taking ~ 2.3 s, and Newton's method taking ~ 0.7 s.

6. Conclusions

An inversion technique comprising stochastic search and regularized gradient optimization to solve the atmospheric inverse-source problem is described in this article. The inverse problem involves retrieving the spatial coordinates, source strength and the wind speed and wind direction at the source, given certain receptor locations and concentration values at these receptor locations. The GPM is adopted as the forward model and derivative-based optimization is chosen to take advantage of its simple analytical nature. The proposed approach is explained using the Copenhagen field experiment data. Stochastic search is performed over the domain of the misfit functional to identify an initial iterate for the gradient scheme. A new misfit functional is developed to take into account the zero and non-zero measurements recorded by the receptors and is used in the stochastic stage. It is based on the base 10 logarithm of the ratio of the observed and predicted data and it is shown that the new misfit functional improves the inversion accuracy. Several QMC point-sets in their original and scrambled forms are considered in the stochastic stage. Their performance are evaluated against the Mersenne–Twister generator. QMC point-sets are recommended for atmospheric inverse-source problems due to their deterministic and superior space-filling nature. Three strategies to solve the inverse-source problem are proposed and are implemented in the stochastic stage. The original Sobol and the scrambled NiederreiterXing point-sets are found to produce the best results across all the test cases considered. Newton's method with the Tikhonov stabilizer and adaptive regularization with quadratic line-search is implemented in the gradient stage. The final solution obtained from Newton's scheme is close to the true model parameters from the Copenhagen data.

References

- [1] M.S. Zhdanov, *Geophysical Inverse Theory and Regularization Problems – Methods in Geochemistry and Geophysics*, Elsevier, Amsterdam, The Netherlands, 2002.
- [2] Z.B. Zabinsky, *Stochastic Adaptive Search for Global Optimization*, Kluwer Academic, Dordrecht, The Netherlands, 2003.
- [3] R. Sneider, *The role of nonlinearity in inverse problems*, Inverse Probl. 14 (1998), pp. 387–404.
- [4] P.J. Ballester and J.N. Carter, *Characterizing the parameter space of a highly nonlinear inverse problem*, Inverse Probl. Sci. Eng. 14 (2006), pp. 171–191.
- [5] B.L.N. Kennett, *Consistency regions in non-linear inversion*, Geophys. J. Int. 157 (2004), pp. 583–588.
- [6] A. Lomax and R. Sneider, *Identifying sets of acceptable solutions to non-linear, geophysical inverse problems which have complicated misfit functions*, Nonlinear Processes Geophys. 2 (1995), pp. 222–227.
- [7] M. Sambridge, *Finding acceptable solutions in nonlinear inverse problems using a neighbourhood algorithm*, Inverse Probl. 17 (2001), pp. 387–403.
- [8] F. Chow, B. Kosovic, and S.T. Chan, *Source inversion for contaminant plume dispersion in urban environments using building-resolving simulations*, J. Appl. Meteorol. Climatol. 47 (2008), pp. 1553–1572.

- [9] I. Senocak, N.W. Hengartner, M.B. Short, and B.W. Daniel, *Stochastic event reconstruction of atmospheric contaminant dispersion using Bayesian inference*, Atmos. Environ. 42 (2008), pp. 7718–7727.
- [10] V. Akecelik, G. Biros, A. Draganescu, O. Ghattas, J. Hill, and B.V.B. Waanders, *Lecture Notes on Computational Science*, International Conference on Computational Science, Reading, 2006.
- [11] X. Davoine and M. Bocquet, *Inverse modelling-based reconstruction of the Chernobyl source term available for long-range transport*, Atmos. Chem. Phys. Discuss. 7 (2007), pp. 1–43.
- [12] S. Houweling, T. Kamsinki, F. Dentener, J. Lelieveld, and M. Heimann, *Inverse modelling of methane sources and sinks using the adjoint of a global transport model*, J. Geophys. Res. 104 (1999), pp. 26137–26160.
- [13] R.B. Storch, L.C.G. Pimentel, and H.R.B. Orlando, *Identification of atmospheric boundary layer parameters by inverse problem*, Atmos. Environ. 41 (2007), pp. 1417–1425.
- [14] J.A. Scales and L. Tenorio, *Prior information and uncertainty in inverse problems*, Geophysics 66 (2001), pp. 389–397.
- [15] S.E. Gryning and E. Lyck, *The Copenhagen tracer experiments: Reporting measurements*, Riso National Laboratory, Roskilde, 1998.
- [16] A.J. Annunzio, S.E. Haupt, and G.S. Young, *Source Characterization and Meteorology Retrieval including Atmospheric Boundary Layer Depth using Genetic Algorithm*, 15th Joint Conference on the Applications of Air Pollution Meteorology with the A&WMA, New Orleans, LA, 2008.
- [17] M.J. Brown, M.D. Williams, G.E. Streit, M. Nelson, and S. Linger, *An Operational Event Reconstruction Tool: Source Inversion for Biological Agent Detectors*, 86th American Meteorological Society Annual Meeting, 2006.
- [18] S.E. Haupt, R.L. Haupt, and G.S. Young, *Using Genetic Algorithms in Chem-bio Defense Applications*, Proceedings of the 2007 ECSIS Symposium on Bio-inspired, Learning, and Intelligent Systems for Security, 2007.
- [19] A. Khemka, C.A. Bouman, and M.R. Bell, *Inverse problems in atmospheric dispersion with randomly scattered sensors*, Digit. Signal Process. 16 (2006), pp. 638–651.
- [20] K.J. Long, S.E. Haupt, G.S. Young, and C.T. Allen, *Characterizing Contaminant Source and Meteorological Forcing using Data Assimilation with a Genetic Algorithm*, 86th American Meteorological Society Annual Meeting, 2006.
- [21] D.R. Roberti, D. Anfossi, H.F. de Campos Velho, and G.A. Degrazia, *Estimation of pollutant source emission rate from experimental data*, Il Nuovo Cimento 30 C(02) (2007), pp. 177–186.
- [22] L.C. Thomson, B. Hirst, G. Gibson, S. Gillespie, P. Jonathan, K.D. Skeldon, and M.J. Padgett, *An improved algorithm for locating a gas source using inverse methods*, Atmos. Environ. 41 (2007), pp. 1128–1134.
- [23] M.R. Beychok, *Fundamentals of Stack Gas Dispersion*, M.R. Beychok, Irvine, CA, 2005.
- [24] B.D. Turner, *Workbook of Atmospheric Dispersion Estimates – An Introduction to Dispersion Modelling*, CRC Press, Boca Raton, FL, 1994.
- [25] Y. Zhou and S.R. Hanna, *Along-wind dispersion of puffs released in a built-up urban area*, Boundary-Layer Meteorol. 125 (2007), pp. 469–486.
- [26] R.I. Sykes, C.P. Cerasoli, and D.S. Henn, *The representation of dynamic flow effects in a Lagrangian puff dispersion model*, J. Hazardous Mater. 64 (1999), pp. 223–247.
- [27] A. Trantola, *Inverse Problem Theory and Methods for Model Parameter Estimation*, SIAM, Philadelphia, PA, 2004.
- [28] C.R. Vogel, *Computational Methods for Inverse Problems*, SIAM, Philadelphia, PA, 2002.
- [29] D. Edwards, *Practical sampling for ray-based rendering*, Ph.D. diss., University of Utah, 2008.
- [30] H. Niederreiter, *Random Number Generation and Quasi-Monte Carlo Methods*, CBMS-NSF Regional Conference Series in Applied Mathematics, 1992.
- [31] J. Matousek, *On the L₂-discrepancy for anchored boxes*, J. Complex. 14 (1998), pp. 527–556.
- [32] R.C. Aster, B. Borchers, and C. Thurber, *Parameter Estimation and Inverse Problems*, Elsevier, Amsterdam, The Netherlands, 2005.

- [33] D. Zajic and M.J. Brown, *Source Inversion in Cities using the Collector Footprint Methodology*, 88th American Meteorological Society Annual Meeting, 2008.
- [34] Anonymous, *Synopsis of the January 22-23, 2004 secretary's council on public health preparedness*, Biosecurity Bioterrorism: Biodefense Strat., Practice Sci. 2 (2004), pp. 41–45.
- [35] C.T. Allen, S.E. Haupt, and G.S. Young, *Application of Genetic Algorithm-coupled Receptor/dispersion Model to the Dipole Pride 26 Experiments*, 14th Joint Conference on the Applications of Air Pollution Meteorology with the Air and Waste Management 2006.
- [36] C.T. Allen, G.S. Young, and S.E. Haupt, *Improving pollutant source characterization by better estimating wind direction with a genetic algorithm*, Atmos. Environ. 41 (2007), pp. 2283–2289.
- [37] J.V. Beck and K.A. Woodbury, *Inverse problems and parameter estimation: integration of measurement and analysis*, Meas. Sci. Technol. 9 (1998), pp. 839–847.
- [38] M. Bocquet, *Reconstruction of an atmospheric tracer source using the principle of maximum entropy: I. Theory*, Q. J. R. Meteorol Soc. 131 (2005), pp. 2191–2208.
- [39] M.N. Bradley, B. Kosovic, and J.S. Nasstrom, *Models and Measurements: Complementary Tools for Predicting Atmospheric Dispersion and Assessing the Consequences of Nuclear and Radiological Emergencies*, International Conference on Monitoring, Assessments, and Uncertainties for Nuclear and Radiological Emergency Response, 2005.
- [40] P.E. Frandsen, K. Jonasson, H.B. Nielsen, and O. Tingleff, *Unconstrained Optimization*, Informatics and Mathematical Modelling, Technical University of Denmark.
- [41] K.M. Hanson, *Quasi-Monte Carlo: Halftoning in high dimensions?*, Proc. SPIE 5016(1) (2003), pp. 161–172.
- [42] S.E. Haupt and G.S. Young, *Paradigms for Source Characterization*, 88th American Meteorological Society Annual Meeting, 2008.
- [43] W.R. Hogan, G.F. Cooper, M.M. Wagner, and G.L. Wallstrom, *An inversion Gaussian plume model for estimating the location and amount of release of airborne agents from downwind atmospheric concentrations*, The RODS laboratory, University of Pittsburgh.
- [44] M.A. Islam, *Application of the Gaussian plume model to determine the location of an unknown emission source*, Water Air Soil Pollut. 112 (1999), pp. 241–245.
- [45] C.T. Kelley, *Solving Nonlinear Equations with Newton's Method – Fundamentals of Algorithms*, SIAM, Philadelphia, PA, 1987.
- [46] C. Lemieux, *Monte Carlo and Quasi-Monte Carlo Sampling*, Springer, New York, 2009.
- [47] K. Mosegaard and A. Trantola, *Monte Carlo sampling of solutions to inverse problems*, J. Geophys. Res. 100 (1995), pp. 12431–12447.
- [48] M. Sambridge, C. Beghein, F.J. Simons, and R. Snieder, *How do we understand and visualize uncertainty?*, Lead. Edge 25 (2006), pp. 542–546.
- [49] M. Sambridge, *Inverse problems in a nutshell*, Center for Advanced Data Inference, Research School of Earth Sciences, Australian National University, ACT 0200, Australia.
- [50] M. Sambridge and K. Mosegaard, *Monte Carlo methods in geophysical inverse problems*, Rev. Geophys. 40 (2002), pp. 1–29.
- [51] A. Wirgin, *The inverse crime*, * LMA/CNRS, 31 chemin Joseph Aiguier, 13402 Marseille cedex 20, France.

CHAPTER 5

URBAN FORM OPTIMIZATION FOR IMPROVED AIR QUALITY

5.1 Abstract

In the work presented, the problem of identification of urban forms that result in the lowest pollutant concentrations in an urban domain is referred to as the urban form optimization problem (UFOP). In the solution of UFOPs, the quick urban and industrial complex (QUIC) dispersion modeling system adapted to graphics processing units (GPU) is adopted as the simulation (forward) model. Simulated annealing (SA) and a genetic algorithm (GA) are considered as the optimization techniques. To demonstrate the application of SA and GA in the solution of UFOPs, a simple 2×2 building array (eight-dimensional) problem is considered, where the decision variables are the spatial locations of the buildings. Minimizing the average and maximum concentrations at street level were considered to be the objective functions. Exhaustive search was performed (65 536 possible configurations), and results from SA and GA are compared against exhaustive search data. To evaluate the performance of SA and GA, they were run 10 000 times using exhaustive search data, to find the frequency with which they converge to the globally optimum solution. The GA converged to the globally optimum solution in all the simulations (100% success rate), while the success rate of SA was 51.98%. The results obtained for the 2×2 building array problem indicate that the optimum configurations obtained using QUIC-GPU are inline with intuition and that GA performs exceedingly well in the identification of optimum urban configurations.

5.2 Introduction

A significant fraction of the world's population lives in urban areas. In the coming years, continual migration to urban areas will only see the fraction of urban populace increase. Since cities are regions of intense activity, are the dominant consumer of resources, and major producers of waste, urbanization introduces an array of environmental challenges including those related to air quality. There are two possible solutions to this problem,

(1) design from scratch, cities that are environmentally sustainable (which is impractical) and (2) modify existing designs over time so that they eventually become environmentally sustainable. In the work presented, how optimization techniques when coupled with flow and dispersion models can help realize either of the above two solutions is demonstrated.

The problem of identification of urban forms that result in the lowest pollutant concentrations is referred to as the urban form optimization problem (UFOP). A review of the literature suggests that there have been a few studies that have that have investigated the effect of urban form on air pollutant concentrations. Most of these studies did not explicitly model the flow around individual buildings. For instance, [1] used an extremely crude dispersion model to investigate the relationship between increased city sprawl and pollution levels in a city for a fixed population size. The work of [2] proposed a framework for integrating geographic information systems (GIS) data with a vehicle emissions model, and a simple Gaussian dispersion model. [3] compared four different planning scenarios: compact development (high-density), multinodal (high-intensity development in distinctive clusters), corridor (growth along transport routes), and business as usual (a sprawl scenario), in Melbourne, Australia. They also linked a geographic based model to a vehicle emission model and a simple dispersion model. From their study, they found that while a compact city produced lower emissions, the concentration levels were quite high. Of the four different choices they considered, the corridor city resulted in the lowest concentration values. In the work of [4], ozone pollution and related chemistry in three idealized cities was modeled using a mesoscale meteorological model with a more sophisticated transport model for dispersion. They modeled a sprawling city, a compact city, and a corridor city. They found that emissions were the highest in the corridor city, but concentrations were the lowest in the compact city and the corridor city.

The work of [5] is the only work to have considered flow and dispersion around individual buildings to identify optimum urban geometries. In their work, they used the commercial computational fluid dynamics (CFD) package STAR-CD, together with the optimization package DYNAMIC-Q, to identify urban geometries that minimize peak pollution levels due to vehicle induced emissions. While their solution methodology is indisputable, it has two serious limitations. The limitations are (1) the number of decision variables that can be considered cannot be too large due to the computationally intensive nature of the forward model and (2) due to the computational cost of the forward model, one has to resort to greedy algorithms for optimization, which may not provide accurate final solutions.

The above discussion amply demonstrates that the solution of UFOP poses several challenges. The most important of them are (1) the computationally intensive nature of the forward model and (2) the dimensionality of the problem. A forward model must be based on the governing equations for flow and dispersion for it to adequately capture the physics of the problem. Any such forward model will be computationally intensive. The UFOP is high-dimensional as each urban object can have several degrees of freedom in the parameter space.

To counter the challenge posed by computationally intensive nature of forward models, the quick urban and industrial complex (QUIC) dispersion modeling system [6] adapted to graphics processing units (GPU) [7] (QUIC-GPU) is adopted as the forward model to solve the UFOP (simulation-based optimization). Simulated annealing (SA) and genetic algorithms (GA) are considered as the optimization techniques to identify optimum urban forms. To demonstrate the application of QUIC-GPU, and SA and GA in the solution of UFOPs, a simple 2×2 building array (eight-dimensional) problem is considered.

5.3 Problem Definition

The problem of identification of (optimum) urban parameters (e.g., building layouts, meteorological variables, etc.) that result in the lowest pollutant concentrations is referred to as the urban form optimization problem (UFOP). The solution of UFOP is comprised of three principal components (1) the forward prediction (simulation) model, (2) an objective function and (3) an optimization technique. In this section, the choices for these components are described.

5.3.1 The Forward Problem

Numerical modeling of flow and dispersion in urban environments for a given set of urban parameters is called the forward problem. The forward problem solution helps predict the flow and dispersion in urban domains for a given set of urban parameters. The numerical model used in the forward problem solution is the forward model. To solve the UFOP, a forward model is assumed. The accuracy of the UFOP solution therefore depends upon how well the forward model captures the urban flow physics.

Mathematically, the forward problem is described by (5.1). In (5.1), f is the forward modeling operator, ω represents a set of urban parameters from the urban parameter space Ω , and C is the predicted concentration data in the urban domain for the given parameters ω . In (5.1), \mathcal{C} is the concentration data space, and $f : \Omega \rightarrow \mathcal{C}$. Typically, $\Omega \subset \mathbb{R}^{n_1}$, where

\mathbb{R} is set of real numbers, and n_1 represents the dimension of the parameter space. As mentioned in the previous section, n_1 can be very large for UFOPs.

$$f(\omega) = C, \omega \in \Omega, C \in \mathcal{C}. \quad (5.1)$$

In the present work, the quick urban and industrial complex (QUIC) dispersion modeling system [6] adapted to graphics processing units (GPUs) (QUIC-GPU) [7] is used as the forward model f . QUIC consists of a diagnostic wind model (QUIC-URB), a random-walk dispersion model (QUIC-PLUME), a pressure solver, and a graphical user-interface (QUIC-GUI). QUIC-URB computes spatially-resolved mean wind fields in urban domains. It is based on empirical flow parameterizations and mass conservation. The dispersion model QUIC-PLUME is an unsteady *urbanized* random-walk model with a nonlocal mixing scheme. QUIC-PLUME is based on the Langevin equations. Additional details about QUIC can be found in [6, 7].

The standard QUIC dispersion model runs extremely fast. When compared to other prognostic models used to simulate flow and dispersion in urban areas, QUIC runs two to three orders of magnitude faster and produces similar results [8, 9]. However, QUIC is still not fast enough to be used in the solution of UFOP, which require several thousand forward model evaluations. Therefore to use QUIC to solve UFOP, it has been adapted to GPU to take advantage of the massive data parallelism afforded by these units [7].

5.3.2 The Objective Function

An objective function is a function used to determine the optimality of an urban form. An objective function (\mathcal{H}) is a rule that assigns a single real number to every layout (ω) in the parameter space (Ω), based on the predicted concentration vector (C). That is, $\mathcal{H} : \Omega \rightarrow \mathbb{R}^1$. The objective function utilizes the forward model (QUIC-GPU) to determine the optimality of an urban form. The solution of UFOP consists of determining the arguments (urban parameters) at which the objective function attains its optimum (minimum or maximum) value. Typical examples of objective functions for the UFOP include the maximum and average concentrations at the street level, the mortality rate, etc. Using the definition of the objective function, the UFOP is cast as an optimization problem as shown in (5.2). In (5.2), ω_{opt} represents the optimum urban form from the urban parameter space (Ω) considered, assuming that the arguments corresponding to the minimum of the objective function are desired.

$$\omega_{opt} := \arg \left(\min_{\omega \in \Omega} \mathcal{H}(\omega) \right). \quad (5.2)$$

5.3.3 Optimization Techniques

For the UFOP, with QUIC-GPU as the forward model, analytical expressions for the gradient of the objective function cannot be computed. The parameter space over which the UFOP is solved is usually assumed to be discrete (finite). Also, with QUIC-GPU as the forward model, global convexity of the objective function over the parameter space cannot be shown to hold theoretically. Therefore, in solution of UFOPs, stochastic *derivative-free* optimization techniques such as simulated annealing (SA) and genetic algorithms (GA) are considered. SA and GA are considered as each has its own theoretical and intuitive appeal. A brief description of the variants of SA and GA used are given in this section.

5.3.3.1 Simulated Annealing - SA

Simulated annealing (SA) [10] is a stochastic global optimization technique (Markov chain Monte Carlo [MCMC] method) used to find the arguments at which an objective function attains its optimum value. SA is based on the Metropolis algorithm [11, 12], which was developed to simulate the evolution of a solid to thermal equilibrium. SA works by simulating the cooling of a fictitious physical system (urban parameter space) whose energies correspond to the objective function values. The analogy works because physical systems occupy the lowest energy states with very high probability when in thermal equilibrium. Parallels can be drawn between the physical states of a system and urban configurations, and energies and air-quality levels, and this gives SA its intuitive appeal. Along with the above-mentioned analogy, SA is also backed by the theory of Markov chains. The SA algorithm is essentially a Markov chain (a sequence of random variables indexed by time) with its stationary distribution being the Boltzmann distribution [13, 14]. Thus, SA has proof of convergence [13–16], which gives it its theoretical appeal.

In SA, given (starting with) an urban configuration ω_i , a new configuration ω_j is generated using a suitable configuration-generating mechanism (rule). Assuming that the arguments corresponding to the global minimum of the objective function $\mathcal{H}(\omega)$ are to be found, the new configuration ω_j is accepted if $\Delta\mathcal{H}(\omega_i, \omega_j) \leq 0$, where $\Delta\mathcal{H}(\omega_i, \omega_j) := \mathcal{H}(\omega_j) - \mathcal{H}(\omega_i)$. If $\Delta\mathcal{H}(\omega_i, \omega_j) > 0$, then the new configuration ω_j is accepted with probability, $\exp[-\Delta\mathcal{H}(\omega_i, \omega_j)/T_i]$. The probability $\exp[-\Delta\mathcal{H}(\omega_i, \omega_j)/T_i]$ is called the Metropolis acceptance criterion [11–14]. The parameter T_i ($T_i > 0$) is an artificial temperature parameter. The value of T_i determines the extent to which one is willing to accept pro-

posed configurations with higher objective function values than the current configuration. Typically, the algorithm is implemented by starting with a large value of the temperature parameter, and the parameter is progressively lowered. Loosely speaking, in the initial stages of SA, when the temperature parameter is large, random search performed over the urban parameter space, while at lower temperatures, local-search is strongly favored. This feature of the SA algorithm helps in the exploration of the urban parameter space and reduces the chances of the algorithm getting stuck in local minima.

For inhomogeneous SA Markov chains (where temperature is a monotonous function of time), a temperature reduction schedule (along with an *appropriate* candidate-generating mechanism) that ensures convergence to the global optima with probability 1 is the logarithmic schedule (see for example, [13, 15]). The logarithmic schedule requires the rate of decrease of the temperature parameter T_t over time t to not be faster than $\mathcal{O}(1/\log(t))$. The logarithmic schedule is however impracticable in real-life applications. Therefore, in practical implementations, conceptually simpler and more practical cooling schedules are used, and hence, SA only finds *good* solutions (which could be the globally optimum solution[s]). That is, in practical applications of SA, the proof of convergence (which guarantees convergence to the global optima) is rendered ineffectual. In the current SA implementation, a geometric cooling schedule is used for decreasing the values of the temperature parameter. That is, starting with an initial temperature T_0 , the temperature on the i^{th} iteration is determined using, $T_i = \alpha^i T_0$, where $0 < \alpha < 1$.

5.3.3.2 Binary Genetic Algorithm - BGA

Genetic algorithms are based on the principles of genetics and natural evolution [17, 18]. In GA, the (urban) parameter space is explored by a group of *chromosomes* simultaneously. A GA is based on the *survival of the fittest* principle, with a structured yet randomized information exchange between the chromosomes [17]. GAs are not random walks (like SA), and therefore do not have general proofs of convergence. Despite lacking in mathematical rigor, the intuitive appeal of GA is due to two reasons (1) human reasonings of how the parameter space should be explored is encoded into the structured information exchange between the chromosomes and (2) investing in a group of information exchanging chromosomes to explore the parameter space and identify the global optimum seems intuitively a better option than banking on a single sequence of random variables (SA Markov chain).

In the current work, a binary genetic algorithm (BGA) is implemented. The variant of BGA implemented is described in [18]. In GA, the vector of decision variables to be optimized is referred to as a *chromosome*. In the BGA, a chromosome is represented as

an encoded binary string. The number of bits used to represent a decision variable as a binary string is user dependent. The BGA begins with a group of randomly generated *chromosomes* called the *population*. The objective function is evaluated at each *chromosome* of the population. Based on the evaluation, the *chromosomes* are ranked (sorted) starting from the best to the worst. A fraction of the bad-performing *chromosomes* are discarded to enforce the *survival of the fittest principle*. The fraction of the population that survives is referred to as the *survival rate*. The discarded bad-performing *chromosomes* are replaced by offspring's generated from the surviving *chromosomes*. This process is referred to as *selection*, and in the present work, *selection* is based on *rank-weighting* and *single-point crossover*. To prevent clustering of all the *chromosomes* near good-performing *chromosomes* (in the decision variable space), random mutations (swapping of the bits) are introduced in the population. The best-performing *chromosome* is not subject to mutation and is saved as an *elite* solution. The process is then repeated for a few iterations, and the *elite* solution is taken as the final answer.

5.4 The Eight-Dimensional Test Problem

To demonstrate the application of SA and BGA in the solution of UFOP, a simple urban optimization problem consisting of a 2×2 building array is considered. The schematic of the problem is shown in Fig. 5.1. In Fig. 5.1, four cubical buildings of dimensions $10 \text{ m} \times 10 \text{ m} \times 10 \text{ m}$, numbered 1, 2, 3, and 4, are shown in the plan-view ($x - y$ plane). The domain size for the test problem is $80 \text{ m} \times 60 \text{ m} \times 20 \text{ m}$. The two dashed lines in the domain indicate two line-emitters (continuous line-sources), numbered I and II. Emitter I is along the x -direction, and emitter II is in the y -direction. The emitters are placed 0.5 m above the ground level. The length of each emitter is 30 m. The two emitters divide the square region ABCD into four smaller square regions, AEJG, EBHJ, JHCF, and GJFD, which house the buildings. The wind direction for this problem is $\theta = 270$ degrees (wind coming from the west). For a user-specified objective function let the decision variables be the x and y -coordinates of the buildings (all the other parameters are assumed to be known). Also for simplicity, assume that each building can only move four discrete grid cells from its initial position along the x and y -directions within the square the building is contained in (that is, building 1 cannot jump out of GJFD). Based on the problem formulation, the relatively simple-looking 2×2 building array problem is an eight-dimensional (8D) problem. That is because each building has two degrees of freedom in the decision variable space. The location of each building is identified by the unique ordered pair (x_i, y_i) , where the

subscript i indicates the building number, and x and y represent the x and y -coordinates of the midpoint on the left-edge of the building in the plan view. The bounds on the parameter space are, $x_1, x_4 \in \{20 \text{ m}, 21 \text{ m}, 22 \text{ m}, 23 \text{ m}\}$; $y_1, y_2 \in \{37 \text{ m}, 38 \text{ m}, 39 \text{ m}, 40 \text{ m}\}$; $x_2, x_3 \in \{37 \text{ m}, 38 \text{ m}, 39 \text{ m}, 40 \text{ m}\}$; and $y_3, y_4 \in \{20 \text{ m}, 21 \text{ m}, 22 \text{ m}, 23 \text{ m}\}$. A logarithmic profile is assumed for the inflow, with $z_0 = 0.1$. The reference velocity was 3 m s^{-1} at a height of 10 m. Solving this UFOP for any objective using an exhaustive search would require 4^8 or 65 536 QUIC-GPU (forward model) simulations. For this problem, the current simulation capability of QUIC-GPU is about 7000 configurations per day, per machine. That is, even for a simple UFOP comprising the simple 2×2 building array, an exhaustive search would take approximately 10 days for a single objective function. Thus, it can be seen that for realistic city designs, where each urban object can have several degrees of freedom in the decision variable space, optimization methods are the only option. For the 8D test problem, 250 500 particles (0.5 g) were released per emitter per simulation. The simulations were run for 150 s, with a Lagrangian time-step of 0.1 s. The concentration field computed by QUIC-GPU had a grid resolution of 1 m. Minimizing the maximum and average concentrations at the street level (1.5 m above ground) in the region ABCD were chosen to be the objective functions.

To assess the performance and the accuracy of the final solutions provided by SA and BGA, forward model (QUIC-GPU) simulations were run for all the 65 536 configurations. SA was run for 6400 iterations (forward model evaluations) ($\approx 1/10$ of the total number of configurations), and the BGA was run for 100 iterations (6400 QUIC-GPU evaluations). SA and BGA were run 10 000 times (using the exhaustive search data) to determine the frequency with which they identify the globally optimum solution. Good implementations of SA and BGA require optimum tuning parameter selection in these algorithms, specific to the problem. Table 5.1 summarizes the cooling schedule used in SA. In Table 5.1, T_0^M , T_f^M , and α^M represent the initial and final temperatures and temperature decrease rate when the objective is to minimize the maximum concentration. The corresponding parameters when the objective is to minimize the average concentration are, T_0^A , T_f^A , and α^A . In Table 5.2, the parameters chosen in the BGA for both the objective functions are listed.

In the version of SA implemented, the following candidate-generating kernel is used for both the objectives. Each component of a newly generated urban configuration (possible transition of the SA Markov chain) depends on the corresponding component of the previous configuration and is generated independently of the other components. The 2×2 building array problem is comprised of 8 decision variables, with the decision variables taking values

in finite sets of cardinality 4. Let the set corresponding to the i^{th} decision variable be S^i , with $S^i = \{s_1^i, s_2^i, s_3^i, s_4^i\}$. Keeping the 2×2 array problem in mind, it is assumed that the set S^i has an order, with $s_1^i < s_2^i < s_3^i < s_4^i$ (since $S^i \subset \mathbb{R}$, S^i inherits the order of \mathbb{R}). For every element s_j^i of S^i , the following sets (neighborhoods) are defined, $N(s_1^i) = \{s_4^i, s_1^i, s_2^i\}$; $N(s_2^i) = \{s_1^i, s_2^i, s_3^i\}$; $N(s_3^i) = \{s_2^i, s_3^i, s_4^i\}$; and $N(s_4^i) = \{s_3^i, s_4^i, s_1^i\}$. If the current state of the chain in the i^{th} component is s_j^i , then the next state s_k^i is generated from $N(s_j^i)$, with each element of $N(s_j^i)$ selected with probability $1/3$. This is done for all the components to generate the next state of the SA Markov chain. It should be noted that the choice of the candidate-generating mechanism affects the performance of the SA implementation.

5.5 Results and Discussion

5.5.1 Minimizing the Maximum Concentration at Street Level

Shown in Fig. 5.2 are the mean streamline patterns and the normalized mean concentration field at street level (1.5 m above ground) for the configuration obtained for the 2×2 building array problem, when the objective was to minimize the maximum street level concentration (obtained from BGA and verified by exhaustive search). The normalized concentration field is computed as, $C^* := Cu_{ref}Hl/Q$, where C^* , C , u_{ref} , H , l , and Q are the normalized concentration, actual concentration, the reference velocity ($= 10 \text{ m s}^{-1}$), building height ($= 10 \text{ m}$), the total emitter length ($= 60 \text{ m}$), and the emission rate ($= 1/150 \text{ g s}^{-1}$). From the figure it can be deduced that the obtained solution is very much in line with intuition. That is because one would expect the maximum concentration at the street level to be minimum when all the four buildings are the farthest from the emitters, as it decreases the retention time of the particles released, thereby helping in effective ventilation of the released contaminants. The results obtained further demonstrate the ability of QUIC-GPU to produce intuitively consistent wind and concentration fields in complex urban domains in a matter of few seconds.

5.5.2 Minimizing the Average Concentration at Street Level

Shown in Fig. 5.3 are the street level mean streamline patterns and the normalized mean concentration field for the configuration obtained, when the objective was to minimize the average street level concentration. As much as at first sight the result appears counter-intuitive, examining the definition of the average concentration sheds light on the validity of the result obtained. The average concentration at the street level is computed as the mean of all the concentration values at the grid nodes at $z = 1.5 \text{ m}$. Intuitively, one would expect the best configuration when minimizing the average concentration to be similar to

that obtained when minimizing the maximum concentration, that is, with all four buildings being farthest from the emitters. However, the result obtained suggests that the best solution when minimizing the average concentration is when buildings 2 and 3 are the farthest from the emitters, while buildings 1 and 4 are closest to the emitter along the y -axis. The difference between the solutions in Fig. 5.3b and Fig. 5.2b is that the regions $(30, 33] \times [15, 25]$ and $(30, 33] \times [35, 45]$ (where $(a, b) \times (c, d)$ represents the Cartesian product across intervals $(a, b), (c, d) \subset \mathbb{R}$, and $(a, b]$ denotes the set $\{x : a < x \leq b, x \in \mathbb{R}\}$) in Fig. 5.2b are occupied by buildings 4 and 1 in Fig. 5.3b. Since the version of QUIC-GPU used does not account for infiltration of contaminants into the buildings, the concentration values at grid nodes that lie within a building are zero. And since the regions $[20, 23) \times [15, 25]$, and $[20, 23) \times [35, 45]$ in Fig. 5.3b are upwind of buildings 4 and 1 (and also upwind of the emitter parallel to the y -axis, and along wind and at considerable lateral distance from the emitter parallel to the x -axis), these regions are not significantly infiltrated by the particles released. Consequently, when computing the average concentration of the configuration in Fig. 5.3b, there are a greater number of grid nodes with smaller concentration values in comparison to the configuration in Fig. 5.2b. Therefore, the configuration in Fig. 5.3b is better than the configuration in Fig. 5.2b, when the objective is to minimize the average concentration, and this result is an artifact of the averaging procedure.

5.5.3 Performance of the Optimization Techniques

5.5.3.1 Performance of BGA

To evaluate the performance of BGA, it was run 10 000 times using the exhaustive search data (for each objective function). The BGA converged to the globally optimum solution in all the 10 000 test runs (100% success rate), for both the objective functions.

5.5.3.2 Performance of SA

Shown in Figs. 5.4a and 5.4b are the frequencies with which the current implementations of SA converge to the top 75 solutions (urban configurations), when the objectives are to minimize the maximum and average concentrations at street level. SA always converged to one of these 75 solutions in the 10 000 simulations. From the figure it is seen that the success rates of SA in identifying the globally optimum solutions are 51.98% and 52.21%, for the maximum and average concentrations objectives. Comparing the performance of BGA against SA, it is evident that the BGA outperforms SA in terms of identifying the optimum urban configuration. Several reasons can be given to explain this observation, the most important being ergodicity breaking of the SA Markov chain at lower temperatures.

That is, at lower temperatures, once the chain gets stuck in a good local optimum, it is very hard for the chain to accept transitions to eventually reach the global optimum. Also, the population-based learning strategy, along with the *crossover* and *mutation* operators, help GA better explore the state space, and the *elitism* operator ensures that the best solution throughout the iteration procedure is taken as the final solution. Finally, the performance of SA depends upon the choice of several parameters such as the candidate-generating mechanism, the cooling schedule, the length of the Markov chain, etc. And given that the necessary and sufficient conditions that ensure convergence to global optima are no longer satisfied in practical implementation, one has to contend with the *good* solutions provided by SA.

5.5.4 Top Six Solutions

Figs. 5.5 and 5.6 show the top six configurations when the objective is to minimize the maximum and average street level concentrations. The configurations were sorted from the exhaustive search data. From the figures it is evident that the solutions in the vicinity of the global best solution differ only very slightly from the best solution in terms of urban geometry and are in line with intuition. These figures again demonstrate the ability of QUIC-GPU in producing intuitively consistent wind and concentration fields in urban domains.

5.6 Summary

In the work presented, the problem of identifying urban forms that result in low pollution levels in urban domains is considered. Solution of urban form optimization problems (UFOP) pose several challenges including computationally intensive forward simulation models and possible high-dimensional state spaces. To address the forward model complexity challenge, the quick urban and industrial complex dispersion model (QUIC) adapted to graphics processing units (GPU) (QUIC-GPU) is used as the forward model. Through the current and previous works, the ability of QUIC-GPU to compute reasonably accurate flow and dispersion fields in urban domains extremely rapidly is demonstrated. To tackle the possible high-dimensional state space challenge, UFOP are cast as optimization problems. Stochastic derivative-free methods such as simulated annealing (SA) and genetic algorithms (GA) are considered as the optimization techniques. To demonstrate the application of QUIC-GPU in conjunction with SA / GA in the solution of UFOPs, a simple (eight dimensional) 2×2 building array problem, with 65 536 possible configurations is considered. An exhaustive search was performed for the test problem, and the results, and performance

of SA and GA were compared against exhaustive search data. SA and GA were run 10 000 times to compute the frequency with which they identify the global best configuration, which was ascertained from exhaustive search data. The number of forward model evaluations in SA and GA were fixed to 6400 ($\approx 1/10$ of total number of configurations). The GA performed better than SA and converged to the global best configuration in all the 10 000 simulations (100% success rate).

5.7 References

- [1] A. J. Robson, "The effect of urban structure on concentration of pollution," *Urban Studies*, vol. 14, pp. 89–93, 1977.
- [2] I. C. Medina, G. Schattaneck, and F. Nichols Jr., "A framework for integrating information systems in air quality analysis," in *Urban and Regional Information Association (URISA), 32nd Annu. Conf.*, Milwaukee, WI, 1994, pp. 339–348.
- [3] L. O. Marquez and N. C. Smith, "A framework for linking urban form and air quality," *Environmental Modelling and Software*, vol. 14, no. 6, pp. 541–548, 1999.
- [4] C. Borrego, H. Martins, O. Tchepel, L. Salmim, A. Monteiro, and A. I. Miranda, "How urban structure can affect city sustainability from an air quality perspective," *Environmental Modelling and Software*, vol. 21, no. 4, pp. 461–467, 2006.
- [5] K. J. Craig, D. J. de Kock, and J. A. Snyman, "Minimizing the effect of automotive pollution in urban geometry using mathematical optimization," *Atmospheric Environment*, vol. 35, no. 3, pp. 579–587, 2001.
- [6] B. Singh, B. Hansen, M. Brown, and E. Pardyjak, "Evaluation of the quic-urb fast response urban wind model for a cubical building array and wide building street canyon," *Environmental Fluid Mechanics*, vol. 8, no. 4, pp. 281–312, 2008.
- [7] B. Singh, E. R. Pardyjak, A. Norgren, and P. Willemsen, "Accelerating urban fast response lagrangian dispersion simulations using inexpensive graphics processor parallelism," *Environmental Modelling and Software*, vol. 26, no. 6, pp. 739–750, 2011.
- [8] A. Gowardhan, M. Brown, and E. Pardyjak, "Evaluation of a fast response pressure solver for flow around an isolated cube," *Environmental Fluid Mechanics*, vol. 10, no. 3, pp. 311–328, 2007.
- [9] J. E. Flaherty, K. J. Allwine, M. J. Brown, W. I. J. Coirier, S. C. Ericson, O. R. Hansen, A. H. Huber, S. Kim, M. J. Leach, J. D. Mirocha, R. K. Newsom, G. Patnaik, and I. Senocak, "Evaluation study of building-resolved urban dispersion models," no. 10.2. San Diego, CA: American Meteorological Society, September 2007, pp. 1–5.
- [10] S. Kirkpatrick, C. D. Gelatt, and M. P. Vecchi, "Optimization by simulated annealing," *Science*, vol. 220, pp. 671–680, 1983.
- [11] N. Metropolis, A. Rosenbluth, M. Rosenbluth, A. Teller, and E. Teller, "Equation of state calculations by fast computing machines," *The Journal of Chemical Physics*, vol. 21, no. 6, pp. 1087–1092, 1953.

- [12] W. K. Hastings, “Monte Carlo sampling methods using Markov chains and their applications,” *Biometrika*, vol. 57, no. 1, pp. 97–109, 1970.
- [13] P. J. M. van Laarhoven and E. H. L. Aarts, *Simulated Annealing-Theory and Applications*, 1st ed. New York: Kluwer Academic Publishers, 1987.
- [14] J. Schneider and S. Kirkpatrick, *Stochastic Optimization*, 1st ed. New York: Springer, 2006.
- [15] B. Hajek, “Cooling schedules for optimal annealing,” *Mathematics of Operations Research*, vol. 13, no. 2, pp. 311–329, 1988.
- [16] C. P. Robert and G. Casella, *Monte Carlo statistical methods*, 2nd ed., ser. Springer texts in statistics. New York: Springer, 2004.
- [17] D. E. Goldberg, *Genetic Algorithms in Search, Optimization, and Machine Learning*, 1st ed. New York: Addison-Wesley Professional, 1989.
- [18] R. L. Haupt and S. E. Haupt, *Practical Genetic Algorithms*. New York: Wiley-Interscience, 2004.

Table 5.1. Parameters in SA implemented for the 2×2 array problem.

Initial temperature (T_0)	$T_0^M \approx 7.77 \times 10^{-6}, T_0^A \approx 1.93 \times 10^{-5}$
Final temperature (T_f)	$T_f^M \approx 1.44 \times 10^{-9}, T_f^A \approx 2.31 \times 10^{-8}$
Temperature decrease rate (α)	$\alpha^M \approx 0.9987, \alpha^A \approx 0.9989$

Table 5.2. Parameters in the BGA implemented for the 2×2 array problem.

Population size	64
Number of chromosomes	8
Number of bits to represent chromosomes	16
Selection rate	0.5
Weighting procedure	rank weighting
Mutation rate	0.10
Number of iterations	100

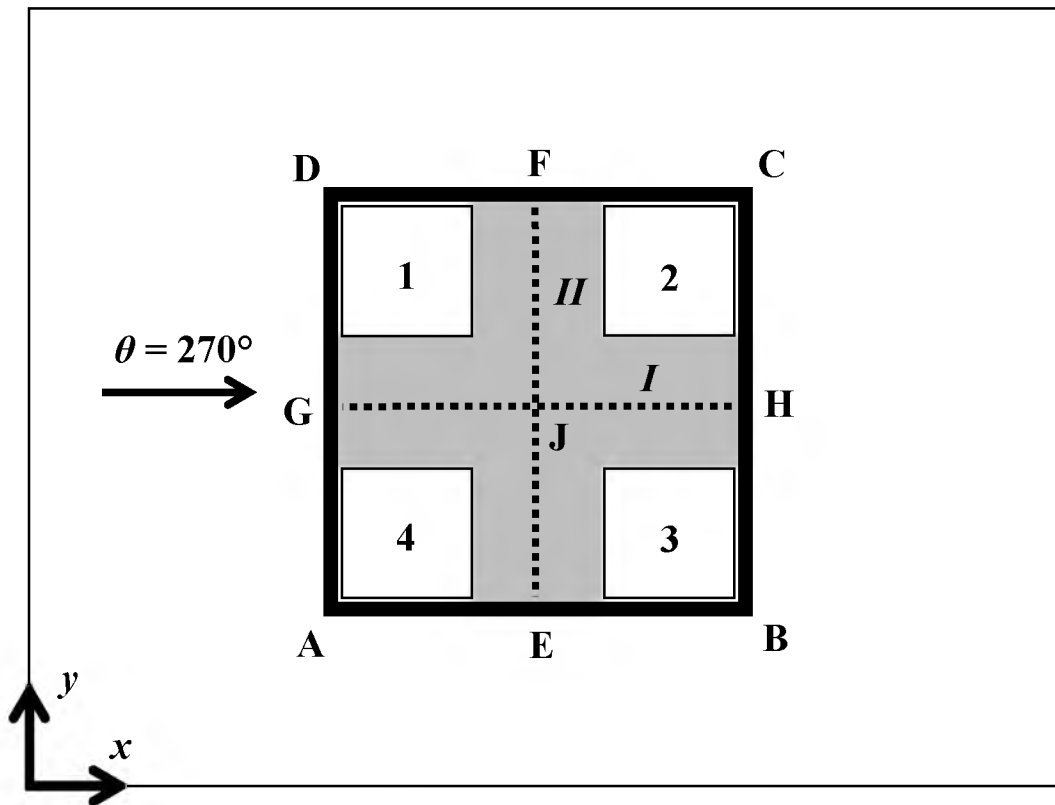


Figure 5.1. The 2×2 building array (8D) problem (figure not to scale).

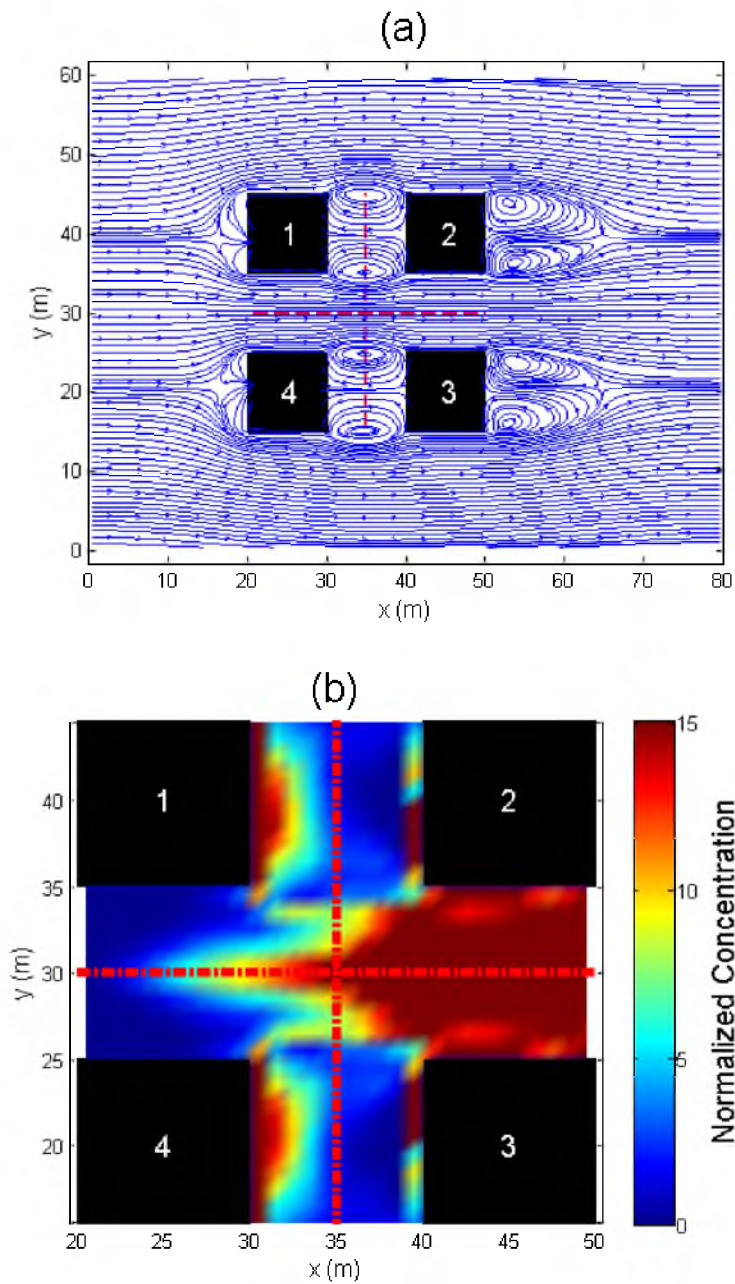


Figure 5.2. Shown in (a) and (b) are the mean streamline patterns and concentration field at street level ($z = 1.5\text{m}$) for the global best configuration obtained when the objective was to minimize the maximum street level concentration.

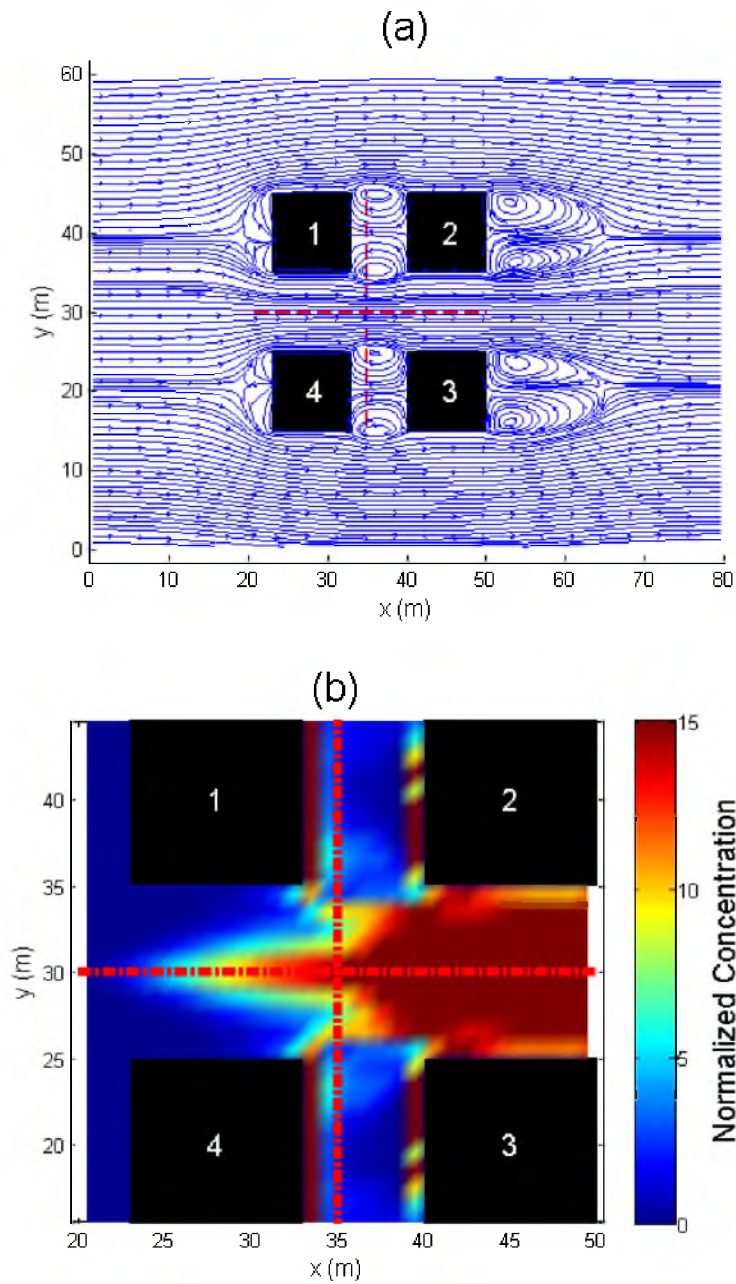


Figure 5.3. Shown in (a) and (b) are the mean streamline patterns and concentration field at street level ($z = 1.5\text{m}$) for the global best configuration obtained when the objective was to minimize the average street level concentration.

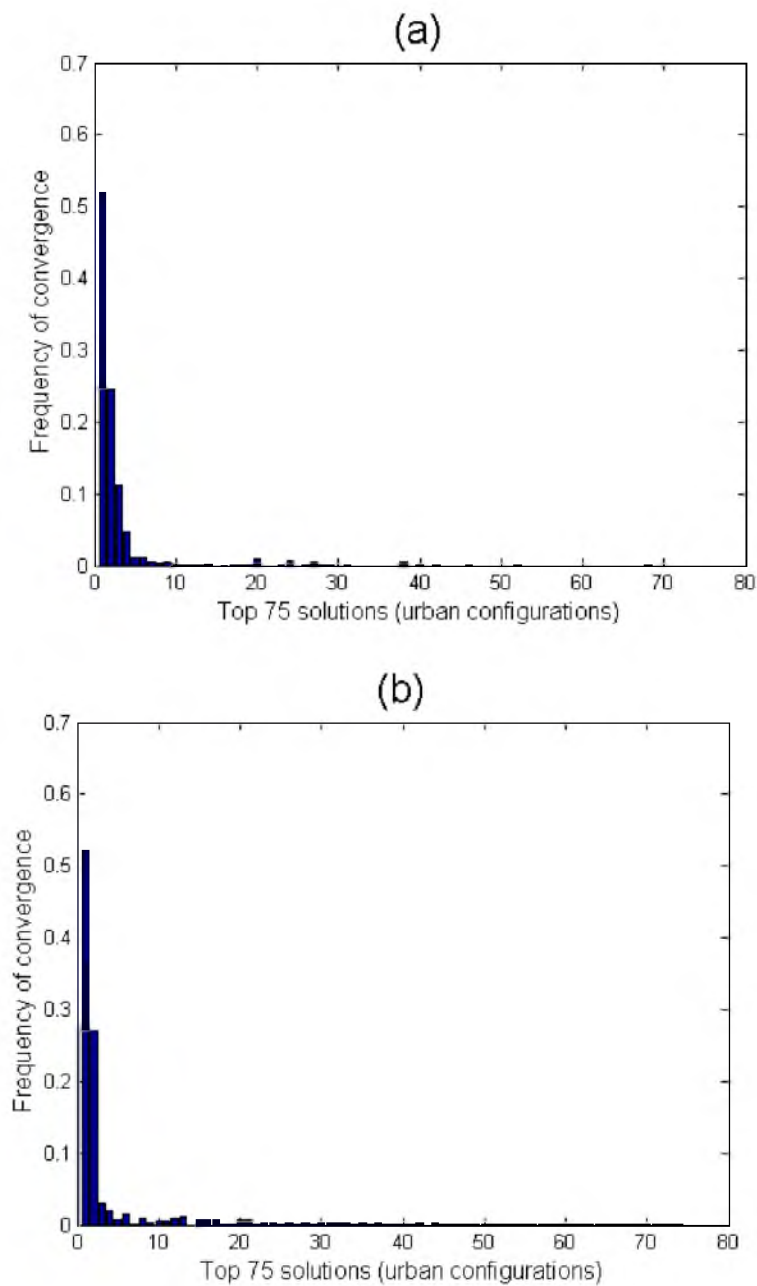


Figure 5.4. Frequency of convergence of SA to the top 75 urban configurations, when the objective is to minimize street level, (a) maximum, and (b) average concentrations.

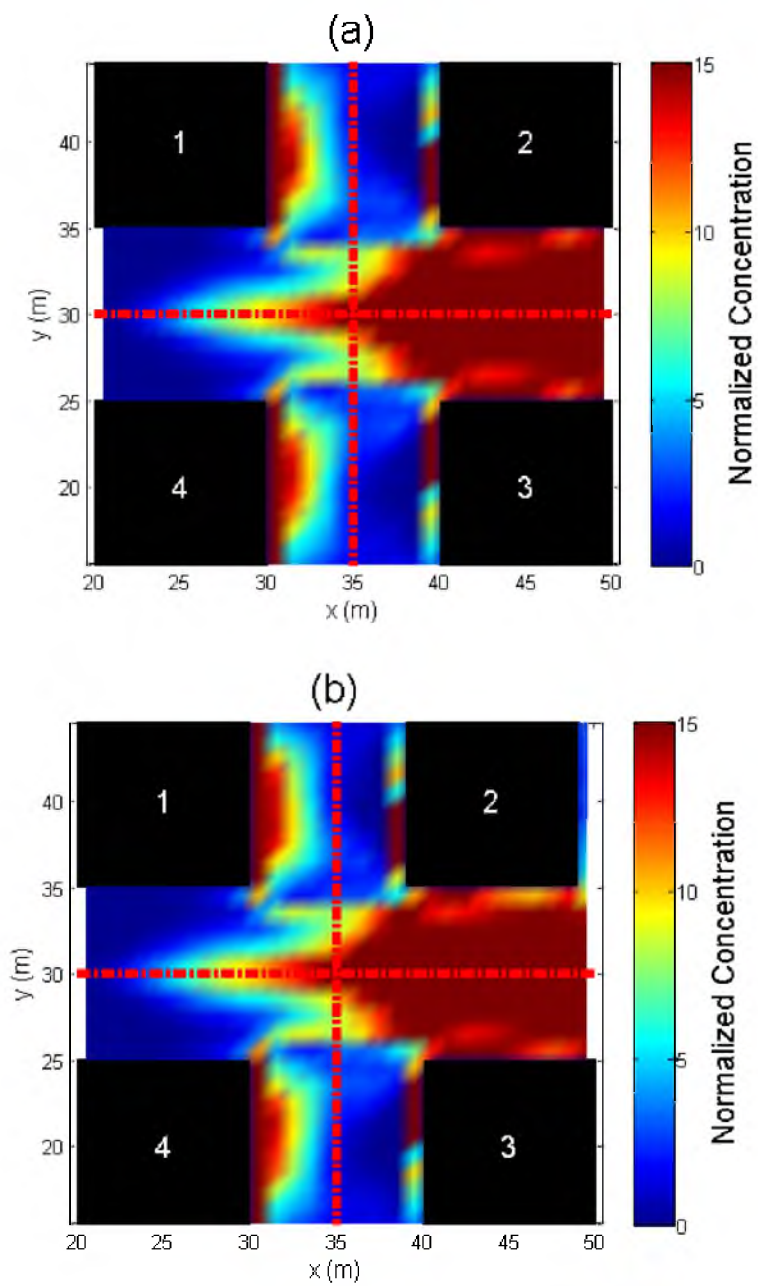


Figure 5.5. Top six urban configurations when the objective is to minimize maximum street level concentrations. (a) represents the best solution, (b) the second best solution, and so on.

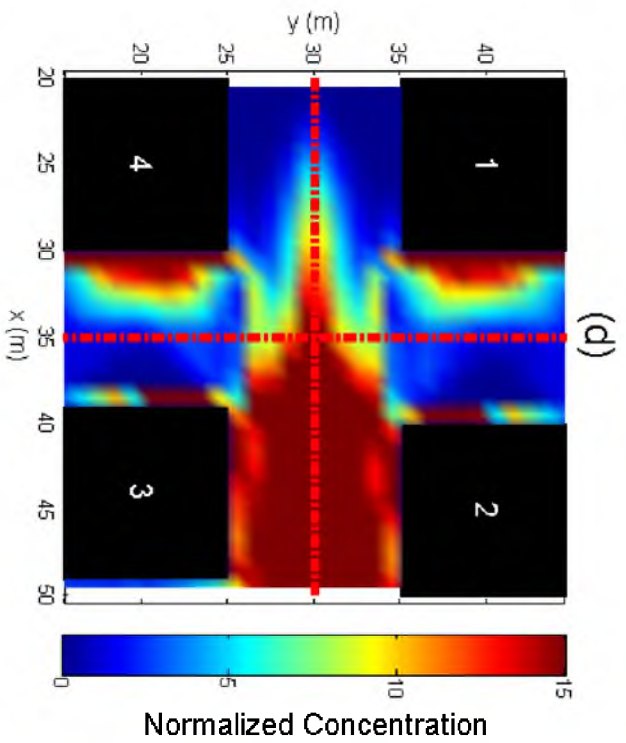
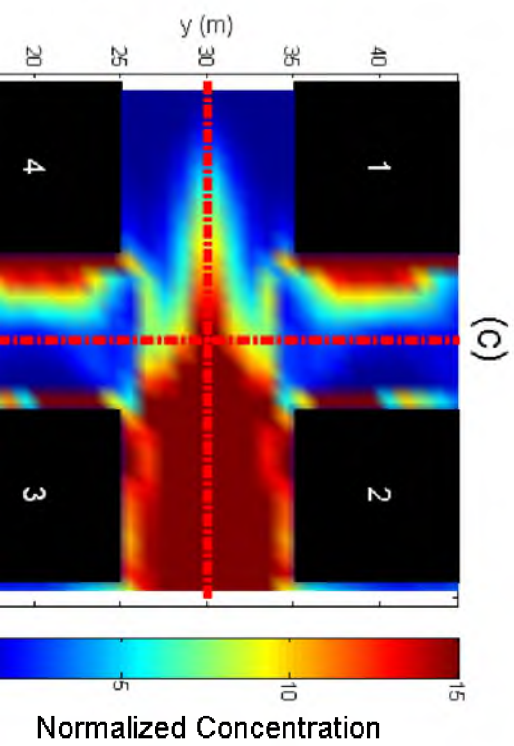


Figure 5.5. continued.



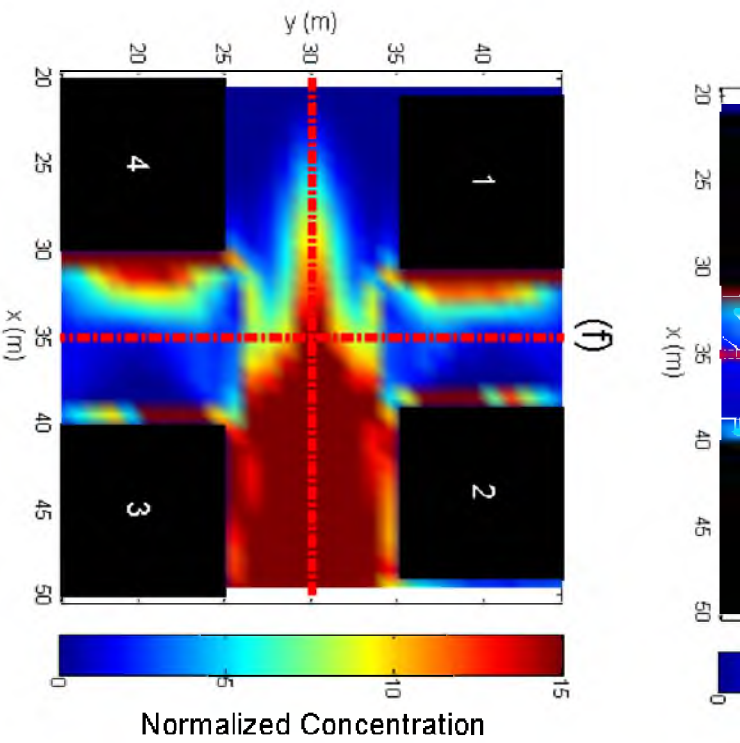
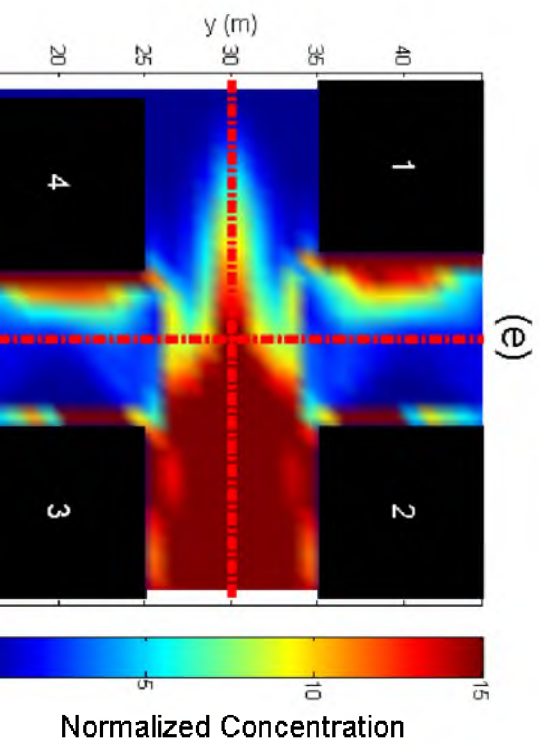


Figure 5.5. continued.



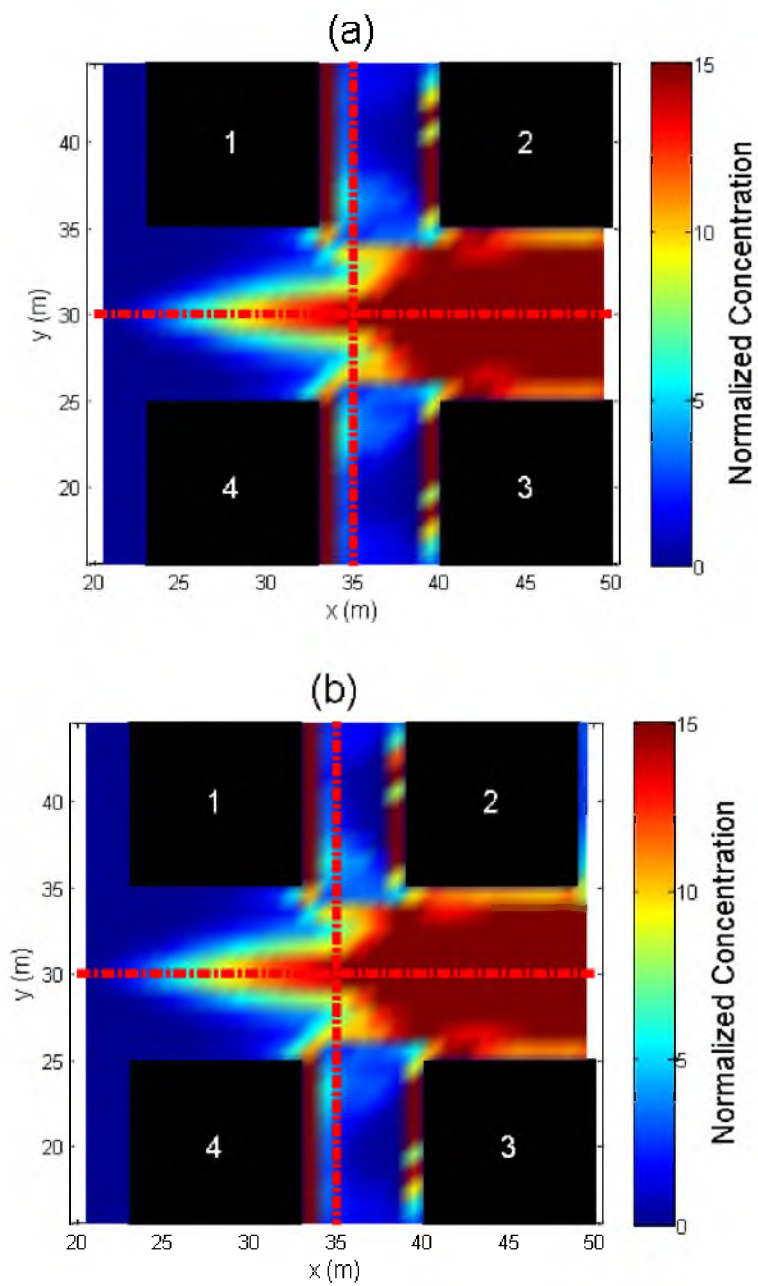


Figure 5.6. Top six urban configurations when the objective is to minimize average street level concentrations. (a) represents the best solution, (b) the second best solution, and so on.

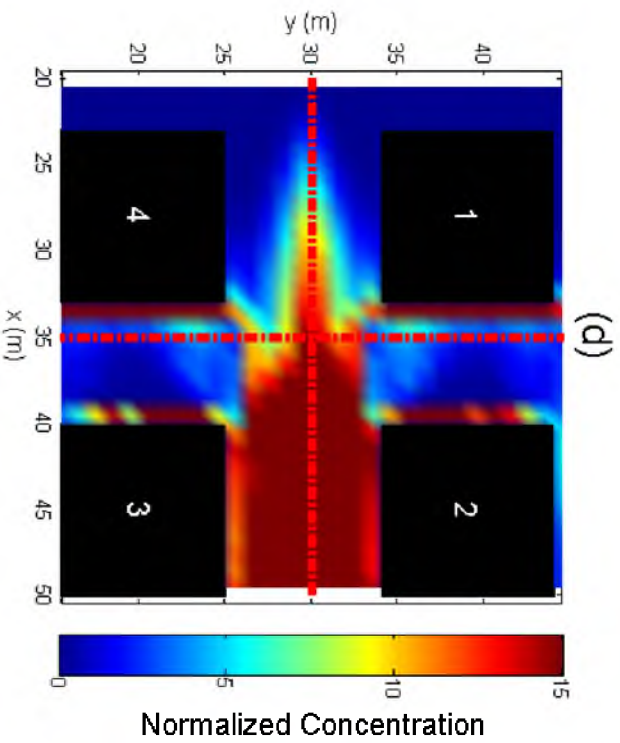
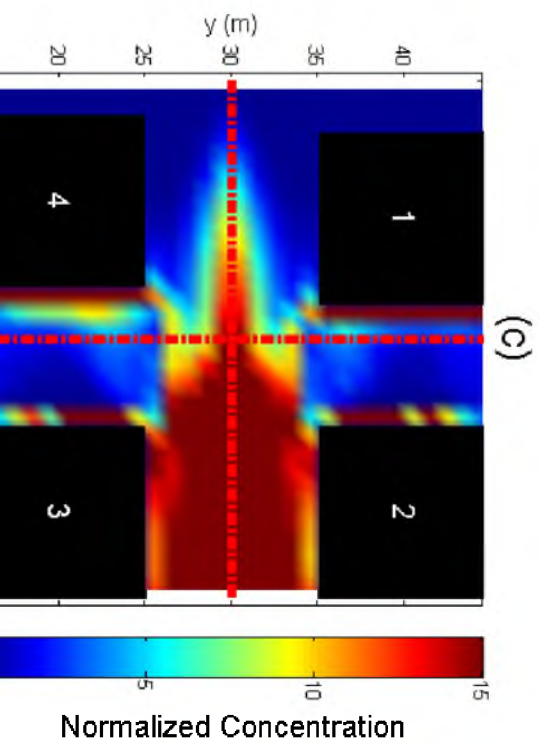


Figure 5.6. continued.



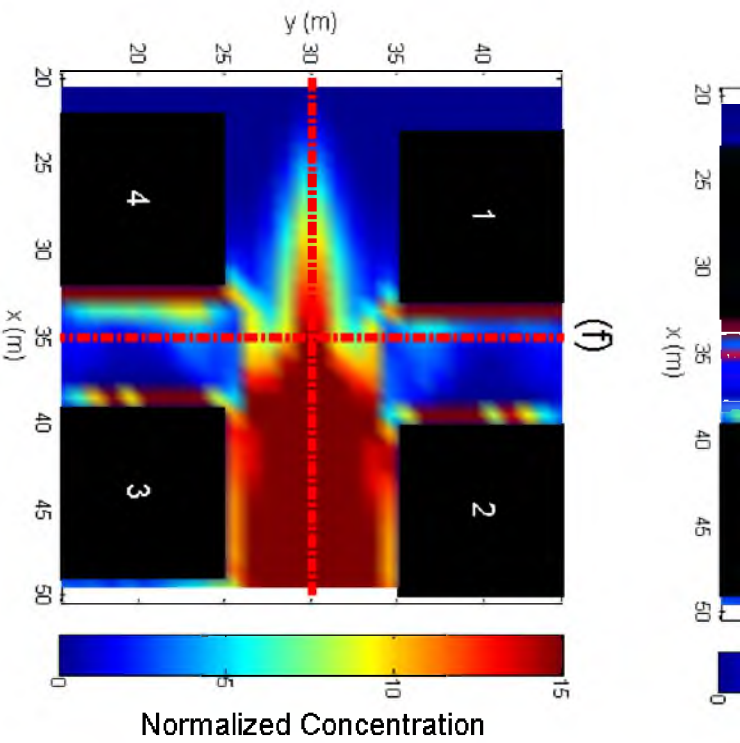
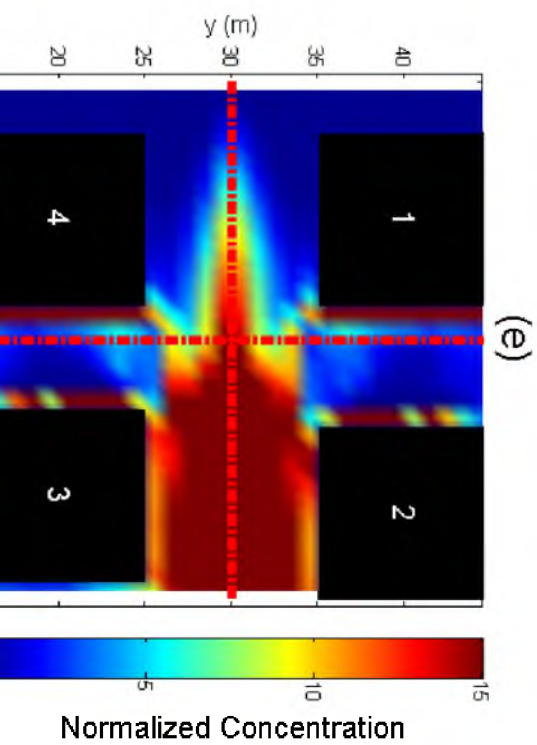


Figure 5.6. continued.



CHAPTER 6

CONCLUSIONS

As much as each chapter in this dissertation is its own body of work with its own conclusions, this chapter summarizes the results and provides overall conclusions for the research performed.

The experiments conducted to better understand flows in the vicinity of tall buildings (tall building street canyons) demonstrate that the flow patterns in tall building street canyons are fundamentally different from those observed in square canyons and two-dimensional (2D) canyons. Among other features, tall building street canyon flows are characterized by strong updrafts and downdrafts. The experimental results also illustrate the importance of and the need for accounting for the sidewall motions (momentum) into the canyon, which is neglected in 2D simulations. The flow patterns observed were very unique and counterintuitive and were not reported previously in the street canyon literature. Additionally, the experimental data has been used to evaluate and improve the empirical parameterizations in the quick urban and industrial complex (QUIC) dispersion modeling system.

Chapter 4 concentrates on the development of efficient and robust atmospheric event reconstruction tools. An atmospheric event reconstruction tool is comprised of three principal components: (1) a forward prediction model, (2) the objective function formulation, and (3) the optimization method. Different forward models, objective functions, and optimization techniques can be used in the solution of source characterization problems. The choices for these components determine the overall accuracy and speed of reconstruction. In general, there exist a suite of methods to solve inverse problems. However, there is no single-best technique to solve every inverse problem. Each technique is tailored to a particular type of inverse problem. In Chapter 4, the effect of the objective function formulation on the accuracy and complexity of inversion is examined. Based on this study, a new objective function that can better handle the zero and nonzero measurements recorded by atmospheric sensors and that accounts for the exponential decay nature of scalar mixing is developed. It is shown that choosing the optimization technique based on the forward model employed can

help improve the efficiency of event reconstruction tools. To further this assertion, a source inversion problem is considered, and the Gaussian plume model is used as the forward model. Since analytical expressions for the Frechet and Hessian for the Gaussian model can be precomputed, gradient-based optimization is used. The results obtained indicate significant improvements in the speed of inversion, in comparison to other techniques employed in the literature for the same problem.

In Chapter 5, the problem of identifying urban forms that result in the best environmental conditions in an urban domain is considered. The utility of the urban form optimization tool developed through the current work cannot be overemphasized. Engineers, urban planners, and decision-makers will be the end-users of this tool. The knowledge gained using the tool will help address sustainability issues with new urban designs, which could potentially impact the quality of life of millions of people living in urban areas.